

MAGNETIC RESONANCE CONDUCTIVITY TENSOR IMAGING (MRCTI) AT
3 TESLA

A THESIS SUBMITTED TO
THE GRADUATE SCHOOL OF NATURAL AND APPLIED SCIENCES
OF
MIDDLE EAST TECHNICAL UNIVERSITY

BY

MEHDI SADIGHI

IN PARTIAL FULFILLMENT OF THE REQUIREMENTS
FOR
THE DEGREE OF MASTER OF SCIENCE
IN
ELECTRICAL AND ELECTRONICS ENGINEERING

FEBRUARY 2014

Approval of the thesis:

**MAGNETIC RESONANCE CONDUCTIVITY TENSOR IMAGING
(MRCTI) AT 3 TESLA**

submitted by **MEHDI SADIGHI** in partial fulfillment of the requirements for the degree of **Master of Science in Electrical and Electronics Engineering Department, Middle East Technical University** by,

Prof. Dr. Canan Özgen _____
Dean, Graduate School of **Natural and Applied Sciences**

Prof. Dr. Gönül Turhan Sayan _____
Head of Department, **Electrical and Electronics Engineering**

Prof. Dr. Murat Eyüboğlu _____
Supervisor, **Electrical and Electronics Engineering Dept., METU**

Examining Committee Members:

Prof. Dr. Nevzat G. Gençer _____
Electrical and Electronics Engineering Dept., METU

Prof. Dr. Murat Eyüboğlu _____
Electrical and Electronics Engineering Dept., METU

Prof. Dr. Tolga Çiloğlu _____
Electrical and Electronics Engineering Dept., METU

Assoc. Prof. Dr. Yeşim Serinağaoğlu Doğrusöz _____
Electrical and Electronics Engineering Dept., METU

Assist. Prof. Dr. Evren Değirmenci _____
Electrical and Electronics Engineering Dept., Mersin University

Date: 07.02.2014

I hereby declare that all information in this document has been obtained and presented in accordance with academic rules and ethical conduct. I also declare that, as required by these rules and conduct, I have fully cited and referenced all material and results that are not original to this work.

Name, Last name: MEHDI SADIGHI

Signature :

ABSTRACT

MAGNETIC RESONANCE CONDUCTIVITY TENSOR IMAGING (MRCTI) AT 3 TESLA

Sadighi, Mehdi

MSc. Departement of Electrical and Electronics Engineering

Supervisor : Prof. Dr. Murat Eyüboğlu

February 2014, 101 pages

Electrical conductivity of biological tissues changes with physiological and pathological state of tissue. Therefore, recognizing the changes of the conductivity distribution inside human body, provides unique information about the pathological conditions of internal organs which is not available from other imaging modalities. Magnetic Resonance Electrical Impedance Tomography (MREIT) is an imaging technique to reconstruct the isotropic conductivity distribution of the biological tissues. But most of the biological structures and tissues have anisotropic conductivity. Therefore, Magnetic Resonance Conductivity Tensor Imaging (MRCTI) is proposed to image the anisotropic conductivity distribution. Similar to MREIT technique, MRCTI reconstruction algorithms are grouped into B -based and J -based algorithms. The aim of this study is implementing the MRCTI

J-based algorithms to reconstruct the experimental data obtained using a 3 Tesla Magnetic Resonance Imaging (MRI) system. An experimental phantom is designed and manufactured with special properties according to needs of the experiments and the resulted conductivity distributions are compared. Furthermore, a novel hybrid *J*-based reconstruction algorithm namely, the Anisotropic Hybrid Equipotential Projection (AHEPP) is proposed, and the related simulations and experimental results are given. In addition, performance of the four *J*-based MRCTI algorithms in reconstruction of the experimental data is evaluated using error measures.

Keywords: Magnetic resonance, electrical impedance, tomography, anisotropic conductivity, reconstruction, imaging.

ÖZ

3 TESLADA MANYETİK REZONANS İLETKENLİK TENSÖRÜ GÖRÜNTÜLEME (MRİTG)

Sadighi, Mehdi

Master, Elektrik ve Elektronik Mühendisliği Bölümü

Danışmanı : Prof. Dr. Murat Eyüboğlu

Şubat 2014, 101 sayfa

Biyolojik dokuların elektriksel iletkenlikleri fizyolojik ve patolojik durumlarına göre değişiklik göstermektedir. Bu nedenle, insan vücudundaki iletkenlik dağılımının değişimlerini teşhis etmek için organların patolojik durumları hakkında diğer görüntüleme metotlarının yetersiz kaldığı yerde özgün bilgiler sağlar. Eşyönlü iletkenlik dağılımını görüntülemek için kullanılan tekniklerden biri Manyetik Rezonans Elektriksel Empedans Tomografisidir (MREET). Ancak insan vücudundaki çoğu doku ve yapıda iletkenlik dağılımı eşyönsüzdür. Bu nedenle, eşyönsüz iletkenlik dağılımını görüntülemek için Manyetik Rezonans İletkenlik Tensörü Görüntülemesi (MRİTG) önerilmiştir. MREET tekniğindeki benzer şekilde, MRİTG geriçatım algoritmaları B -tabanlı ve J -tabanlı olarak gruplandırılmaktadır. Bu çalışmanın amacı, 3 Tesla Manyetik Rezonans Görüntüleme sisteminde elde edilen deneysel verilerin J -tabanlı algoritmalar kullanılarak

iletkenlik görüntülerinin oluşturulmasıdır. Deneysel çalışmaya uygun özellikte fantom tasarımı ve üretimi yapıp elde edilen iletkenlik dağılımları karşılaştırılmıştır. Ayrıca, Eşyönsüz Hibrit Eşpotansiyel İzdüşümü (EHEİ) diye adlandırılan J -tabanlı özgün hibrit bir algoritma önerilmiş ve buna dair simülasyon ve deneysel sonuçlar verilmiştir. Bunlara ek olarak, deneysel veriler kullanılarak dört farklı J -tabanlı MRİTG geriçatım algoritmasının performansı hata hesapları gözetilip değerlendirilmiştir.

Anahtar Kelimeler: Manyetik Rezonans, elektriksel empedans, tomografi, eşyönsüz iletkenlik, geriçatım, görüntüleme.

To My Parents

ACKNOWLEDGEMENTS

I would like to express my utmost and deepest gratitude and appreciation to my dear supervisor, Prof. Dr. Murat Eyübođlu for his continuous effort, patience and guidance in providing invaluable ideas, encouragement and exceptional role he has played in making this thesis a reality.

I would also like to thank Assist Prof. Dr. Evren Deđirmenci for his valuable guidance during the thesis study.

My utmost gratitude is forwarded to my beloved parents, Abbas and Fatemeh and my sister Elham, for their love, support and encouragement during this period.

I would like to thank Cihan Göksu, who as a good friend and colleague, was always willing to help and give his best suggestions. It would have been a lonely lab without him.

I would like to thank my dear friend Fourough Gharbalchi, she was always there cheering me up and stood by me through the good times and bad.

I would like to thank Sasan Sokhanvar for his kindness, friendship and support during the thesis period.

Last but not least, my warmest appreciation to all my friends especially Mürsel Karadaş, Kemal Sümser, Mehdi Ebrahimi, Mohammad Reza Robaie, Gizem Bedir and Ceren Bora.

TABLE OF CONTENTS

ABSTRACT.....	v
ÖZ.....	vii
ACKNOWLEDGEMENTS.....	x
TABLE OF CONTENTS.....	xi
LIST OF TABLES.....	xiv
TABLE OF FIGURES.....	xv
LIST OF ABBREVIATIONS.....	xix
CHAPTERS	
1. INTRODUCTION.....	1
1.1. Electrical Properties of Tissues.....	1
1.1.2. Anisotropy of Tissues.....	2
1.2. Electrical Impedance Tomography.....	2
1.3. Magnetic Resonance Electrical Impedance Tomography.....	3
1.4. Objectives of the Thesis.....	11
1.5. Outline of the Thesis.....	12
2. METHODOLOGY OF CURRENT DENSITY AND ANISOTROPIC CONDUCTIVITY IMAGING USING MAGNETIC RESONANCE IMAGING SYSTEM.....	13
2.1. Introduction.....	13
2.2. Magnetic Resonance Current Density Imaging (MRCDI)	14
2.2.1. Phase Unwrapping.....	19
2.3. The Forward Problem of the Anisotropic MREIT.....	21

2.4. Inverse problem of MRCTI.....	23
2.4.1. Equipotential Projection Algorithm For Anisotropic Conductivity Reconstruction.....	23
2.4.1.1. Introduction.....	23
2.4.1.2. Anisotropic Equipotential Projection (AEPP) Algorithm.....	24
2.4.2. Anisotropic J-Substitution (AJS) Algorithm.....	30
2.4.2.1. Introduction.....	30
2.4.2.2. Anisotropic <i>J</i> -substitution algorithm.....	31
2.4.3. Anisotropic Hybrid J-Substitution (AHJS) Algorithm.....	36
2.4.4. Anisotropic Hybrid Equipotential Projection (AHEPP) Algorithm.....	37
3. EXPERIMENTAL SETUP FOR MRCTI AT 3 TESLA MRI SYSTEM.....	39
3.1. Introduction.....	39
3.2. Pulse Sequence Generation.....	40
3.3. Current Source.....	41
3.3.1. Boost Converter.....	44
3.3.2. Voltage to Current Converter.....	46
3.4. Experimental Phantom.....	47
3.5. Conductivity Cell.....	56
4. RESULTS AND COMPARISONS.....	57
4.1. Introduction.....	57
4.2. SNR Calculation.....	58
4.3. Error Calculation.....	60
4.4. Scaling Factor Calculation.....	61
4.4.1 Scaling the relative reconstructed conductivity distribution by calculating the potential values in the boundary pixels for an unknown conductivity distribution in the imaging region.....	62
4.5. Pulse Sequence Parameters.....	66

4.6. Simulation Results of the Proposed AHEPP Algorithm.....	67
4.7. Results of the Experimental Phantom.....	70
4.7.1. Experimental Results of the Magnetic Flux Density and Current Density Distributions.....	70
4.7.2. Experimental Results of the Reconstructed Anisotropic Conductivities....	83
4.7.2.1. The Reconstructed Conductivities Using AEPP algorithm.....	83
4.7.2.2. The Reconstructed Conductivities Using AJS algorithm.....	84
4.7.2.3. The Reconstructed Conductivities Using AHJS algorithm.....	86
4.7.2.4. The Reconstructed Conductivities Using AHEPP algorithm.....	87
4.7.3 Comparisons of the Four J -Based MRCTI Algorithms.....	88
 5. CONCLUSIONS.....	 95
REFERENCES.....	97

LIST OF TABLES

TABLES

Table 4.1: The experimental parameter values used in SNR calculation.....	59
Table 4.2: The experimental parameters of the used pulse sequence and the injected current.....	66
Table 4.3: Comparing the error values obtained from the four MRCTI algorithms using the same numerical model in [42] and for the noise free case. (The error values of the first three algorithms are taken from [42])	69
Table 4.4: Percentage error of the reconstructed conductivities in Figure 4.19.....	85
Table 4.5: Percentage error of the reconstructed conductivities in Figure 4.21.....	88

TABLE OF FIGURES

FIGURES

Figure 2.1: Spin Echo pulse sequence with current pulse line (MRCDI pulse sequence).....	19
Figure 2.2: Demonstration of unwrapping: (a) Phase diagram before unwrapping (b) after unwrapping.....	20
Figure 2.3: Phase wrap in an MR phase image: (a) wrapped phase image (b) unwrapped phase image.....	21
Figure 3.1: The 3 Tesla MRI scanner used in this thesis located at National Magnetic Resonance Research Center (UMRAM) at Bilkent University.....	40
Figure 3.2: Schematic diagram of the used current source [44].....	42
Figure 3.3: Spin-echo pulse sequence for MREIT experimental data acquisition.....	43
Figure 3.4: Fiber optic receiver circuit (Avago HFBR-2528Z)	44
Figure 3.5: Diagram schematic of the step-up DC-DC boost converter [44]	45
Figure 3.6: Diagram schematic of the Voltage to Current Converter [44]	46
Figure 3.7: 2D representation of the experimental phantom filled with conductive solution	49
Figure 3.8: Illustration of the current steering structure in the four electrode experimental phantom	50
Figure 3.9: Illustration of current flow inside the phantom slice in presence of the current steering structure which is used to create macro-scale anisotropy in the background material conductivity. (a) Vertical view (b) Horizontal view (c) Vertical current injection profile (d) Horizontal current injection profile.....	51
Figure 3.10: The experimental four electrode phantom.....	52
Figure 3.11: The six current injection profiles using the phantom in Figure 3.10	

(a) Vertical (b) Horizontal (c) First adjacent (up and right) (d) Second adjacent (left and down) (e) Third adjacent (up and right) (f) Fourth adjacent (left and down), current injecting profiles.....	53
Figure 3.12: Illustration of the experimental phantom inside the MR magnet.....	55
Figure 3.13: conductivity cell.....	56
Figure 4.1: Illustration of the boundary pixels along with the assigned voltage values to the source and sink electrodes in the vertical path.....	63
Figure 4.2: The potential value distribution on the boundary pixels of the used experimental phantom and measured voltage in vertical current injection profile.....	65
Figure 4.3: Timing diagram of the spin echo pulse sequence with current injection.....	67
Figure 4.4: Reconstruction results of the simulation model using AHEPP algorithm (SNR = ∞). (a) σ_{xx} (b) σ_{yy}	68
Figure 4.5: The magnetic flux density distribution in all three orientaions for the vertical current injection path using the experimental phantom. (a) z component (experimental) (b) z component (numerical) (c) x -plus (d) x -minus (e) y -plus (f) y -minus	71
Figure 4.6: Current density distribution for the vertical current injection path of the experimental phantom. (a) J_x (b) J_y (c) Total current density distribution	72
Figure 4.7: The magnetic flux density distribution in all three direction for the horizontal current injection path using the experimental phantom. (a) z component	73
Figure 4.8: Current density distribution for the horizontal current injection path of the experimental phantom. (a) J_x (b) J_y (c) Total current density distribution.....	74
Figure 4.9: The magnetic flux density distribution in all three direction for the first adjacent current injection path (up and right electrodes) using the experimental phantom. (a) z component(experimental) (b) z component (numerical) (c) x -plus (d) x -minus (e) y -plus (f) y minus.....	75
Figure 4.10: Current density distribution for first adjacent current injection path (up and right electrodes) of the experimental phantom. (a) J_x (b) J_y (c) Total current density distribution.....	76

Figure 4.11: The magnetic flux density distribution in all three direction for the second adjacent current injection path (left and down electrodes) using the experimental phantom. (a) z component(experimental) (b) z component (numerical) (c) x-plus (d) x-minus (e) y-plus (f) y minus	77
Figure 4.12: Current density distribution for the second adjacent current injection path (left and down electrodes) of the experimental phantom. (a) J_x (b) J_y (c) Total current density distribution	78
Figure 4.13: The magnetic flux density distribution in all three direction for the third adjacent current injection path (up and left electrodes) using the experimental phantom. (a) z component(experimental) (b) z component (numerical) (c) x-plus (d) x-minus (e) y-plus (f) y minus.....	79
Figure 4.14: Current density distribution for the third adjacent current injection path (up and left electrodes) of the experimental phantom. (a) J_x (b) J_y (c) Total current density distribution.....	80
Figure 4.15: The magnetic flux density distribution in all three direction for the fourth adjacent current injection path (right and down electrodes) using the experimental phantom. (a) z component(experimental) (b) z component (numerical) (c) x-plus (d) x-minus (e) y-plus (f) y minus	81
Figure 4.16: Current density distribution for the fourth adjacent current injection path (left and down electrodes) of the experimental phantom. (a) J_x (b) J_y (c) Total current density distribution	82
Figure 4.17: True conductivity distributions obtained using (4.5). (a) σ_{xx} (b) σ_{yy}	83
Figure 4.18: The results of anisotropic conductivity reconstructed using AEPP algorithm for the experimental phantom (a) True conductivity σ_{xx} (b) True conductivity σ_{yy} (c) Reconstructed σ_{xx} (d) Reconstructed σ_{yy}	84
Figure 4.19: The results of anisotropic conductivity reconstructed using AJS algorithm for the experimental phantom (a) True conductivity σ_{xx} (b) True conductivity σ_{yy} (c) Reconstructed σ_{xx} (d) Reconstructed σ_{yy}	85
Figure 4.20: The results of anisotropic conductivity reconstructed using AHJS algorithm for the experimental phantom (a) True conductivity σ_{xx} (b) True conductivity σ_{yy} (c) Reconstructed σ_{xx} (d) Reconstructed σ_{yy}	86

Figure 4.21: The results of anisotropic conductivity reconstructed using AHEPP algorithm for the experimental phantom (a) True conductivity σ_{xx} (b) True conductivity σ_{yy} (c) Reconstructed σ_{xx} (d) Reconstructed σ_{yy} 87

Figure 4.22: Illustration of current density minimality in corner pixels of the simulation phantom. (a) Total current density in horizontal current injection profile (b) x component of the total current density along the specified red line in (a). As it is illustrated in the (b) the current density along the selected line is minimum for the pixels in corner points. The negative picks of current density in the diagram (b) is due to rapid transitions of the current lines when leaving the recessed part of the electrode. (c) x component of the total current density in the middle line of the simulation phantom (green line)91

Figure 4.23: The performance chart of the four J -based algorithms93

LIST OF ABBREVIATIONS

AEPP	Anisotropic Equipotential Projection
AHEPP	Anisotropic Hybrid Equipotential Projection
AJS	Anisotropic J-Substitution
DAC	Digital to Analog Converter
EPP	Equipotential Projection
EIT	Electrical Impedance Tomography
FEM	Finite Element Method
FOV	Field Of View
MRCDI	Magnetic Resonance Current Density Imaging
MRCTI	Magnetic Resonance Conductivity Tensor Imaging
MREIT	Magnetic Resonance Electrical Impedance Tomography
MRI	Magnetic Resonance Imaging
PWM	Pulse Width Modulation
SNR	Signal to Noise Ratio
UMRAM	Ulusal Manyetik Rezonans Arařtırma Merkezi

CHAPTER 1

INTRODUCTION

1.1 Electrical Properties of Tissues

Electrical properties of biological tissues may vary with physiological state of the tissue. This can be useful in identifying and monitoring the probability of an illness or presence of abnormalities [1]. These properties determine the current flow pathways through different organs. Knowledge of these properties can be useful in a variety of biomedical applications such as, modeling tissues to investigate action potential propagations, estimating therapeutic current distribution during electrical stimulation and monitoring physiological functions [2].

Among these properties, “the electrical conductivity of a biological tissue is affected by its composition, structure, concentration and mobility of ions in intra- and extra-cellular fluids, amounts of those fluids, temperature and other factors” [3]. Therefore, the conductivity value of the various biological materials is different. Recognizing these differences by obtaining the conductivity map of the biological tissues inside the body can provide significant information about pathological conditions of internal organs, which is not available from other imaging modalities.

For instance, “tumors generally have higher water content than normal cells because of cellular necrosis but also, irregular and fenestrated vascularization. In addition, differences may exist in the membrane structure. Although an increased conductivity may be used to identify the presence of tumors” [2].

1.1.2 Anisotropy of Tissues

Electrical anisotropy which is observed in some biological materials such as bones, *myocardial fiber*, skeletal muscles, ligaments or blood vessels is related to presence of different fibers that are folded together in their structure [4]. These fibers are actually the very long cells. For instance in the case of skeletal muscle, fibers are wrapped together densely, and the electrical conduction in the longitudinal direction of fibers is much more than the transversal route. Because the transversal route is actually the extra cellular region and is less conductive than the cell inside [2]. On the other hand, the anisotropy is a frequency-dependent phenomenon that can be disappeared by increasing the injected current frequency. For instance in the case of muscle tissue and for frequencies beyond several MHz the anisotropy disappears. Then this property should be evaluated in a specific range of frequencies related to that biological material.

1.2 Electrical Impedance Tomography

Electrical Impedance Tomography (EIT) is an imaging technique to produce cross-sectional conductivity images from a conductive distribution and was proposed first by Henderson and Webster [5]. In this technique, current patterns are injected to the conductive region by using a set of surface electrodes and simultaneous measurements of currents and voltages are performed in the boundary. This data is used by EIT reconstruction algorithms to determine the conductivity distribution inside the volume conductor [6]. Brown and Barber [7] published the first EIT tomographic images.

But, this technique suffers from many practical and theoretical drawbacks like “errors in boundary shape and electrode positions, high and uncontrollable contact impedance of skin” [5] along with poor and space dependent spatial resolution of the reconstructed images due to the limited number of electrodes placed on the boundary. Another problem in this technique is the low sensitivity of the measured data at the boundary to conductivity variations inside the object. This inherent insensitivity of the boundary data to internal conductivity changes even worsens with distance from the surface. In other words, the spatial resolution differs for inner regions, and regions close to the boundary. Theoretically, this can be solved by voltage measurements directly from inner regions of the object, but this cannot be achieved non-invasively [8]. Highly non-uniform sensitivity and ill-posedness of the EIT inverse problem along with the poor spatial resolution, make conventional EIT unfeasible for clinical applications.

1.3 Magnetic Resonance Electrical Impedance Tomography

To overcome the EIT’s main problems namely the space-dependent spatial resolution and the low sensitivity of the measured data at the boundary to conductivity perturbations inside the object, Scott and Joy [9] proposed using the Magnetic Resonance Imaging (MRI) to measure internal current density. In this technique, the currents are injected externally to the object using surface electrodes, consonant with a conventional MRI spin-echo pulse sequence. In this way, the magnetic field due to the injected currents is obtained by extraction from the resultant MRI phase images. Then by using the Ampere’s law given in (1.1),

$$J = \frac{\nabla \times B}{\mu_0} \quad (1.1)$$

Current density data inside the object is obtained. This technique is named as Magnetic Resonance Current Density Imaging (MRCDI).

In (1.1), $\mathbf{J} = (J_x, J_y, J_z)$, $\mathbf{B} = (B_x, B_y, B_z)$ and μ_0 is magnetic permeability of free space.

To have all three components of B and consequently J , an object rotation inside the main magnet is needed, because only the magnetic field component which is aligned with the z direction of the main magnet can be calculated using MRI.

By using this current density data which is obtained from MRCDI technique and applying the relevant algorithms, the absolute conductivity images of the object can be obtained with high resolution and uniform sensitivity. This technique is named as Magnetic Resonance Electrical Impedance Tomography (MREIT) and proposed first by Zhang [10] and Woo *et al* [11].

Zhang [10] indeed, combined the two EIT and CDI techniques to obtain the conductivity distribution inside the object by using several boundary voltage measurements of EIT and internal current density distribution measurements of CDI. The relation between potential differences on the surface points ($\Delta\varphi$) and the current density J , is as given in (1.2).

$$\Delta\varphi = \int_l \rho \vec{J} \cdot \vec{dl} \quad (1.2)$$

Where, ρ is the resistivity of the object distribution and l is any contour for line integral which connects two surface measurement points.

In numerical implementation, if the imaging region is discretized to M pixels, each with constant conductivity, for N boundary voltage measurements the equation (1.2) is reduced to a linear system of equations as given in (1.3):

$$\Delta\varphi_{N \times 1} = G_{N \times M} \rho_{M \times 1} + n_{N \times 1} \quad (1.3)$$

Where, G is the internal current density data matrix, ρ is the unknown resistivity distribution vector and n is the noise data vector, for M pixels and N boundary voltage measurements.

The solution of this linear system of equations gives the unknown resistivity (conductivity) values on the imaging region. Despite this, the technique suffers from the need for many boundary voltage measurements to result a solution with a high spatial resolution.

Woo *et al* [11], proposed a new method based on minimizing an error function in terms of resistivity distribution, which models difference between measured current density data using CDI technique and the current density which is obtained from computer simulation model using the Finite Element Method (FEM). Beside the advantages, this technique suffers from low spatial resolution and poor convergence to true resistivity values because of non-effective usage of inside current density data.

Another method was proposed by Ider and Birgül [12], which is based on calculation of a sensitivity matrix relating the measured magnetic field due to the injected currents, to the conductivity distribution of the object using FEM and Biot-Savart law. In this technique, it is claimed that conductivity perturbations inside the imaging object causes a change in the magnetic field distribution due to the changes in the injected current. As it is possible to measure these magnetic field alternations with equal sensitivity throughout the entire region using MRI, the conductivity distribution map of the object can be obtained with uniform spatial resolution by applying the reconstruction algorithms [13, 14].

Eyüboğlu *et al* [15] and Özdemir *et al* [16], proposed a technique that uses the current density distribution measured by MRCDI, along with surface potential measurements of EIT, to reconstruct absolute conductivity images with high and space independent spatial

resolution. The principle of this method is based on the fact that the current density vectors are perpendicular to the equipotential lines in any pixel of the imaging object in an isotropic distribution. In this way, by using the current density data, it is possible to project the measured surface potentials, into the imaging region and assign a potential value to each pixel and calculate the potential gradient. Then for imaging region $(x, y) \in S$, by using the measured current density data J , and the calculated potential gradient $\nabla\varphi$, the conductivity distribution can be obtained using (1.4).

$$\sigma(x, y) = \frac{|J(x, y)|}{|\nabla\varphi(x, y)|} \quad (1.4)$$

In 2002, another reconstruction algorithm was proposed by Kwon *et al* [17] to produce cross-sectional static conductivity images of a resistive distribution. The method is indeed an iterative algorithm which relates numerically, the conductivity of the object distribution to the current density data which is due to the injected currents. They called this method as J substitution algorithm. In this procedure, a cost functional is introduced according to the solution of the following boundary value problem (BVP) given in (1.5).

$$\nabla \cdot \left(\frac{1}{\rho} \nabla V_\rho \right) = 0 \quad \text{in } \Omega \quad (1.5)$$

This BVP is solved for a given conductivity distribution $\sigma (= \frac{1}{\rho})$, and the Neumann boundary condition which is given in (1.6) and for the mathematical body model Ω .

$$\frac{1}{\rho} \frac{\partial V_\rho}{\partial n} = J_i \quad \text{on } \partial\Omega \quad (1.6)$$

In the above equations, J_i represents the current density at the boundary $\partial\Omega$, and n denotes the normal unit vector outward on $\partial\Omega$.

By minimizing the cost functional in (1.7), an update equation is resulted to use in the iterative method.

$$\Psi(\rho) := \int_{\Omega_s} \left| J(r) - \frac{1}{\rho(r)} E_\rho \right|^2 dr \quad (1.7)$$

In the equation (1.7), $J(r)$ represents the magnitude of the measured current density, E_ρ is the magnitude of the electric field strength obtained from solving the equation (1.5) under the constraint of (1.6) by using the FEM.

It is also claimed that, to reconstruction of absolute conductivity value at least two current injection patterns is needed along with the one surface potential measurement. The injected current patterns should not be parallel to each other. Namely, the currents satisfy the inequality which is given in (1.8).

$$|J^1 \times J^2| \neq 0 \quad (1.8)$$

In a later study, Khang *et al* [18] represented phantom experiments for static resistivity imaging by J substitution algorithm, using a 0.3 Tesla MRI scanner and saline phantoms.

Boyacıoğlu and Eyüboğlu [19] proposed another J substitution algorithm which is actually the combination of two MREIT reconstruction algorithms namely, the equipotential projection (EPP) and the J substitution algorithms. This hybrid algorithm uses the EPP's resultant conductivity distribution as the initial conductivity value for the J substitution algorithm.

In 2007, Değirmenci and Eyüboğlu [20] proposed a novel MREIT reconstruction algorithm using equipotential projection to image anisotropic conductivity distributions without any surface voltage measurements and gave the simulation results. Before that,

almost all of the studies in the field of MREIT reconstruction algorithms assumed isotropic conductivity distribution, which is actually may not be realistic for some of the biological tissues. Because as it is mentioned in [1] and [2] most of the pathological materials and biological tissues have anisotropic conductivities. In this study, the anisotropic conductivity is taken as a tensor $\bar{\sigma}$ which is defined in two dimensions as given in (1.9), instead of the one dimensional scalar conductivity value σ as it is considered in the isotropic MREIT reconstruction algorithms.

$$\bar{\sigma} = \begin{bmatrix} \sigma_{xx} & \sigma_{xy} \\ \sigma_{yx} & \sigma_{yy} \end{bmatrix} \quad (1.9)$$

Therefore, the boundary value problem in (1.5) and (1.6) which is also the forward problem of the MREIT changes to (1.10).

$$\nabla \cdot (\sigma \nabla \varphi)(x, y) = 0 \quad (x, y) \in S \quad (1.10)$$

$$\bar{\sigma} \frac{\partial \varphi}{\partial n} = \begin{cases} J_i & \text{at positive current electrode} \\ -J_i & \text{at negative current electrode} \\ 0 & \text{elsewhere} \end{cases} \quad (1.11)$$

In (1.10), S is the imaging region. In the case of anisotropic conductivity it is known that the equipotential lines are not perpendicular to the current density vectors. The calculation of the angle between the current density data and the equipotential lines in each pixel is given in 3.1.2.

In 2009, Değirmenci and Eyüboğlu [21] proposed the anisotropic J -substitution and anisotropic hybrid J -substitution algorithms to reconstruction of the anisotropic conductivity distribution, in a simulation study.

These studies gave birth to a slightly different MREIT reconstruction algorithms called Magnetic Resonance Conductivity Tensor Imaging (MRCTI), which is explained in [22]

as a simulation study. [23] Includes the practical realization and the phantom experiments of MRCDI.

In general, MREIT and MRCTI conductivity reconstruction algorithms can be divided into, two main groups:

1. The algorithms that use current density data or J -based algorithms, which need object rotation in the main magnet to obtain all three components of current density.
2. The algorithms which use the induced magnetic flux density due to the injected currents directly, or B -based algorithms. The exclusivity of the B -based algorithms is, not requiring object rotation because the related reconstruction algorithms use only the z component of the induced magnetic flux density in conductivity reconstruction procedure. This property of the B -based algorithms reduces the total imaging time and measurement errors due to object rotation, but causes different errors in the reconstructed images.

All of the algorithms which are explained and implemented in this thesis are current density based reconstruction algorithms.

In 2008, Kim *et al* [3] performed an *in vivo* animal imaging experiment of a canine brain using a 3T MRI system with home-built STR RF coil and implementing isotropic Harmonic B_z algorithm of CoReHA program [24] and injecting 5 mA current pulses. They reported that the white matter of the imaged canine brain appeared more conductive than the gray matter for equivalent isotropic conductivity images as the result.

In another study, Kim *et al* [25] proposed the first *in vivo* human experiment in this field which was the high resolution conductivity imaging of the human leg using Harmonic B_z algorithm of the isotropic MREIT [26, 27]. In the study like the previous one a 3T MRI scanner device is used to measure the internal magnetic flux density due to the externally injected currents to the imaging region. Carbon-hydrogel electrodes with thin and large surface area are used to inject 9mA current pulses with 15ms durations in harmony with

the proper spin-echo pulse sequence. They reported that the reconstructed conductivity images show quite different and unique contrast information in comparison to the conventional MRI magnitude images. In addition, because of the electrical safety considerations, the lower extremity of the human body is chosen as the imaging region.

Similar studies are performed in [28] and [29] on the canine male pelvis and canine brain to evaluate ischemia and abscess using 3T magnetic resonance system and CoReHA MREIT package software. Kim *et al* [30], performed another experiments to support the clinical significance of the MREIT reconstructed conductivity images and showing the fact that this method can provide meaningful diagnostic information that is not available from other imaging modalities.

Kim Y T [31] proposed a new multi-echo pulse sequence (Explained in Section 2.2) to obtain the conductivity images of the human lower extremity using CoReHA MREIT package software and injecting 3mA current pulses. In addition, the chemical shift artifact correction method is explained and implemented in this study to increase the quality of the reconstructed conductivity images.

Woo E J [32] showed the capability of the MREIT techniques to reconstruct the conductivity images with 1mm pixel size, by applying currents less than 1mA using a 3T MRI scanner and utilization of the previously introduced multi-echo ICNE pulse sequence along with using the high performance RF coils. The experimental results also are given in the same study.

Oh T I [33] proposed another application of the conductivity images in detection of internal temperature distribution in radiofrequency ablation or hyperthermia via recovering electrical conductivity by MREIT to control their outputs and diagnose (recognize) the treatment effect.

In a recent study, Meng Z J [34] proposed numerical simulations of MREIT conductivity imaging for brain tumor detection using realistic three-dimensional head model and adding realistic noise levels which are obtained from the used 3T MRI system and reported “that tumor-like anomalies with 200% conductivity contrast can straightforwardly be both detected and imaged by an existing 3T system using total acquisition times below 30 minutes.” [34]

1.4 Objectives of the Thesis

As it is mentioned in the previous section, conductivity imaging of the biological tissues can provide meaningful diagnostic information that is not available from other imaging modalities. Furthermore, it is mentioned that some of the biological materials have anisotropic conductivity which cannot be reconstructed truly using the isotropic reconstruction algorithms. Therefore, the anisotropic conductivity reconstruction algorithms in MREIT named as MRCTI are proposed by Değirmenci and Eyüboğlu [20, 21, 22]. The phantom experiments of the MRCTI technique using the 0.15T METU-EE MRI System, is given in [23].

As the experimental results reported by Değirmenci and Eyüboğlu [23] are obtained using an MRI device with a low field strength, the main objective of this thesis is performing the MRCTI experiments using 3T UMRAM MRI System. Furthermore, a novel anisotropic hybrid reconstruction algorithm namely, the Anisotropic Hybrid Equipotential Projection (AHEPP) Algorithm is proposed in Section 2.4.4 and the related experimental results are given in Chapter 4. In addition, an error formula is defined to evaluate the accuracy of the reconstruction algorithms in phantom experiments. Also, a scaling method is proposed and implemented to obtain the scaled version of conductivity distribution, from the reconstructed relative conductivity images of the simulation models and phantom experiments, to use in error calculation.

1.5 Outline of the Thesis

In Chapter 2, the theory and methodology of the current density imaging (MRCDI) and the related formulations along with phase unwrapping concept is given in detail. Thereafter, forward and inverse problems of the anisotropic conductivity imaging (MRCTI) is explained comprehensively.

In Chapter 3, the used experimental setup during this thesis which consists of the MRI device, current source and the experimental phantom, are introduced and explained.

Chapter 4, covers the experimental results which are obtained from the phantom experiments, along with the simulation results and the related discussions for each case. Furthermore, the reconstructed conductivities are evaluated using error measures. In addition, an SNR level is attributed to the experiments of this thesis and a method for scaling the relative reconstructed conductivity is given in detail.

Chapter 5, includes the final conclusions of this study and future work.

CHAPTER 2

METHODOLOGY OF CURRENT DENSITY AND ANISOTROPIC CONDUCTIVITY IMAGING USING MAGNETIC RESONANCE IMAGING SYSTEM

2.1 Introduction

In this chapter, the theory behind the conductivity imaging using magnetic resonance system is given in detail. From one perspective, the whole procedure of conductivity imaging using the MRI system can be divided into two main steps. Firstly, extraction of the magnetic flux density due to the injected currents to the imaging region from the MR complex or phase images. This can be considered also as the forward problem of the conductivity imaging and in the case of calculating current density data from the obtained magnetic flux density it is known as the Magnetic Resonance Current Density Imaging (MRCDI). Secondly, the inverse problem namely, the Magnetic Resonance Electrical Impedance Tomography (MREIT) which can be divided into forward and inverse problems itself. Section 2.2, explains the MRCDI procedure and the related formulations. Section 2.2.1, gives a definition of phase wrap and a general explanation about the unwrapping algorithm.

In Section 2.3, the forward problem of the anisotropic MREIT is introduced and explained. The inverse problem of anisotropic MREIT consists of the reconstruction algorithms and will be explained comprehensively in Section 2.4.

2.2 Magnetic Resonance Current Density Imaging (MRCDI)

Generally, the purpose of MRCDI technique is to extract the current density distribution inside the imaging object, using the MRI phase images. Magnetic flux density is introduced to the MR phase images by injecting or inducing currents in to the imaging region in synchrony with an appropriate MRI pulse sequence. This data can be used directly in the B -based MREIT reconstruction algorithms or can be utilized in calculation of the current density using Ampere's law (1.1), to use in the J -based MREIT algorithms. Here, it is important to note that only the magnetic flux density component which is parallel to the MR main magnetic field can be measured by MRI system. But as it is illustrated in (2.1) for calculation of x and y components of the current density (J_x, J_y), all three components of the magnetic flux density are needed.

$$J_x = \frac{1}{\mu_0} \left(\frac{\partial B_z}{\partial y} - \frac{\partial B_y}{\partial z} \right) \quad (2.1)$$

$$J_y = \frac{1}{\mu_0} \left(\frac{\partial B_x}{\partial z} - \frac{\partial B_z}{\partial x} \right)$$

Where, B_z, B_x and B_y are the induced magnetic flux density components due to the injected currents to the object in z, x and y directions respectively.

Therefore, an object rotation should be done to align the two other orientations of the object with the z direction of the main magnet.

A conventional spin echo pulse sequence (without current pulse line) is shown for one TR , in Figure 2.1. Acquired MRI signal using this pulse sequence is given in (2.2).

$$S(k_x, k_y, t) = \int_x \int_y M(x, y) e^{j[\gamma B(x, y)t + \theta_c + k_x x + k_y y]} dy dx \quad (2.2)$$

Where, $M(x, y)$ represents the transverse magnetization, γ is the gyromagnetic ratio of hydrogen, $B(x, y)$ is the component due to the main magnetic field inhomogeneity and θ_c is a constant phase which is added to spin echo MR signal because of instrumentation and receiver circuits. Also k_x is equal to $\gamma G_x(t - T_E)$ for echo signals where, G_x represents the frequency-encoding gradient which maps a time signal to a k -space signal, t is acquisition period and T_E is the echo time of signal. Similarly, $k_y = \gamma G_y T_{pe}$ where, G_y represents the phase-encoding gradient and T_{pe} stands for phase encoding gradient pulse duration [35].

By taking Fourier transform from (2.2) with respect to k_x and k_y the magnetization density can be obtained and the MR complex image including magnitude and phase data can be expressed as (2.3).

$$M_r(x, y) = M(x, y) e^{j[\gamma B(x, y)t + \theta_c]} \quad (2.3)$$

By applying currents to the imaging region in synchrony with the spin-echo pulse sequence in Figure 2.1, the applied current produces magnetic flux density components in all directions, but only the component which is parallel to the main magnetic field direction, causes a phase accumulation in the acquired MR signal, as it is given in (2.4).

$$S(k_x, k_y, t) = \int_x \int_y M(x, y) e^{j[\gamma B(x, y)t + \theta_c + \gamma B_{J_z}(x, y)T_c + k_x x + k_y y]} dy dx \quad (2.4)$$

In (2.4), the phase term $\gamma B_{J, z}(x, y)T_c$ is due to the applied current to the conductor object and $B_{J, z}(x, y)$ is the component of the magnetic flux density which is parallel with the main magnetic field. Also, T_c represents the duration of current injection or induction.

Like (2.3), by taking the Fourier transform of (2.4) the expression in (2.5) is resulted.

$$M_{r,J}(x, y) = M(x, y)e^{j[\gamma B(x,y)t + \gamma B_{J, z}(x,y)T_c + \theta_c]} \quad (2.5)$$

Here, the subscription J in $M_{r,J}(x, y)$ shows the current application.

By comparing (2.3) and (2.5), it is inferred that, difference between the two equations arises from an exponential term, $e^{\gamma B_{J, z}(x,y)T_c}$. Now by dividing the complex images with and without current injection the all phase components due to phase inhomogeneities and other artifacts are canceled and only the phase term $\gamma B_{J, z}(x, y)T_c$ remains. In other words, by performing two MRI scans with and without current flow and dividing them, the inherent phase shifts due to the magnetic field imperfections are eliminated [36]. In practical application of the method in this study and using the 3T Siemens MRI scanner, the MR phase images are available individually, and the procedure is done by subtracting the obtained two phase images directly. This way, the magnetic flux density is extracted as given in (2.6).

$$B_{J, z}(x, y) = \frac{\theta_{JN}(x, y)}{\gamma T_c} \quad (2.6)$$

In (2.6), $\theta_{JN}(x, y)$ represents the normalized phase image [9]. In other words, $\theta_{JN}(x, y)$ is the resultant phase image obtained, after unwrapping the image with current injection and subtracting it from the other phase image, which is obtained without current injection.

It is seen from (2.6), that the magnetic flux density which is extracted from normalized phase images, has a linear relation with the accumulated phase in the related MR phase

image. In other words, by increasing the injected current the phase accumulation in the MR phase image and consequently $\theta_{JN}(x, y)$ increases. But increasing the amplitude of the current is not preferred in human applications. There are other ways, to increase the obtained phase without increasing current amplitude like, using other types of pulse sequences. For instance, using the lately suggested multi-echo based MREIT pulse sequence” to utilize a remaining time after the first echo within one TR to obtain more echo signals and also to prolong the total current injection time” [31, 37, 38]. Another way, is using two opposite current injection strategy like what is done in this study. For doing so, instead of obtaining with and without current flow phase images and subtracting them, it is useful to obtain two MR images due to current application in two opposite polarities, unwrapping both of them and then subtracting them to obtain (2.7).

$$B_{J, z}(x, y) = \frac{\theta_{JN}(x, y)}{2\gamma T_c} \quad (2.7)$$

As it is seen from (2.7), by using this strategy the extracted magnetic field and consequently obtained current density is increased as twice.

As it is mentioned before, in MREIT J -based reconstruction algorithms the current density distribution data is needed, then by considering the Amperes law in (1.1) the extended form of the obtained current density is calculated as it is given in (2.8).

$$J = \frac{1}{\mu_0} \left[\left(\frac{\partial B_z}{\partial y} - \frac{\partial B_y}{\partial z} \right) \hat{a}_x + \left(\frac{\partial B_x}{\partial z} - \frac{\partial B_z}{\partial x} \right) \hat{a}_y + \left(\frac{\partial B_y}{\partial x} - \frac{\partial B_x}{\partial y} \right) \hat{a}_z \right] \quad (2.8)$$

Also by considering equations in (2.1) it is seen that, to calculate the x component of the current density J_x , the derivative of B_z with respect to y ($\partial B_z / \partial y$) and the derivative of B_y with respect to z ($\partial B_y / \partial z$) is are needed. Since, B_z component of the magnetic flux density is obtained by aligning the z axis of the imaging object with the main magnetic

field, then B_z includes the information of magnetic flux density distribution in x - y plane. Therefore $(\partial B_z / \partial y)$ can be calculated using the Sobel operator as it is given in (2.9).

$$\frac{\partial B_z}{\partial y} = \frac{1}{8\Delta y} B_z ** \begin{vmatrix} 1 & 2 & 1 \\ 0 & 0 & 0 \\ -1 & -2 & -1 \end{vmatrix} \quad (2.9)$$

In (2.9), $**$ denotes the 2D convolution and Δy represents the pixel side length in y direction. Fairly complete description about Sobel operators is given in Section 3.1.2.

But, in order to calculate the $(\partial B_y / \partial z)$ the image processing techniques cannot be applied. The reason is that, the extracted B_y which is obtained by aligning the y axis of the imaging object with the main magnetic field has information of magnetic flux density distribution as a function of x and y but not z . Therefore, $(\partial B_y / \partial z)$ cannot be calculated using Sobel operators. For calculation of $(\partial B_y / \partial z)$ the definition of derivative is used as given in (2.10).

$$\frac{\partial B_y(x, y, z)}{\partial z} = \frac{\partial B_y(x, y, z_1) - \partial B_y(x, y, z_2)}{|d|} \quad (2.10)$$

In (2.10), $B_y(x, y, z_1)$ and $B_y(x, y, z_2)$ denote the two B_y images with the distance d apart from each other in z direction. Similar expressions can be attributed to the calculation of $\partial B_x / \partial z$.

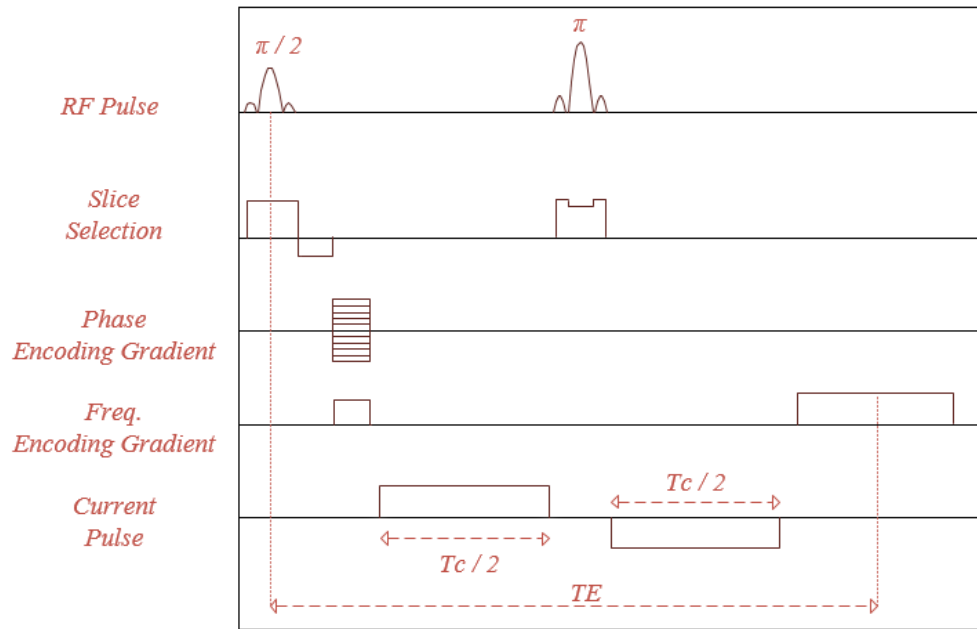


Figure 2.1: Spin Echo pulse sequence with current pulse line (MRCDI pulse sequence)

As it is seen from Figure 2.1, the current pulse polarity is reversed after the 180° RF pulse to preserve the previously accumulated phase due to the injected current between 90° and 180° RF pulses. If the polarity does not change, the accumulated phase before 180° RF pulse is canceled by the phase accumulation after it.

2.2.1 Phase Unwrapping

The concept of phase unwrapping can be explained by starting from the meaning of the phase wrap. In general, “the phase of a complex function is uniquely defined only in the principal value range” [39]. In the case of the MRI system, the obtained MR phase images are uniquely defined in the range value between $-\pi$ and π . Any phase value which is not in this interval is wrapped to $(-\pi, \pi]$. This phenomenon causes a discontinuity in the

obtained MR phase images and should be resolved to obtain correct outcome, because as it is explained in Section 2.2 the extracted magnetic flux density has a linear and proportional relation with the created actual phase image.

The all procedures which are used to remove this wrapping effect are named as unwrapping algorithms. A simple general illustration of phase wrap and the relevant unwrapped sample is shown in Figure 2.2.

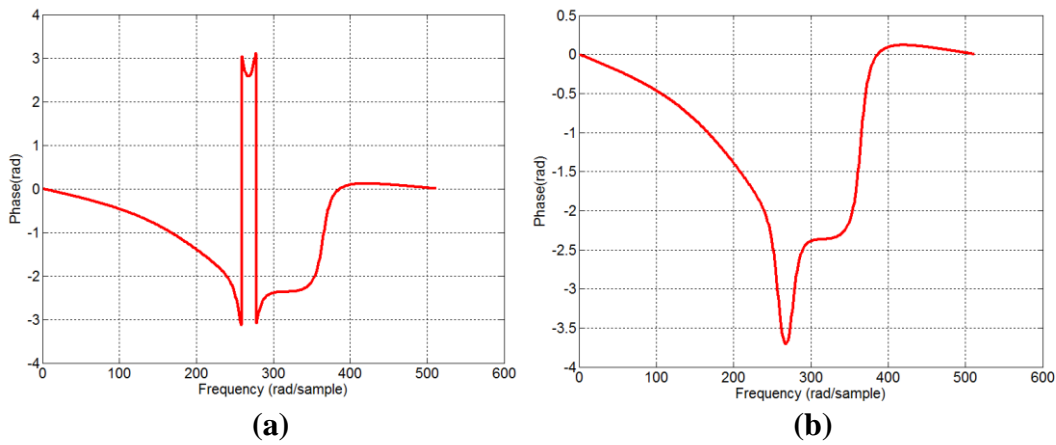


Figure 2.2: Demonstration of unwrapping: (a) Phase diagram before unwrapping (b) after unwrapping

Figure 2.2, demonstrates the phase response of a modified order 4 elliptic function lowpass filter cutting off at $f_s/4$. This phase response provides a simple example of the phase wrap concept. Figure 2.2(a), has phase wrap for the phase values smaller than -3.14 (π rad) which causes a discontinuity in the related plot, that is resolved in the unwrapped continuous phase plot in Figure 2.2(b)

Figure 2.3, illustrates phase wrap in an MR phase image. This wrapped image is related to the z component of the magnetic flux density, which is created due to the current injection

to the experimental phantom. Figure 2.3 (a) shows a phase wrap in the obtained phase image and (b) represents the unwrapped case.

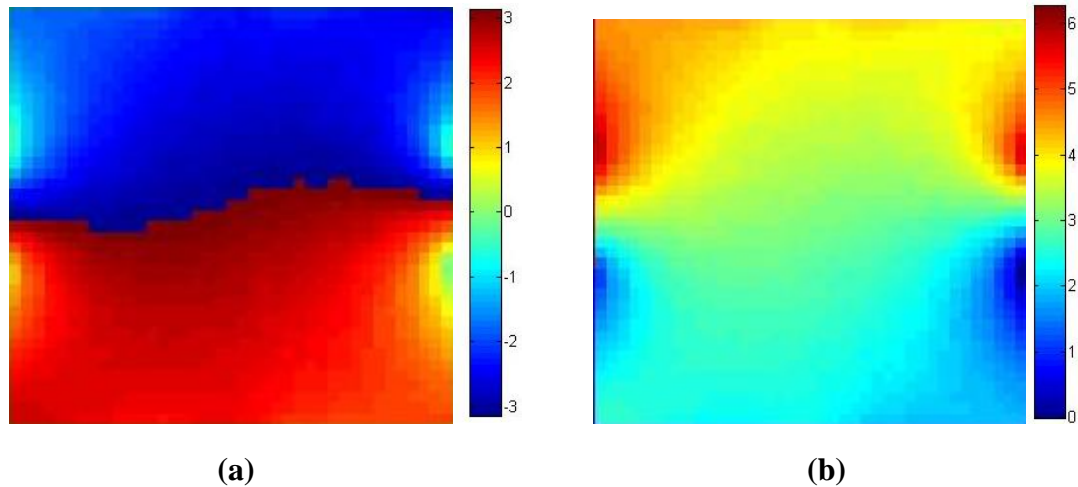


Figure 2.3: Phase wrap in an MR phase image: (a) wrapped phase image (b) unwrapped phase image.

As it is seen from Figure 2.3, the wrapped phase image is confined between $-\pi$ and π . By using a proper unwrapping algorithm the unwrapped image is resulted.

In this study, the phase unwrapping algorithm which is proposed by Liang [40] and implemented by Birgöl [41] is used.

2.3 The Forward Problem of the Anisotropic MREIT

As it is stated before, the anisotropic MREIT technique can be considered as the inverse problem of the conductivity imaging using MRI system. The anisotropic MREIT individually can be expressed as forward and inverse problems. The inverse problem of the anisotropic MREIT consists of anisotropic reconstruction algorithms which will be explained completely in detail in Chapter 3. Here, the forward problem is explained and

formulated. Generally, calculation of the magnetic flux density distribution using Biot-Savart law and surface potential calculation, by knowing the anisotropic conductivity distribution and boundary conditions are stated as anisotropic MREIT forward problem. The use of forward problem is in implementation of reconstruction algorithms like what is done in the anisotropic J -substitution algorithm in construction of cost functional as it is explained in Section 2.4.2. Another usage of forward problem, is in generation of simulation data. The start point of the forward problem is the poisson's equation in (1.5) with boundary condition in (1.6). The slightly modified form of the equation (1.5) and (1.6) for anisotropic conductivity cases is given in (2.11) and (2.12).

$$\nabla \cdot (\bar{\sigma} \nabla \varphi)(x, y) = 0 \quad (x, y) \in S \quad (2.11)$$

$$-\bar{\sigma} \frac{\partial \varphi}{\partial n} = \begin{cases} \vec{J} & \text{on positive current electrode} \\ -\vec{J} & \text{on negative current electrode} \\ 0 & \text{elsewhere} \end{cases} \quad (2.12)$$

In (2.11) and (2.12), $\bar{\sigma}$ is the conductivity tensor for 2D object distributions S , and equals to $\begin{bmatrix} \sigma_{xx} & \sigma_{xy} \\ \sigma_{yx} & \sigma_{yy} \end{bmatrix}$ and φ represents the electrical potential.

By solving the boundary value problem in (2.11) and (2.12) and obtaining the potential field distribution in the in the imaging region the electric field distribution can be expressed as (2.13).

$$E = -\nabla \varphi \quad (2.13)$$

Using the generalized form of the Ohm's law, x and y components of the current density can be obtained as it is given in (2.14).

$$\vec{j} = \bar{\sigma} \vec{E} = \begin{bmatrix} \sigma_{xx} & \sigma_{xy} \\ \sigma_{yx} & \sigma_{yy} \end{bmatrix} \cdot \begin{bmatrix} \nabla \phi_x \\ \nabla \phi_y \end{bmatrix} \quad (2.14)$$

Using Biot-Savart relation in (2.15), the magnetic flux density generated due to the current density distribution $\vec{j}(x, y)$, can be calculated as it is given in (2.15).

$$B(x, y, z) = \frac{\mu_0}{4\pi} \int \frac{\vec{j}(x, y) dS \times \hat{a}_R}{R^2} \quad (2.15)$$

In (2.15), μ_0 is the permeability of the free space, R denotes the vector from source point (x', y', z') to the field point (x, y, z) and \hat{a}_R is the unit vector in that direction.

The inverse problem of the anisotropic MREIT namely, the reconstruction algorithms are explained in detail in the next Section.

2.4 Inverse problem of MRCTI

2.4.1 Equipotential Projection Algorithm For Anisotropic Conductivity Reconstruction

2.4.1.1 Introduction

Anisotropic equipotential projection algorithm is based on the equipotential projection algorithm proposed by Eyüboğlu *et al* [15] and practically realised for the isotropic conductivity distributions by Özdemir *et al* [16]. In this technique, the current density which is calculated from the extracted magnetic flux density from MRI phase images, is used to reconstruct the anisotropic conductivity in a relative scale. To have true conductivity values at least one potential measurement at the object boundary is required to scale the resultant conductivity distribution. Magnetic flux density extraction and current density calculation are described in detail in Section 2.2. Generally, this method is an iterative algorithm, based on constructing equipotential lines in the imaging region

at each iteration. The algorithm starts with an initial conductivity distribution which is calculated previously and then, the difference between the calculated and the measured current density is minimized using a residual function, iteratively. The resultant conductivity data in each step is fed in to the algorithm as initial conductivity distribution for the next iteration.

2.4.1.2 Anisotropic Equipotential Projection (AEPP) Algorithm

The key point in anisotropic conductivity reconstruction is obtaining potential gradients in x and y directions in the field of view for 2D model. By knowing the potential gradients and possessing the internal current density distribution, the anisotropic conductivity can be calculated. By rearranging equation (2.14), $\nabla\phi_x$ and $\nabla\phi_y$ can be obtained as given in (3.1-3.2)

$$\nabla\phi_x = \frac{J_x \sigma_{yy} - J_y \sigma_{xy}}{\sigma_{xy}\sigma_{yx} - \sigma_{xx}\sigma_{yy}} \quad (2.16)$$

$$\nabla\phi_y = \frac{J_y \sigma_{xx} - J_x \sigma_{yx}}{\sigma_{xy}\sigma_{yx} - \sigma_{xx}\sigma_{yy}} \quad (2.17)$$

Where, $\nabla\phi_x$ and $\nabla\phi_y$ are the potential gradients in any pixel in the imaging region, in x and y directions. Similarly J_x and J_y are x and y components of the current density and σ values are the anisotropic conductivity components for the specified directions in any pixel. It is possible to calculate potential gradients throughout the object boundaries using equations (2.16) and (2.17). For doing this, conductivity values in the boundary columns are needed. In the experimental phantom, it is possible by assigning known conductivity values to the boundary pixels. In this way, by obtaining potential gradients along all boundaries, potential values of each boundary pixels can be determined by assigning a

value to one pixel. These potential values likely are not true potentials but satisfying the correct potential gradient distribution. That is why; the reconstructed conductivity images have relative scaling.

As it is mentioned in Section 1.3, in the case of anisotropic conductivity the current density vectors are not perpendicular to the equipotential lines. To calculate the angle between these two vectors the conductivity anisotropy at the crossing point is needed. Therefore, the ratio given in (2.18),

$$\frac{\nabla\varphi_y}{\nabla\varphi_x} = \frac{J_y \sigma_{xx} - J_x \sigma_{yx}}{J_x \sigma_{yy} - J_y \sigma_{xy}} \quad (2.18)$$

gives the tangent of $\nabla\varphi$ at any point $(x, y) \in S$ for each pixel in the imaging region, with specified current density and anisotropic conductivity values. Then the angle of $\nabla\varphi$ at this point is:

$$\alpha_{\nabla\varphi|(x,y)} = \tan^{-1} \left(\frac{J_y \sigma_{xx} - J_x \sigma_{yx}}{J_x \sigma_{yy} - J_y \sigma_{xy}} \right) \Big|_{(x,y) \in S} \quad (2.19)$$

On the other hand, it is obvious that the equipotential lines are perpendicular to $\nabla\varphi$ lines, then the angle α can express the angles of equipotential lines truly.

Since, the conductivity distribution in calculation of the initial conductivity is not known, then this procedure to find angle α , cannot be performed at first iteration. Therefore, in calculation of initial conductivity distribution the current density vectors are assumed perpendicular to the equipotential lines. By obtaining the angles for the entire field of view the potential values through the boundary columns which were calculated previously, are projected to the field of view using the current density distribution data and observance of the angle α through the equipotential lines which are constructed on the entire imaging slice. It is notable that there may be more than one equipotential line

starting from different points of same boundary pixel. However due to the definite angle between the current density vector in a pixel and the equipotential lines starting from that one, the lines follow parallel but different paths [42].

In the case of passing more than one equipotential line from a pixel in the imaging slice, the pixel's potential value can be determined as a weighted sum of the potential contributions of those equipotential lines to that pixel, as given in (2.20),

$$\varphi_n = \frac{\sum_{i=1}^N d_i e_i}{\sum_{i=1}^N d_i} \quad (2.20)$$

where, φ_n gives the pixel's potential value, N is the number of equipotential lines passing through the pixel, d_i is the length of i^{th} equipotential line in that pixel, and e_i represents the potential value of the i^{th} equipotential line.

In the case of pixels with no equipotential line passing through them, the mean potential value of the eight nonzero neighbouring pixels is assigned as the potential value of that pixel.

As it is mentioned before, the obtained φ_n is a relative value and can be used in the applications where the true values of potential and conductivity distributions are not needed. To obtain the true values, at least one potential measurement is performed most of the time from the object boundary.

By obtaining the potential values of all pixels in the imaging region, it is possible to calculate the directional potential gradients ($\nabla\varphi_x$ and $\nabla\varphi_y$) for each pixel in the imaging region, by using the concept of Sobel operators, as given in (2.21).

$$\nabla\varphi_x(x, y) = \frac{1}{8\Delta x} \begin{vmatrix} -1 & 0 & 1 \\ -2 & 0 & 2 \\ -1 & 0 & 1 \end{vmatrix} ** \varphi(x, y) \quad (2.21)$$

$$\nabla\varphi_y(x, y) = \frac{1}{8\Delta y} \begin{vmatrix} 1 & 2 & 1 \\ 0 & 0 & 0 \\ -1 & -2 & -1 \end{vmatrix} ** \varphi(x, y)$$

In (2.21), Δx and Δy represent the pixel length in x and y directions.

The Sobel operator actually is a kind of differential operators which performs a 2D spatial gradient on the obtained $\varphi(x, y)$ in the imaging region, and calculates the potential gradients in x and y directions. The operator consists of two 3×3 convolution kernels (filters), which are actually 90° rotated form of each other. Using the large convolution kernels makes filter less sensitive to noise and produce more smooth outputs, but increases the computational cost.

By obtaining the potential gradients $\nabla\varphi$ for each pixel in the imaging slice as explained and having the internal current density J measured from MRCDI technique the residual function in the imaging region S can be stated as in (2.22)

$$R = \int_S \left\| -\bar{\sigma} \cdot \nabla\varphi - \vec{j} \right\|^2 ds \quad (2.22)$$

where, $\| \cdot \|$ represents the L_2 norm.

The surface integral (2.22) can be expressed as a summation over the pixel elements as given in (2.23).

$$R = \sum_j \int_{S_j} \left\| -\bar{\sigma}_j \cdot \nabla\varphi - \vec{j} \right\|^2 ds \quad (2.23)$$

In (2.23), j is the element index, and thus S_j and $\bar{\sigma}_j$ are the surface and conductivity of the j^{th} element, respectively.

As it is mentioned in Section 2.4.1.1, the residual function is minimized at each iteration with respect to $\bar{\sigma}_j$ by setting the condition in (2.24).

$$\frac{\partial R}{\partial \bar{\sigma}_j} = 0 \quad (2.24)$$

By minimizing the residual function R , with respect to all $\bar{\sigma}_j$ elements separately the system of equations can be obtained as given in (2.25).

$$J_x^j = \sigma_{xx}^j \nabla \varphi_x^j + \sigma_{xy}^j \nabla \varphi_y^j \quad (2.25)$$

$$J_y^j = \sigma_{yx}^j \nabla \varphi_x^j + \sigma_{yy}^j \nabla \varphi_y^j$$

In (2.25), J_x and J_y represent the current density components of the j^{th} element, which has anisotropic conductivities σ_{xx}^j , σ_{xy}^j , σ_{yx}^j , σ_{yy}^j and potential gradients $\nabla \varphi_x^j$ and $\nabla \varphi_y^j$ in x and y directions.

Equation (2.25) is obtained for one current injection pattern and be seen that, there are two equations with four unknown conductivities, therefore this system of equations cannot be solved, because at least four equations are needed to solve this equation set. To overcome this problem at least two different current injection patterns are needed to obtain four independent equations.

The internal current density \vec{J} in (2.23) is a measured distribution. If the obtained potential values and consequently the resultant potential gradients in the imaging region are scaled with a scaling factor to obtain true values, then the system of four independent equations

will have a unique solution. Otherwise, a relative distribution is obtained which is not unique. In this study the four and six current injection profiles are examined to obtain better conductivity distribution.

Totally for N different current injection patterns in the whole imaging region S , the system of equations can be expressed as it is given in (2.26)

$$\begin{aligned}
 J_x^1 &= \sigma_{xx} \nabla \varphi_x^1 + \sigma_{xy} \nabla \varphi_y^1 \\
 J_x^2 &= \sigma_{xx} \nabla \varphi_x^2 + \sigma_{xy} \nabla \varphi_y^2 \\
 &\vdots \\
 &\vdots \\
 J_x^N &= \sigma_{xx} \nabla \varphi_x^N + \sigma_{xy} \nabla \varphi_y^N
 \end{aligned} \tag{2.26}$$

$$\begin{aligned}
 J_y^1 &= \sigma_{yx} \nabla \varphi_x^1 + \sigma_{yy} \nabla \varphi_y^1 \\
 J_y^2 &= \sigma_{yx} \nabla \varphi_x^2 + \sigma_{yy} \nabla \varphi_y^2 \\
 &\vdots \\
 &\vdots \\
 J_y^N &= \sigma_{yx} \nabla \varphi_x^N + \sigma_{yy} \nabla \varphi_y^N
 \end{aligned}$$

The matrix-vector form of the equation system in (2.26) can be expressed as (2.27).

$$\begin{bmatrix} J_x^1 \\ J_x^2 \\ \vdots \\ J_x^N \end{bmatrix} = \begin{bmatrix} \nabla \varphi_x^1 & \nabla \varphi_y^1 \\ \nabla \varphi_x^2 & \nabla \varphi_y^2 \\ \vdots & \vdots \\ \nabla \varphi_x^N & \nabla \varphi_y^N \end{bmatrix} \cdot \begin{bmatrix} \sigma_{xx} \\ \sigma_{xy} \end{bmatrix}, \quad \begin{bmatrix} J_y^1 \\ J_y^2 \\ \vdots \\ J_y^N \end{bmatrix} = \begin{bmatrix} \nabla \varphi_x^1 & \nabla \varphi_y^1 \\ \nabla \varphi_x^2 & \nabla \varphi_y^2 \\ \vdots & \vdots \\ \nabla \varphi_x^N & \nabla \varphi_y^N \end{bmatrix} \cdot \begin{bmatrix} \sigma_{yx} \\ \sigma_{yy} \end{bmatrix} \tag{2.27}$$

Utilizing (2.26-2.27), anisotropic conductivity values can be calculated as shown in (2.28).

$$\begin{bmatrix} \sigma_{xx} \\ \sigma_{xy} \end{bmatrix} = \begin{bmatrix} \nabla\varphi_x^1 & \nabla\varphi_y^1 \\ \nabla\varphi_x^2 & \nabla\varphi_y^2 \\ \vdots & \vdots \\ \nabla\varphi_x^N & \nabla\varphi_y^N \end{bmatrix}^{-1} \cdot \begin{bmatrix} J_x^1 \\ J_x^2 \\ \vdots \\ J_x^N \end{bmatrix}, \quad \begin{bmatrix} \sigma_{yx} \\ \sigma_{yy} \end{bmatrix} = \begin{bmatrix} \nabla\varphi_x^1 & \nabla\varphi_y^1 \\ \nabla\varphi_x^2 & \nabla\varphi_y^2 \\ \vdots & \vdots \\ \nabla\varphi_x^N & \nabla\varphi_y^N \end{bmatrix}^{-1} \cdot \begin{bmatrix} J_y^1 \\ J_y^2 \\ \vdots \\ J_y^N \end{bmatrix} \quad (2.28)$$

As it is seen from (2.28), the matrix including gradient values is not square. Therefore, the direct inverse of the matrix cannot be calculated. Instead, the singular value decomposition (SVD) method is used in the inversion procedure without truncation since, the matrix has only the two Eigen values. [42]

As it is mentioned in this chapter, this algorithm is an iterative one, and the procedure which is described in this section is iteratively repeated to result the best outcome for anisotropic distribution.

2.4.2 Anisotropic J-Substitution (AJS) Algorithm

2.4.2.1 Introduction

J-substitution algorithm which is proposed by Kwon *et al* [17] in 2002, is another current density based isotropic conductivity reconstruction algorithm for the solution of MREIT inverse problem.

In this method, to image resistivity a constructive map $\{I, J\} \rightarrow \rho$ is found inside the 2D cross section of an electrically conducting body Ω . In this constructive map, *I* represents the injected current to the region, *J* is the magnitude of the current density due to the injected currents and ρ is the resistivity of the region to be imaged. The method is an

iterative algorithm and the procedure is somehow similar to what was done in the equipotential projection based algorithm in minimizing the residual sum obtained from cost functional. The main difference between these two reconstruction algorithms is in the calculation of internal potential field inside the body which is performed in EPP by constructing equipotential lines in each iteration and projecting the boundary potentials through them in the imaging region, while in the J -substitution algorithm the internal potential distribution is obtained by solving a boundary value problem using Finite Element Method (FEM), in the entire imaging region.

Değirmenci and Eyüboğlu [21] proposed an extended version of the previously presented J -substitution algorithm, to reconstruct the anisotropic conductivities and called this method as anisotropic J -substitution algorithm, which is used in this thesis and is explained in detail in Section 2.4.2.2.

2.4.2.2 Anisotropic J -substitution algorithm

This anisotropic algorithm can be explained by using the concept of the isotropic procedure like what is done by Kwon *et al* [17] and then it can be extended to the anisotropic case.

A boundary value problem (BVP) is the starting point for the problem definition of this algorithm. For an electrically conducting body Ω with resistivity ρ , the corresponding voltage V_ρ satisfies the following BVP :

$$\nabla \cdot \left(\frac{1}{\rho} \nabla V_\rho \right) = 0 \quad \text{in } \Omega \quad (2.29)$$

$$\frac{1}{\rho} \frac{\partial V_\rho}{\partial n} = J_I \quad \text{on } \partial\Omega \quad (2.30)$$

According to (2.29) and (2.30) a cost functional can be considered as given in (2.31).

$$\Psi(\rho) := \int_{\Omega} \left| J^*(r) - \frac{1}{\rho(r)} E_{\rho}(r) \right|^2 \quad (2.31)$$

In (2.31), $J^*(r)$ represents the magnitude of the internal measured current density. On the other hand:

$$E_{\rho}(r) := |\nabla V_{\rho}(r)| \quad (2.32)$$

$E_{\rho}(r)$ represents the internal electric field intensity calculated for given ρ and by solving (2.29) and (2.30).

By discretizing the mathematical body model Ω , into N distinct elements (pixels) all with the same area Ω_k , and by considering (2.31) the following squared residual sum R is obtained as given in (2.33).

$$R(\sigma_0, \dots, \sigma_{N-1}) := \sum_{k=0}^{N-1} \int_{\Omega_k} |J^*(r) - \sigma_k E_{\rho}(r)|^2 dr \quad (2.33)$$

Here, $\sigma_k = \frac{1}{\rho_k}$ is the conductivity of the k^{th} element Ω_k , which is assumed to be constant in a pixel area. In addition, the electric field intensity $E_{\rho}(r)$ in (2.33), is a function of $(\sigma_0, \dots, \sigma_{N-1})$.

Then, to update the resistivity from the zero gradient argument for the minimization of the squared residual sum a differentiation is performed over (2.33) with respect to σ_m for $m = 0, \dots, N-1$ as shown in (2.34).

$$0 = \frac{\partial R}{\partial \sigma_m} = 2 \int_{\Omega_m} E_\rho(r) (\sigma_m E_\rho(r) - J^*(r)) dr +$$

$$2 \sum_{k=0}^{N-1} \int_{\Omega_k} \sigma_k \frac{\partial E_\rho(r)}{\partial \sigma_m} (\sigma_k E_\rho(r) - J^*(r)) dr \quad (2.34)$$

For $m = 0, \dots, N-1$, if r_k be the center point of the element Ω_k , using the quadrature rule for approximating the integral in the first part of (2.34), the following equation is resulted:

$$0 \approx E_\rho(r_m) (\sigma_m E_\rho(r_m) - J^*(r_m)) +$$

$$\sum_{k=0}^{N-1} \sigma_k \frac{\partial E_\rho(r_k)}{\partial \sigma_m} (\sigma_k E_\rho(r_k) - J^*(r_k)) \quad (2.35)$$

Now, the updating strategy to minimize the residual sum in (2.33) for isotropic conductivity cases is calculated for $m = 0, \dots, N-1$ as given in (2.35).

$$\frac{1}{\bar{\rho}_m} = \bar{\sigma}_m := \frac{J^*(r_m)}{E_\rho(r_m)} \quad (2.35)$$

In (2.35), $\bar{\sigma}_m$ is the newly calculated conductivity value for the body model element Ω_m , by using the $E_\rho(r_m)$ value, which was calculated at the center point of the Ω_m using the conductivity distribution in the previous iteration.

Now, to generalize the procedure to anisotropic conductivity problems, the scalar conductivity value σ in (2.35) should be replaced by a 2×2 conductivity tensor $\bar{\sigma} = \begin{bmatrix} \sigma_{xx} & \sigma_{xy} \\ \sigma_{yx} & \sigma_{yy} \end{bmatrix}$ for a 2D body model.

Similar to AEPP algorithm no initial conductivity distribution is existed at the beginning. Therefore, an isotropic, homogeneous conductivity distribution is fed to the algorithm to

utilise in FEM structure construction, as a starting point. Also similar to the AEPP algorithm, to find an updating equation, residual sum in (2.33) is constructed for anisotropic case and is differentiated for minimization. By minimizing the residual function R , with respect to all $\bar{\sigma}_j$ elements separately the system of equations can be obtained for one current profile injection as given in (2.36).

$$J_x^j = \sigma_{xx}^j \nabla \varphi_x^j + \sigma_{xy}^j \nabla \varphi_y^j \quad (2.36)$$

$$J_y^j = \sigma_{yx}^j \nabla \varphi_x^j + \sigma_{yy}^j \nabla \varphi_y^j$$

In (2.36), J_x and J_y represent the current density components of the j^{th} element, which has anisotropic conductivities $\sigma_{xx}^j, \sigma_{xy}^j, \sigma_{yx}^j, \sigma_{yy}^j$ and potential gradients $\nabla \varphi_x^j$ and $\nabla \varphi_y^j$ in x and y directions.

Similar to what was mentioned before in Section 2.4.1.2, the equation (2.36), is obtained for one current injection pattern and it is seen that, there is two equations with four unknown conductivities. Therefore, this system of equations cannot be solved, since at least four equations are needed to solve this equation set. To overcome this problem at least two different current injection patterns are needed to obtain four independent equations.

Totally for N different current injection patterns in the whole imaging region S , the system of equations can be expressed as given in (2.37).

$$\begin{aligned}
J_x^1 &= \sigma_{xx} \nabla \varphi_x^1 + \sigma_{xy} \nabla \varphi_y^1 \\
J_x^2 &= \sigma_{xx} \nabla \varphi_x^2 + \sigma_{xy} \nabla \varphi_y^2 \\
&\vdots \\
&\vdots \\
J_x^N &= \sigma_{xx} \nabla \varphi_x^N + \sigma_{xy} \nabla \varphi_y^N
\end{aligned} \tag{2.37}$$

$$\begin{aligned}
J_y^1 &= \sigma_{yx} \nabla \varphi_x^1 + \sigma_{yy} \nabla \varphi_y^1 \\
J_y^2 &= \sigma_{yx} \nabla \varphi_x^2 + \sigma_{yy} \nabla \varphi_y^2 \\
&\vdots \\
&\vdots \\
J_y^N &= \sigma_{yx} \nabla \varphi_x^N + \sigma_{yy} \nabla \varphi_y^N
\end{aligned}$$

The matrix-vector form of the system equation in (2.37) can be expressed as given in (2.38).

$$\begin{bmatrix} J_x^1 \\ J_x^2 \\ \vdots \\ J_x^N \end{bmatrix} = \begin{bmatrix} \nabla \varphi_x^1 & \nabla \varphi_y^1 \\ \nabla \varphi_x^2 & \nabla \varphi_y^2 \\ \vdots & \vdots \\ \nabla \varphi_x^N & \nabla \varphi_y^N \end{bmatrix} \cdot \begin{bmatrix} \sigma_{xx} \\ \sigma_{xy} \end{bmatrix}, \quad \begin{bmatrix} J_y^1 \\ J_y^2 \\ \vdots \\ J_y^N \end{bmatrix} = \begin{bmatrix} \nabla \varphi_x^1 & \nabla \varphi_y^1 \\ \nabla \varphi_x^2 & \nabla \varphi_y^2 \\ \vdots & \vdots \\ \nabla \varphi_x^N & \nabla \varphi_y^N \end{bmatrix} \cdot \begin{bmatrix} \sigma_{yx} \\ \sigma_{yy} \end{bmatrix} \tag{2.38}$$

Using (2.37-2.38), anisotropic conductivity values can be calculated as shown in (2.39).

$$\begin{bmatrix} \sigma_{xx} \\ \sigma_{xy} \end{bmatrix} = \begin{bmatrix} \nabla\varphi_x^1 & \nabla\varphi_y^1 \\ \nabla\varphi_x^2 & \nabla\varphi_y^2 \\ \vdots & \vdots \\ \nabla\varphi_x^N & \nabla\varphi_y^N \end{bmatrix}^{-1} \cdot \begin{bmatrix} J_x^1 \\ J_x^2 \\ \vdots \\ J_x^N \end{bmatrix}, \quad \begin{bmatrix} \sigma_{yx} \\ \sigma_{yy} \end{bmatrix} = \begin{bmatrix} \nabla\varphi_x^1 & \nabla\varphi_y^1 \\ \nabla\varphi_x^2 & \nabla\varphi_y^2 \\ \vdots & \vdots \\ \nabla\varphi_x^N & \nabla\varphi_y^N \end{bmatrix}^{-1} \cdot \begin{bmatrix} J_y^1 \\ J_y^2 \\ \vdots \\ J_y^N \end{bmatrix} \quad (2.39)$$

As it is deduced from (2.39), the matrix including gradient values is not square. Therefore, the direct inverse of matrix cannot be calculated. Instead, the singular value decomposition (SVD) method is used in inversion procedure without truncation, because the matrix has only the two Eigen-values.

Further, in this algorithm as well as the AEPP, at least one potential measurement is needed to obtain true conductivity values.

2.4.3 Anisotropic Hybrid J-Substitution (AHJS) Algorithm

Actually this algorithm is not an independent method. However, it is a beneficial combination of two previously explained algorithms, AEPP and AJS. In this method which is mainly based on the anisotropic J -substitution algorithm, the initial conductivity distribution which was assumed to be homogenous and isotropic in the starting point of AJS, is considered to be the final best result of conductivity distribution obtained from the AEPP algorithm for the same imaging region with anisotropic conductivity [21]. The purpose of this combination is to obtain a faster convergence and to gain the positive sides of both algorithms. However, the algorithm is highly dependent on the outcome of the AEPP algorithm as the initial conductivity. Hence, any undesirable AEPP result damages the AHJS algorithm as well, which can be the weak point of this algorithm.

2.4.4 Anisotropic Hybrid Equipotential Projection (AHEPP) Algorithm

One of the drawbacks of the Anisotropic Equipotential Projection algorithm (AEPP) is in calculation of the initial conductivity distribution. As it is explained in Section 2.4.1.2, in this algorithm, to project the obtained boundary potential values in to the imaging region the equipotential lines are constructed in the imaging region at each iteration. These equipotential lines are constructed, using the current density distribution data and observing the defined angle in equation (2.19) between the current density vectors and the equipotential lines. By considering the equation (2.19) it is obvious that, to obtain the mentioned angle the conductivity distribution in all anisotropic directions in 2D ($\sigma_{xx}, \sigma_{xy}, \sigma_{yx}, \sigma_{yy}$) is needed.

However, in the first iteration of the algorithm the conductivity distribution inside the imaging region is not known. Therefore, an isotropic distribution is assumed for the first step, because as it is mentioned before in Section 1.3, in the case of isotropic conductivity distribution the equipotential lines in each pixel are perpendicular to the current density vector on that pixel. This initial assumption, can cause an undesirable erroneous result for the initial conductivity distribution. When this weakness of the algorithm is associated with inherent vulnerability of the AEPP algorithm to the experimental data noise, the resultant reconstructed image could not contain any valuable information about the anisotropic conductivity distribution in the imaging region. A phenomenon that despite the expectations is not corrected by applying more iterations, but rather even worsens by increasing the number of iterations.

For improvement of this drawback, an alternative way is considered in this thesis. Instead of calculating an erroneous initial conductivity by isotropic assumptions, it is possible to assign the obtained anisotropic conductivity distribution from the J -substitution algorithm, as the initial conductivity to obtain an acceptable relative contrast image. Another reason for using this method, is the high speed performance of the AEPP in

comparison with the J -substitution algorithm. Normally, performing 20 iterations using the J -substitution algorithm to obtain the desired result gets about 36 minutes using Intel Core i7 CPU at 2.8 GHz and 4 GB of RAM, whereas performing the same number of iterations using AEPP algorithm lasts only 1.5 minutes. Therefore, by performing one iteration in J -substitution algorithm and passing the results to the AEPP algorithm as the initial conductivity distribution, the entire reconstruction time does not exceed 3 minutes.

The performance of the four explained anisotropic J -based algorithms is examined using the 3 Tesla magnetic resonance system in this study (Chapter 4) by reconstructing the conductivity distribution of the experimental phantom to scrutinize the efficiency of each algorithm and finding the strengths and weaknesses of them. In addition, the simulation models are prepared based on the experimental phantom properties to be used in experimental data error calculation procedure.

CHAPTER 3

EXPERIMENTAL SETUP FOR MRCTI AT 3 TESLA MRI SYSTEM

3.1 Introduction

In this chapter, the experimental setup which is used in data acquisition for the MRCTI experiments, is introduced and explained briefly.

Hardware of almost all of the conventional MREIT experiments consist of these three major parts:

1. Magnetic Resonance Imaging system,
2. Controllable Current Source
3. Experimental Phantoms.

Among these three, the Magnetic Resonance Imaging (MRI) system is a completely separate imaging modality which is used to obtain magnitude and phase images from the experimental phantom. A controllable current source produces bipolar current pulses during specific time intervals, in synchrony with a proper spin echo pulse sequence.

The MRI scanner which is used in this study is a device manufactured by Siemens® (Figure 3.1). The MRI system has a 3T main magnetic field intensity, 70cm bore size and 45mT/m gradient strength [43]. The data collection is performed using the embedded single channel body coil of the MR scanner.



Figure 3.1: The 3 Tesla MRI scanner used in this thesis located at National Magnetic Resonance Research Center (UMRAM) at Bilkent University

3.2 Pulse Sequence Generation

The spin echo pulse sequence and the additional triggers are prepared by using the Siemens pulse sequence programming software IDEA® (Integrated Development Environment for Application). Using this program, different parameters of the pulse sequence can be adjusted by user, considering the software and hardware limitations of the scanner. RF and gradient pulses, readout events, external triggers, required gradient

amplitude and phase encoding parameters along with entire sequence timing procedure and many other parameters can be designated using this program. Furthermore, a unit test option is assigned to test the new designed pulse sequences whether it is applicable to the scanner. After the unit test successes, the sequence is compiled with a proper compiler in order to use in the scanner.

3.3 Current Source

Current pulse generation is the starting point of the conventional MREIT experiments. As it is mentioned in Chapter 2, the injected currents to the electrically conductive phantom produce magnetic field in all directions. But only the component of this magnetic field which is parallel with the MR main magnetic field direction can be measured by the magnetic resonance imaging methods because, only this component of the magnetic field produces a phase accumulation in the related MR phase image. By extracting this phase, like what is done in Section 2.2, the current density distribution is obtained in the imaging region.

The current source which is used in the Anisotropic MREIT experiments of this study is designed and manufactured in [44]. This current source has several features like, constant and load independent current injection capability, MR compatible structure to avoid RF noise, being programmable to inject currents in synchrony with the MRI pulse sequence, and multi-channel current injection. The schematic diagram of the current source is given in Figure 3.2.

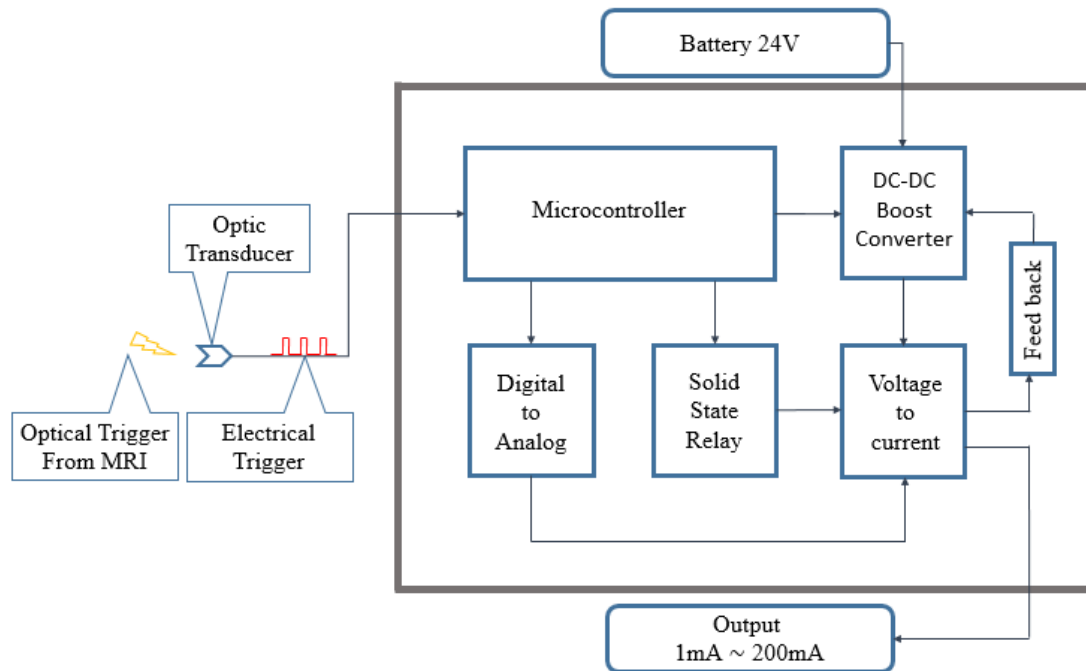


Figure 3.2: Schematic diagram of the used current source [44]

As it is mentioned above, the current source is programmable to work in a synchronized manner with the used pulse sequence. Figure 3.3, demonstrates a conventional spin-echo sequence with the injected current pulse, along with an additional line to demonstrate timing strategy of the triggers which are required in data acquisition. These triggers, are added to the pulse sequence using IDEA[®] software as optic signals with 1ms duration. These optical signals are converted to 3.3V analog triggers to activate the microcontroller unit of the current source for determination of the current injection instant, duration, amplitude and polarity as it is specified in Figure 3.3.

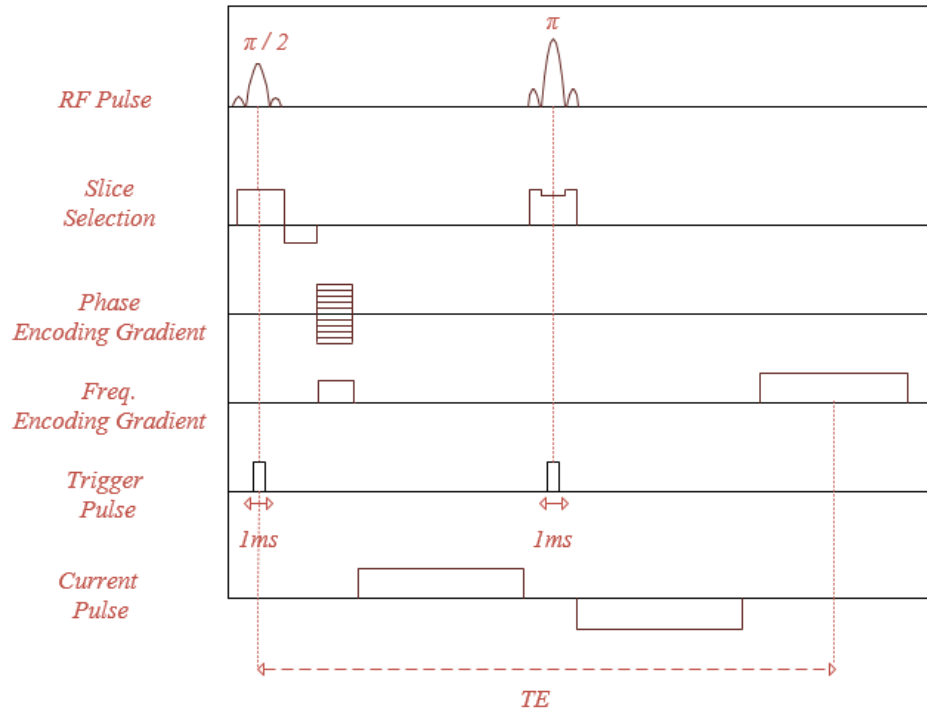


Figure 3.3: Spin-echo pulse sequence for MREIT experimental data acquisition.

In this experimental setup, the programmed triggers with the specified duration come from the MRI scanner via an optic fiber in the form of a red optic signal which turns off when the trigger existed and turns on rest of the time. The optic receiver which is used in this setup to conversion of optic signals to 0 and 3.3V analog voltages is HFBR-2528Z Receiver [45]. Recommended receiver application circuit of the HFBR-2528Z is given in Figure 3.4.

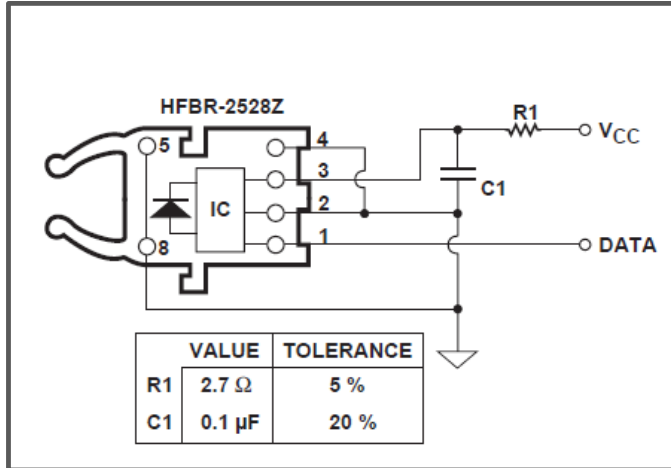


Figure 3.4: Fiber optic receiver circuit (Avago HFBR-2528Z)

After activation of the microcontroller unit by the trigger pulses, this unit sends a start pulse to boost converter to produce required high voltage. Simultaneously, an 8-bit digital signal is sent to the digital to analog converter (DAC) unit to determine the amplitude of the current which will be injected. This amplitude along with other parameters like duration of injection, delay time and the injecting channels are determined by the user from a graphical user interface of the microcontroller. Meanwhile, another 8-bit digital signal is sent by the microcontroller to solid state relays to determine the user selected channels for current injection.

3.3.1 Boost Converter

The above mentioned boost converter is a step-up DC-to-DC power electronic converter with a nonlinear dynamic behavior that creates a greater output voltage than the source voltage. Schematic diagram of boost converter which is used in the structure of the current source is given in Figure 3.5.

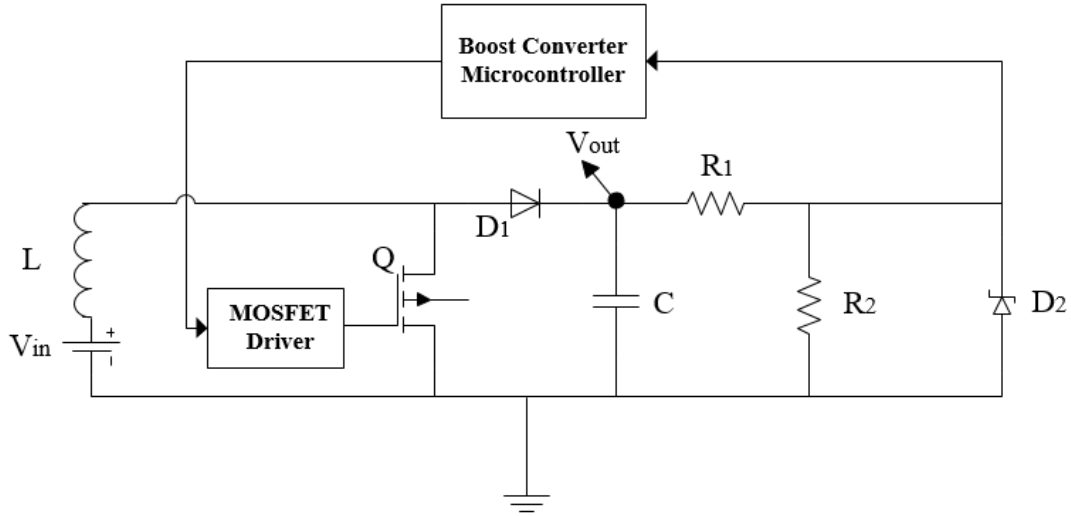


Figure 3.5: Diagram schematic of the step-up DC-DC boost converter [44]

The operating principle of the step-up DC-DC converter is based on the tendency of inductor to resist abrupt changes in current by creating and destroying a magnetic field. A high voltage capacitor C , in the boost structure is continuously charged by switching action of a power MOSFET. Simultaneously, the output voltage of the boost is divided over R_1 and R_2 (Figure 3.5) to obtain a voltage value between 0 and 3.3V across R_2 . This voltage is sent to PIC24 family microcontroller with a hysteresis control feedback. In order to perform the switching behavior, microcontroller arranges the duty cycle of the generated pulse width modulation (PWM) signal according to the received feedback voltage (0-3.3V). Hereby, the desired output voltage is obtained in a sustained manner. When continuous conduction mode is assumed, general gain relationship of a step-up DC-DC converter is as given in (3.1).

$$\frac{V_{out}}{V_{in}} = \frac{1}{1 - D} \quad (3.1)$$

In (3.1), D is the duty cycle of the PWM signal. [46] and [47].

3.3.2 Voltage to Current Converter

The schematic diagram of the voltage to current converter topology is given in Figure 3.6.

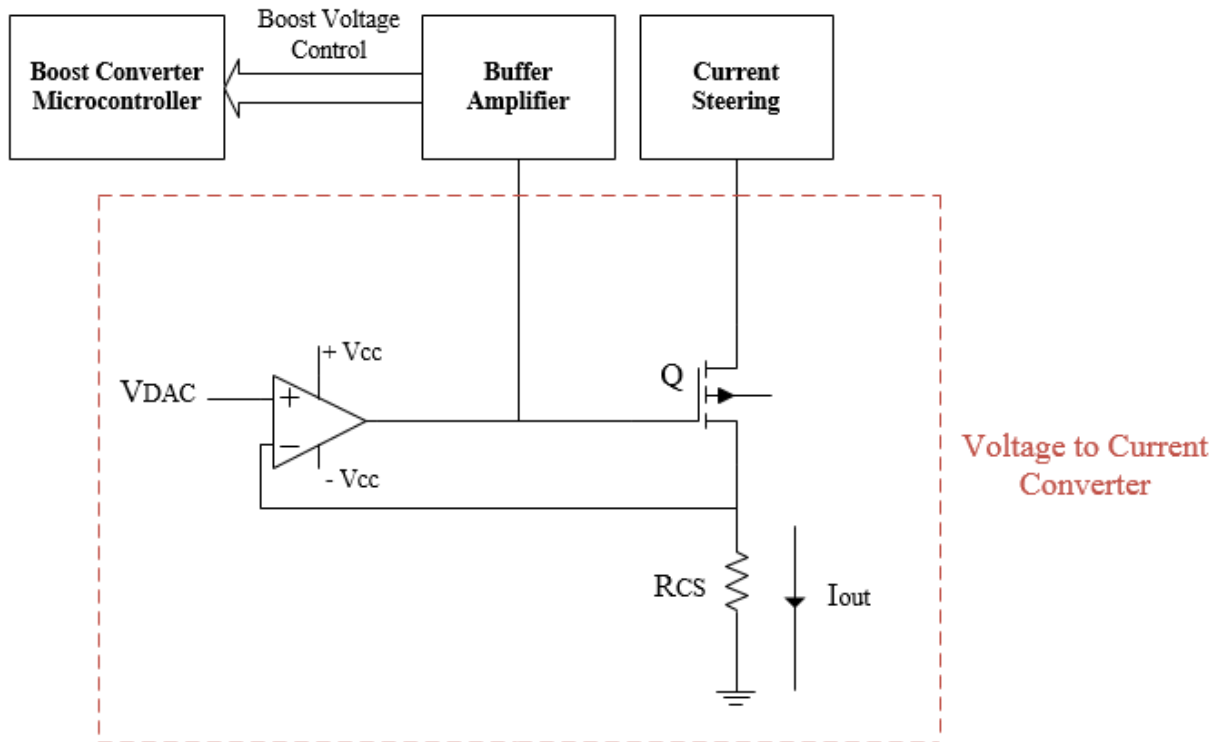


Figure 3.6: Diagram schematic of the Voltage to Current Converter [44]

In Figure 3.6, R_{cs} represents the current sensing resistor and $VDAC$, is the Digital to Analog Converter (DAC) output voltage.

In the above diagram, op-amp drives the power MOSFET and the magnitude of the output current I_{out} , can be calculated as it is given in (3.2).

$$I_{out} = \frac{V_{DAC}}{R_{CS}} \quad (3.2)$$

As it is mentioned, the current source which is used in this study has four channels which can be determined as source and sink channels independently. Therefore, current steering topology is used in the current source which is consist of eight Solid State Relays (four sink and four source relays) to determine the direction of the output current.

During the experiments the current source is outside of the MR scanner room, and the potential measurements which are needed to scale the reconstructed conductivities as it is mentioned in Section 2.4.1.2, are performed between the current injection ports.

3.4 Experimental Phantom

To evaluate the performance of different MREIT algorithms in experimental applications, phantoms are used. An experimental phantom in a MREIT measurement consists of a container which is filled with different materials to simulate the conductivity of a living organ. Materials which are used to fill the phantoms are different according to type of the experiment. In isotropic MREIT experiments, conductive and isotropic materials are placed in the imaging phantom for evaluation of conductivity reconstruction using the various isotropic algorithms. In the case of anisotropic conductivity measurements, the material which is placed in the imaging phantom should have the anisotropic conductivity itself or such a property must be created by using special arrangements. Moreover, size and physical shape of the phantom container depends on purpose of the experiment, used algorithms and hardware limitations.

Generally, the physical material of the phantom container, to use in MREIT experiments should have special properties like being nonmagnetic and non MR active because of placing in the MRI scanner. Furthermore, the container should be electrically insulator

because the current pulses are injected in to the phantom during the experiment using the electrodes at the boundary. The phantom, is designed using SOLIDWORKS[®] software and manufactured with specific features. Plexiglas material is used in the structure of the phantom body because of the reasons mentioned above and the transparency of Plexiglas which enables the user to see inside area of the phantom. The used phantom is constructed in the form of cube to create square slices in 2D, which is proportionate to the implemented algorithms. On the other hand, dimensions of the phantom container should fit with the internal size of the used MR coil. In addition, these dimensions have been designated carefully to provide the required number of pixels in the imaging region. In this study, the internal dimensions of the used phantom is designed to be 8 cm × 8 cm × 8 cm, to provide 40×40 pixels in the imaging slice in 2D, each with 2mm side length by selecting 128mm FOV in x and y directions and 64 base resolution. To eliminate the signal loss due to the high current density under the current injecting electrodes and also MRI signal void around the copper sheet electrodes due to RF signal blocking [2] near the electrodes, the recessed structure is used in electrode placement as it is shown in Figure 3.7.

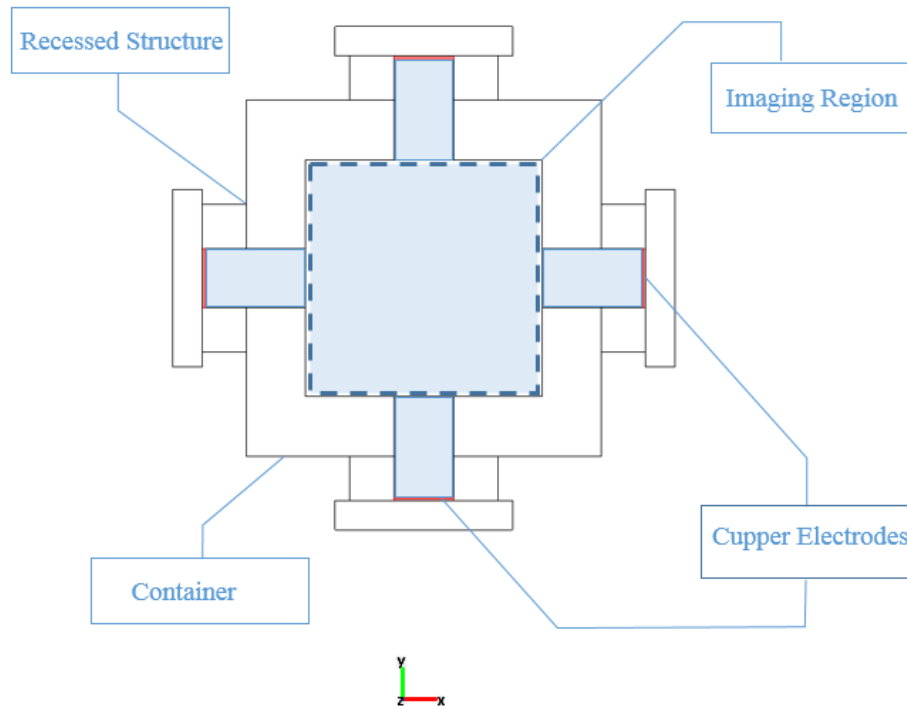


Figure 3.7: 2D representation of the experimental phantom filled with conductive solution.

The interior structure which is used in the experimental phantom to produce anisotropic conductivity behavior in macroscopic scale has a special design [42] as it is shown in Figure 3.8. It can be stated that, preparing micro scale anisotropy in the physical phantoms is almost impossible [23]. As it can be inferred from the physical shape of the current steering structure in Figure 3.9(a) and (b) the injected currents to this imaging slice in vertical path, flow through different directions due to the specific style of placing holes on the plates Figure 3.9 (c). In this way, the anisotropic ratio could be controlled according to the position. The horizontal path can be considered as fully conductive as it is illustrated in Figure 3.9 (d). The background part of the experimental phantom is filled by a solution with conductivity of 0.2 S/m , in order to simulate the blood conductivity [42].

To prepare this solution, 0.1gr CuSO_4 and 0.145gr NaCl are dissolved in 100ml pure water and mixed for 10 minutes.

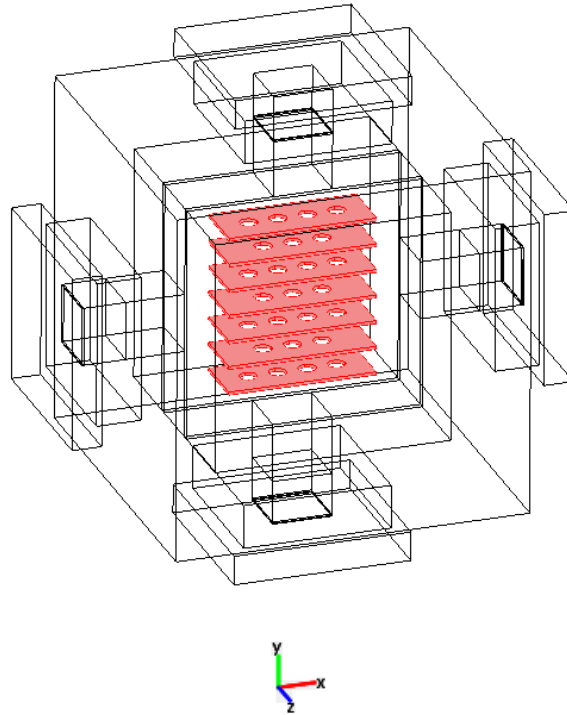
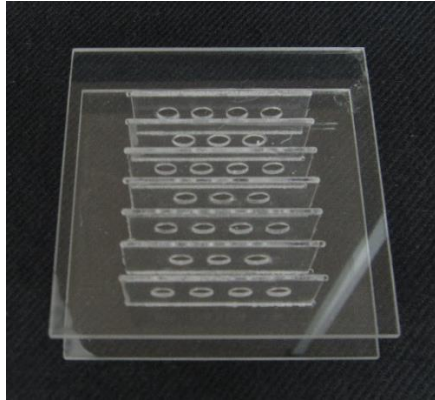
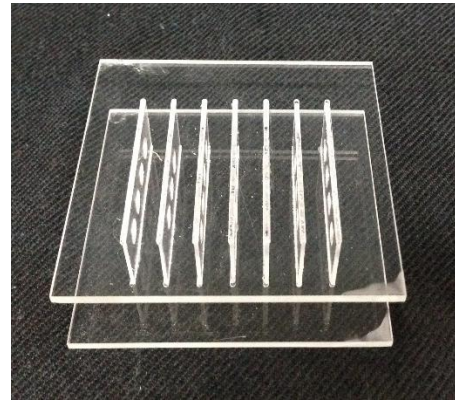


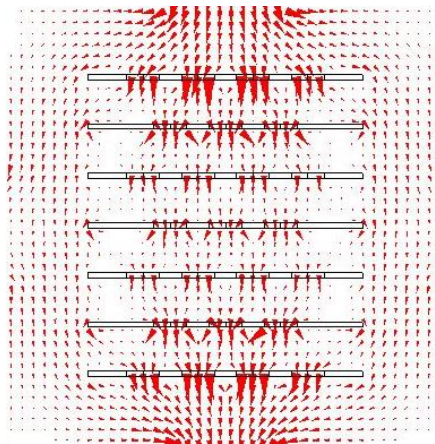
Figure 3.8: Illustration of the current steering structure in the four electrode experimental phantom.



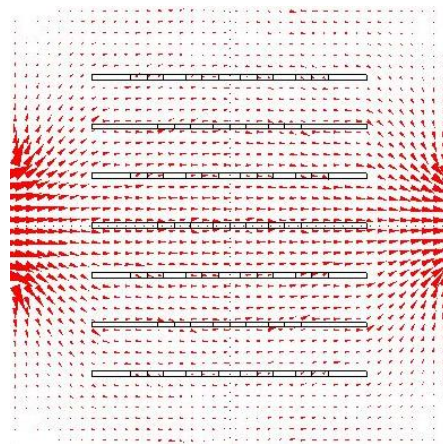
(a)



(b)



(c)



(d)

Figure 3.9: Illustration of current flow inside the phantom slice in presence of the current steering structure which is used to create macro-scale anisotropy in the background material conductivity. (a) Vertical view (b) Horizontal view (c) Vertical current injection profile (d) Horizontal current injection profile

In Figure 3.10, the experimental phantom is displayed. The figure shows a phantom with four recessed electrodes which are placed in the middle point of the container side walls. The current injection strategy using this phantom is shown in Figure 3.11. One vertical, one horizontal and four adjacent current injection profiles are performed using this phantom to image the conductivity distribution.

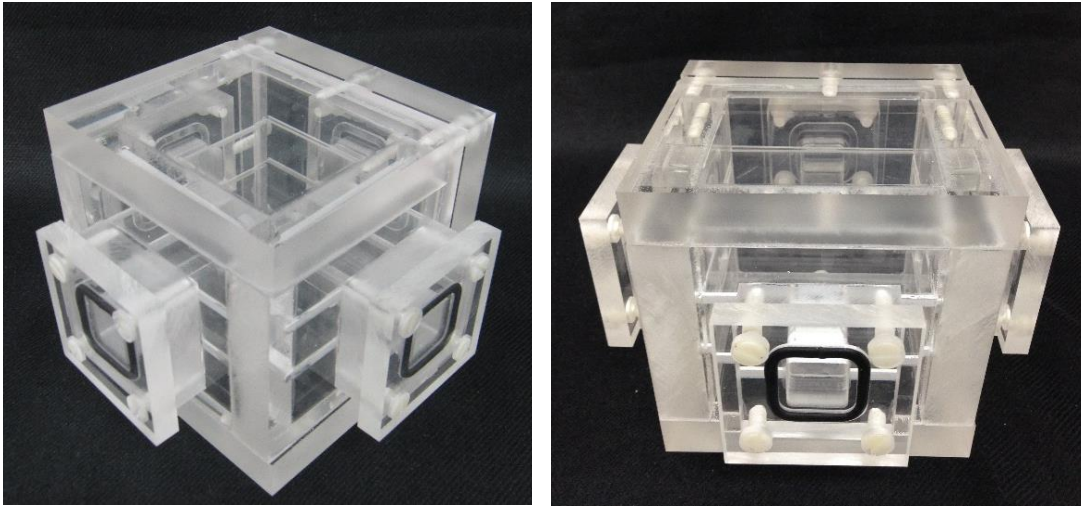


Figure 3.10: The experimental four electrode phantom

As it is explained in 2.4.1.2 and 2.4.2.2 at least two current injection profiles are needed to reconstruct the anisotropic conductivity distribution using the MRCTI algorithms. But it is useful to know that, performing more current injection profiles causes gathering more data from the imaging region and thereupon a fast convergence to the desirable conductivity with more accuracy. But using more current profiles on the other hand, causes increasing in computational operations and consequently requires high memory space and more time to data acquisition and reconstruction procedures. Therefore, a tradeoff is existed between the number of the current profiles and the memory and time consumption.

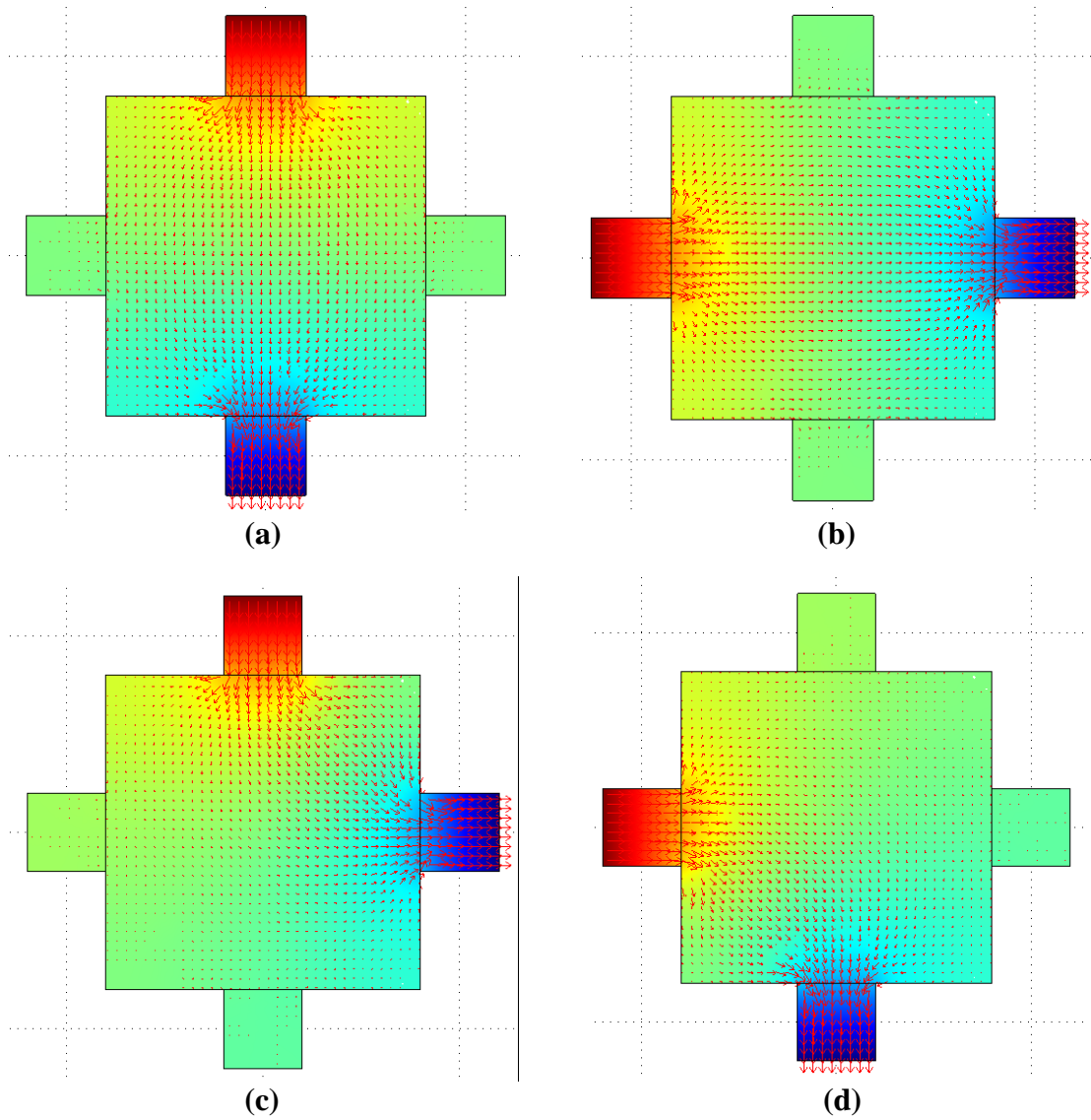


Figure 3.11: The six current injection profiles using the phantom in Figure 3.10 (a) Vertical (b) Horizontal (c) First adjacent (up and right) (d) Second adjacent (left and down) (e) Third adjacent (up and right) (f) Fourth adjacent (left and down), current injecting profiles.

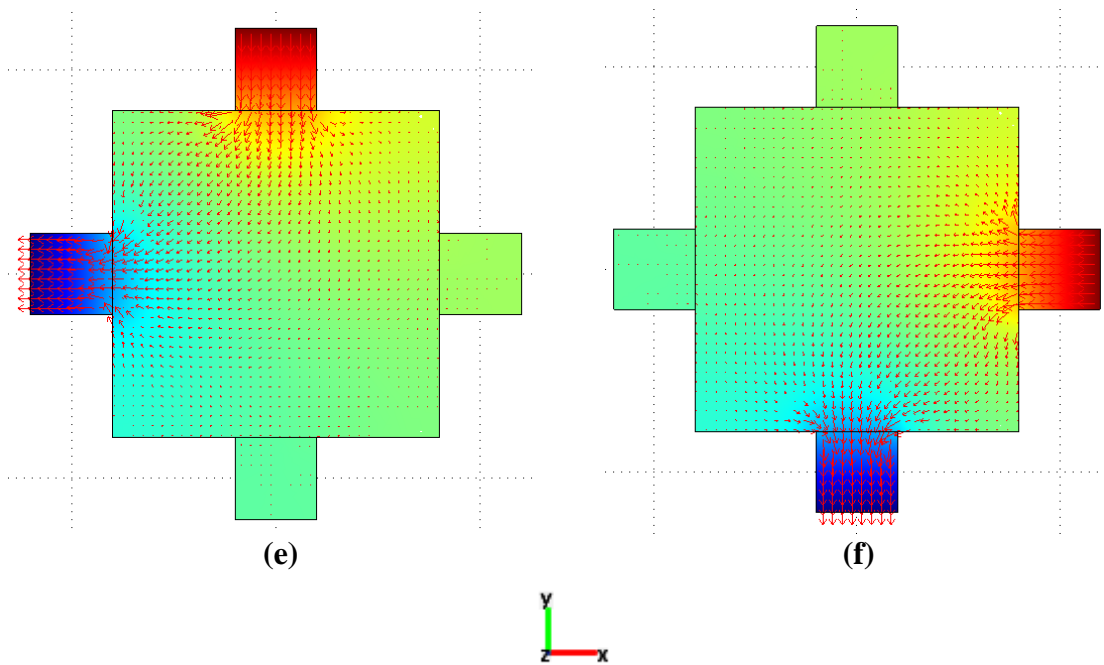


Figure 3.11: (continued)

The performed simulations showed that, using the phantom in Figure 3.10 with current steering structure shown in Figure 3.8, results in increased errors in the four corners of the obtained reconstructed conductivity images. These errors arise from the fact that the injected currents, in some certain current injection profiles does not reach to the points near the corners of the phantom and causes reconstruction of pixel conductivities with no current. This phenomena, increases the calculated error at the corners and even spreads to the neighboring pixels in the next iterations in AEPP and AJS algorithms. The obtained conductivity distributions from experimental data using this phantom (Chapter 4) confirmed this claim in the experimental application as well. Another important point should be considered in experimental data collection is, that the current cables always should be placed parallel to the main magnetic field direction. In this way, the induced magnetic field to the imaging region due to the current cables is in the perpendicular plane

to the MR main magnetic field. Therefore, the accumulated phase due to this magnetic flux density is not measured by MR system. If the position of cables toward the imaging phantom is not considered carefully, the magnetic flux density due to the currents in cables accumulates undesirable phase inside the imaging slice in the MR main magnetic field direction. This phenomenon causes an undesired dephasing in some regions near to the current cables, which can be observed in the form of regions with dark shadow in the related MR magnitude images.

Figure 3.12, shows the experimental phantom in the MR scanner and orientation of the current carrying cables toward the phantom. Furthermore, to hold the phantom in center of MR bore during the experiment, a phantom holder is designed and manufactured from the Plexiglas material.



Figure 3.12: Illustration of the experimental phantom inside the MR magnet

3.5 Conductivity Cell

In order to measure the conductivity of the materials (solutions) which are filled in the phantom as background, the conductivity cell is used. The conductivity cell which is used in this study is shown in Figure 3.13, and is made up of a 1cm×10cm×1cm Plexiglas container with two current injecting electrodes in two sides and two voltage measurement electrodes at the middle, 1cm apart from each other. The liquid material is poured into this container and the conductivity is measured using the four electrode conductivity measurement method [48].



Figure 3.13: conductivity cell

CHAPTER 4

RESULTS AND COMPARISONS

4.1 Introduction

In this chapter, the performance of the four J -based MRCTI reconstruction algorithms explained in Chapter 2, is evaluated using the experimental data. An experimental phantom is manufactured and prepared for experimental data collection as explained in Section 3.4. To measure the SNR level of the experiments, an equation is defined in Section 4.2. Furthermore, in order to quantize the accuracy of the reconstructed conductivity which is obtained from the experimental data, reconstructed conductivity is compared with the true conductivity distribution and an error measure is defined in Section 4.3. To scale the relative reconstructed conductivity a scaling factor is needed. A scaling method is introduced and implemented in Section 4.4. The pulse sequence parameters along with the parameters of the injected current used during the experiments is given in Section 4.5. Simulation results of the proposed AHEPP algorithm are illustrated in Section 4.6. Finally, the experimental results obtained from the phantom experiments along with the simulation results and error calculations for each case are demonstrated in Section 4.7.

4.2 SNR Calculation

In order to attribute an SNR level to the experiments performed in this study, the formulation given in (4.1) is used for SNR calculation in 2D.

$$SNR = K \cdot \left(\frac{FOV_x}{N_x} \cdot \frac{FOV_y}{N_y} \cdot \Delta z \right) \cdot \sqrt{\frac{N_x \cdot N_y \cdot NEX}{BW}} \quad (4.1)$$

In (4.1), K is a constant value which depends on hardware factors of the MRI system such as the coil configuration, pre-amp and noise power spectrum, field strength dependent factors and also the applied pulse sequence parameters. This constant can be taken as unity in approximate calculations of SNR to study the effect of changing other experimental parameters like field of view (FOV), slice thickness, number of frequency and phase encoding steps, and averaging number. FOV_x and FOV_y , determine the field of view in x and y directions, N_x and N_y are the number of frequency and phase encoding steps, Δz is the slice thickness, NEX represents the number of averaging and BW stands for the receive bandwidth.

By substituting the experimental parameters used in the data acquisition process during this study and taking the constant value K as unity the approximate experimental SNR is obtained equal to 26.

The parameters used during experiments are as given in Table 4.1.

Table 4.1: The experimental parameter values used in SNR calculation.

FOV_x	$128mm$
FOV_y	$128mm$
<i>Number of Frequency Encodings (N_x)</i>	64
<i>Number of Phase Encodings (N_y)</i>	64
<i>Number of Signal Averaging (NEX)</i>	16
<i>Slice Thickness (Δz)</i>	$6mm$
<i>Band width (BW)</i>	54.528 KHz

The receive bandwidth can be calculated as it is given in (4.2).

$$BW = FOV \cdot \gamma \cdot G \quad (4.2)$$

In (4.2), γ is the gyromagnetic constant of hydrogen which is equal to 42.6 MHz/T and G represents the gradient field strength which is taken to be 10 mT/m in the prepared spin-echo pulse sequence using the IDEA pulse sequence programming software.

As it is inferred from equation (4.1), by enlarging the field of view, increasing the number of signal averaging and using wider slice thickness, it is possible to increase the SNR level of the experiment. But, it is obvious that the total time of data acquisition procedure increases drastically by enlarging the FOV and increasing the number of averaging. In addition, the width of the slice thickness is limited by the experimental phantom structure and dimensions. In the experiments, the size of FOV in x and y direction along with the

number of frequency and phase encoding steps are taken to be exactly the same values given in Table 4.1 in order to obtain desirable $2\text{mm} \times 2\text{mm}$ pixel size in the imaging region as it is given in (4.3).

$$\begin{aligned}\Delta x &= \frac{FOV_x}{N_x} \\ \Delta y &= \frac{FOV_y}{N_y}\end{aligned}\tag{4.3}$$

In (4.3), Δx and Δy represent the image pixel side length in x and y directions.

4.3 Error Calculation

In order to evaluate the accuracy of the reconstructed conductivity images from the experimental data, an error measure is defined as it is given in (4.4).

$$\varepsilon_{\sigma_n} = \sqrt{\frac{1}{N} \sum_{j=1}^N \frac{(\sigma_{jt_u} - \sigma_{jr_u})^2}{\sigma_{jt_u}^2}} \times 100\% \tag{4.4}$$

In (4.4), σ_{jt_u} and σ_{jr_u} are the true and reconstructed conductivity values of the j^{th} pixel in anisotropic conductivity direction u (xx, yy) respectively and N is the total number of pixels in the conductivity image.

To obtain a true conductivity distribution of the experimental phantom for the measurement of the error value using (4.4), a simulation model is prepared in COMSOL software. In the simulation, a 3D numerical model of the experimental phantom is constructed with same dimensions, boundary conditions and sub-domain properties of the MRCTI experiment and the forward problem of the MRCTI is solved. As mentioned in Section 2.3, one of the applications of the MRCTI forward problem is in generation of

simulation data. Therefore, by solving the 3D model using FEM, the potential distribution and the current density data can be obtained for a known background conductivity distribution in the imaging region and specified boundary conditions, in the selected slice. By knowing the potential distribution in the selected slice it is possible to calculate the directional gradients of potential in x and y directions ($\nabla\phi_x, \nabla\phi_y$) for each pixel in the simulated imaging region. By rearranging the Ohm's law in equation (2.14), the anisotropic conductivities for each pixel can be calculated as it is given in (4.5).

$$\sigma_{xx} = - \frac{J_x}{\nabla\phi_x}$$

$$\sigma_{yy} = - \frac{J_y}{\nabla\phi_y}$$
(4.5)

In (4.5), J_x and J_y represent the current density components in x and y directions at the center point of each pixel. In the same way, $\nabla\phi_x$ and $\nabla\phi_y$ represent the potential gradient in x and y directions for each pixel in the imaging region [15], [16].

4.4 Scaling Factor Calculation

As it is mentioned in Section 2.4.1.1, a scaling factor is needed to calculate true conductivity values from relative conductivity distribution images obtained from MRCTI reconstruction algorithms. Also it was declared in Section 3.3 that a voltage measurement is done between the two current injecting electrodes for each current profile to scale the reconstructed images.

4.4.1 Scaling the relative reconstructed conductivity distribution by calculating the potential values in the boundary pixels for an unknown conductivity distribution in the imaging region

In this method, by measuring the potential difference between the two current injecting electrodes for each current injection profile during the experiment and knowing the isotropic conductivity value of the background material in the outermost boundary pixels, the scaling factor is calculated prior to obtaining the conductivity distribution in the imaging region.

The procedure is based on calculation of the potential gradients in the boundary pixels, by knowing the current density data and the conductivity values on those pixels. As it is explained in Section 3.5, a conductivity cell is used to measure the conductivity value of the prepared background material. In this study, the background material of the experimental phantom is a solution with the specified synthetics as explained in Section 3.4. In this way, by obtaining the conductivity value of each pixel in the outermost boundary rows and columns, and knowing the current density components (J_x and J_y) for each boundary pixel the gradient values are calculated. Therefore, for the outermost upper and lower boundary pixels of the experimental phantom, potential gradients can be calculated using equation (4.6).

$$\nabla\varphi_x = -\frac{J_x}{\sigma} \quad (4.6)$$

Similarly, to calculate the potential gradient for each pixel element in the outermost right and left boundaries of the experimental phantom the equation (4.7) is used.

$$\nabla\varphi_y = -\frac{J_y}{\sigma} \quad (4.7)$$

By obtaining the gradient values for all boundary pixels the electrical potential can be calculated for each boundary pixel.

The procedure starts from assigning the measured potential value during the experiment to the pixels under the current injecting electrodes. As it is illustrated in Figure 4.1, for the measured potential difference V , between the two electrodes during the experiment, the source electrode of the prepared model is assigned to possess the voltage value V , when the sink electrode is set to zero potential (the sink electrode is taken as reference).

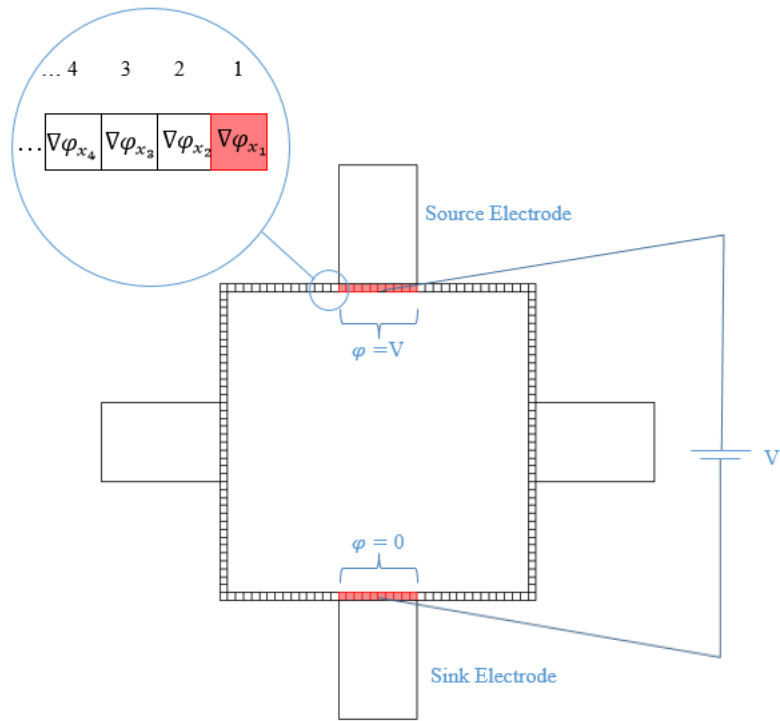


Figure 4.1: Illustration of the boundary pixels along with the assigned voltage values to the source and sink electrodes in the vertical path.

To understand the procedure of potential calculation for the entire boundary pixels in a specific current injection profile, the potential value is calculated for the pixel number 2

and vertical current path as it is illustrated in Figure 4.1. As it is seen from Figure 4.1, the pixel number 2 is located next to the last pixel under the current injecting electrode. Therefore, potential value of the previous pixel (pixel number 1) is known. In this way, potential value of the second pixel can be calculated using the equation (4.8).

$$\varphi_2 = \varphi_1 + \frac{\nabla\varphi_{x_2} + \nabla\varphi_{x_1}}{2} \cdot \Delta x \quad (4.8)$$

In (4.8), $\nabla\varphi_{x_1}$ and $\nabla\varphi_{x_2}$ are the gradient values of the first and the second pixels respectively (Figure 4.3). Δx is the pixel side length in x direction and φ_1 is the assigned potential value for the pixels under the source electrode which equals to V . Similarly, the potential value of the third pixel in Figure (4.1) can be calculated, by knowing the potential value of the second pixel. In general, equations in (4.9) and (4.10) are used to calculate the potential values through the entire boundary pixels.

$$\varphi_{i+1} = \varphi_i + \frac{\nabla\varphi_{x_{i+1}} + \nabla\varphi_{x_i}}{2} \cdot \Delta x \quad (4.9)$$

$$\varphi_{i+1} = \varphi_i + \frac{\nabla\varphi_{y_{i+1}} + \nabla\varphi_{y_i}}{2} \cdot \Delta y \quad (4.10)$$

Equation (4.9) is used to calculate the potential values of the pixels in the most upper and the lower boundaries. In the same way, equation (4.10), is applied for the most right and the most left boundaries of the experimental phantom. An example of potential calculation in boundary pixels, to scale the relative reconstructed conductivity is given in Figure 4.2.

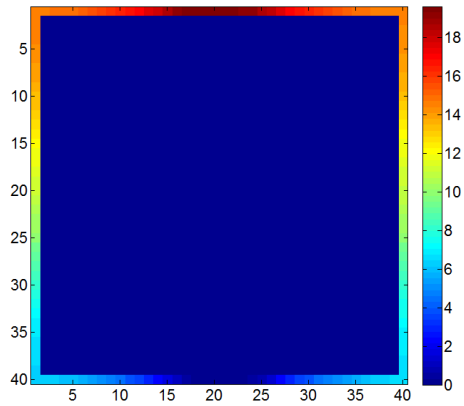


Figure 4.2: The potential value distribution on the boundary pixels of the used experimental phantom and measured voltage in vertical current injection profile.

The potential difference measured between the two current injecting electrodes for the vertical path (Figure 4.2) during the experiment was equal to 19V.

4.5 Pulse Sequence Parameters

The experimental parameters of the applied spin echo pulse sequence along with the injected current parameters are given in Table 4.2, and illustrated in Figure 4.3.

Table 4.2: The experimental parameters of the used pulse sequence and the injected current

<i>TR</i>	<i>250ms</i>
<i>TE</i>	<i>60ms</i>
<i>Number of Signal Averaging</i>	<i>16</i>
<i>Duration of the injected current in forward direction</i>	<i>20ms</i>
<i>Duration of the injected current in inverse direction</i>	<i>20ms</i>
<i>Forward Delay</i>	<i>5ms</i>
<i>Inverse Delay</i>	<i>5ms</i>
<i>Trigger Duration</i>	<i>1ms</i>
<i>Current Amplitude</i>	<i>10mA</i>

Furthermore, it is remarkable to note that the TR and TE values which is used in the experimental data acquisition, is selected by considering the role of these two factors in noise reduction of the obtained current density data and acquiring maximum SNR level [37].

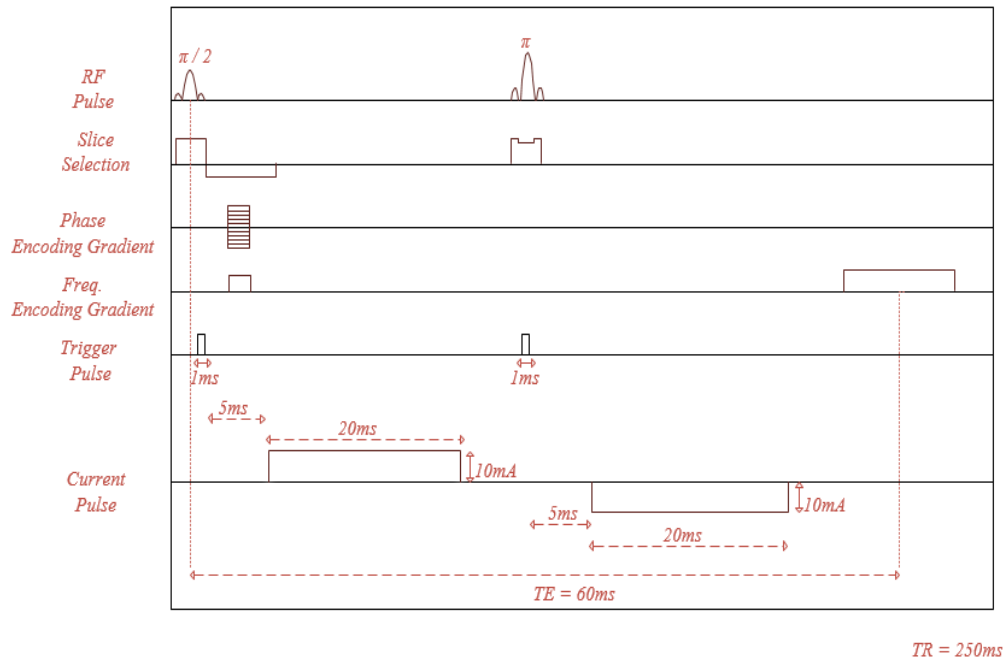


Figure 4.3: Timing diagram of the spin echo pulse sequence with current injection

4.6 Simulation Results of the Proposed AHEPP Algorithm

In order to compare the performance of the proposed AHEPP algorithm with the results of the other three J -based MRCTI algorithms in [21, 22, 23], a numerical model the same as the simulation models in [42] is prepared using FEM and the related simulation data is extracted.

Briefly, the used numerical model in [42] is a 40 by 40 pixel conductivity image with 2.25mm pixel length. A conductive object is placed at the center of the image which is in the form of a circle with radius 15.75mm in the xx direction and in the form of a square in yy direction with side length of 31.5mm. To create anisotropic conductivity condition, the conductivity of the circle object is assigned to be 0.4 S/m, where the conductivity of the square object is 0.6 S/m. An isotropic conductivity of 0.2 S/m is taken for the

background material. Furthermore, the conductivity values in anisotropic directions xy and yx are taken as zero ($\sigma_{xy} = \sigma_{yx} = 0$) [42].

The reconstructed anisotropic conductivity images of the extracted simulation data using AHEPP algorithm is illustrated in Figure 4.4. To evaluate the reconstruction accuracy of the proposed algorithm, the error in the reconstructed anisotropic conductivity is calculated using (4.4). The obtained error values for AHEPP algorithm are compared with the calculated errors of the other three J -based algorithms in [42].

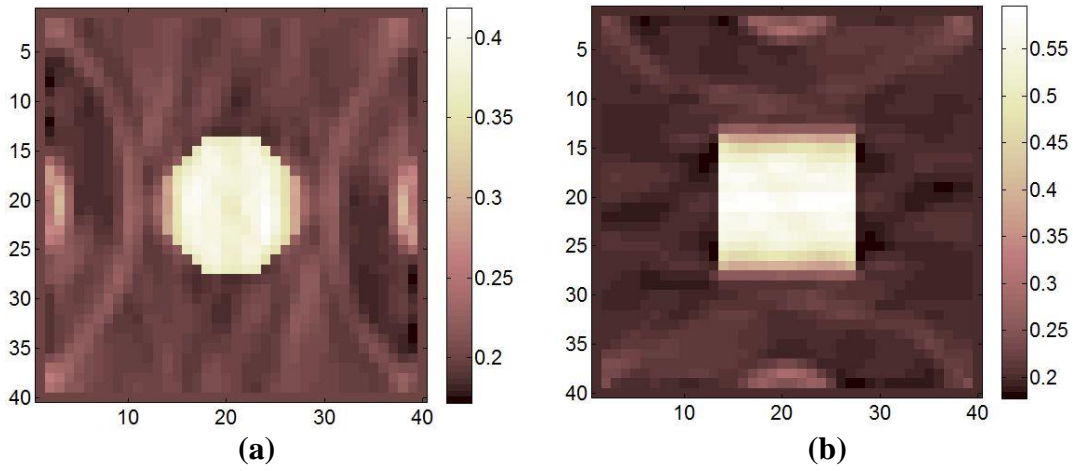


Figure 4.4: Reconstruction results of the simulation model using AHEPP algorithm (SNR = ∞). (a) σ_{xx} (b) σ_{yy} .

Table 4.3: Comparing the error values obtained from the four MRCTI algorithms using the same numerical model in [42] and for the noise free case. (The error values of the first three algorithms are taken from [42]).

Algorithm	$\epsilon_{\sigma_{xx}}$ (%) Object	ϵ_{yy} (%) Object	$\epsilon_{\sigma_{xx}}$ (%) Background	ϵ_{yy} (%) Background
AEPP	10.58	17.6	8.65	8.51
AJS	28.89	46.82	8.59	15.33
AHJS	10.15	17.43	6.35	6.72
AHEPP	9.8055	17.3948	7.7084	8.1232

As it is seen from the calculated errors in Table 4.3, the reconstruction accuracy of the AHEPP algorithm is the same and even better than the other three J -based MRCTI algorithms in reconstruction of the simulation data.

4.7 Results of the Experimental Phantom

4.7.1 Experimental Results of the Magnetic Flux Density and Current Density

Distributions

The experimental phantom is the previously introduced phantom in Section 3.4 and Figure 3.10. As it is shown in Figure 3.11, by using this phantom with four electrodes, six current injection paths are assumed. One vertical, one horizontal and four adjacent current injections are made using this phantom and the magnetic flux density distributions in three directions for all six paths along with the related current density distribution data are shown in Figures 4.5– 4.16

Furthermore, to compare the experimentally obtained magnetic flux density with the results of the numerical model, the z component of the magnetic flux density due to the current injection in the numerical model, is illustrated as an example beside the related experimental data for each current injection profile. One magnetic flux density distribution is existed for each current injecting profile. On the other hand, to calculate derivatives of B_x and B_y with respect to z using the definition of derivative in equation (2.10), two slices in z direction are selected with distance d . Therefore, two magnetic flux density distributions are obtained, as it is illustrated in Figures 4.5-4.16.

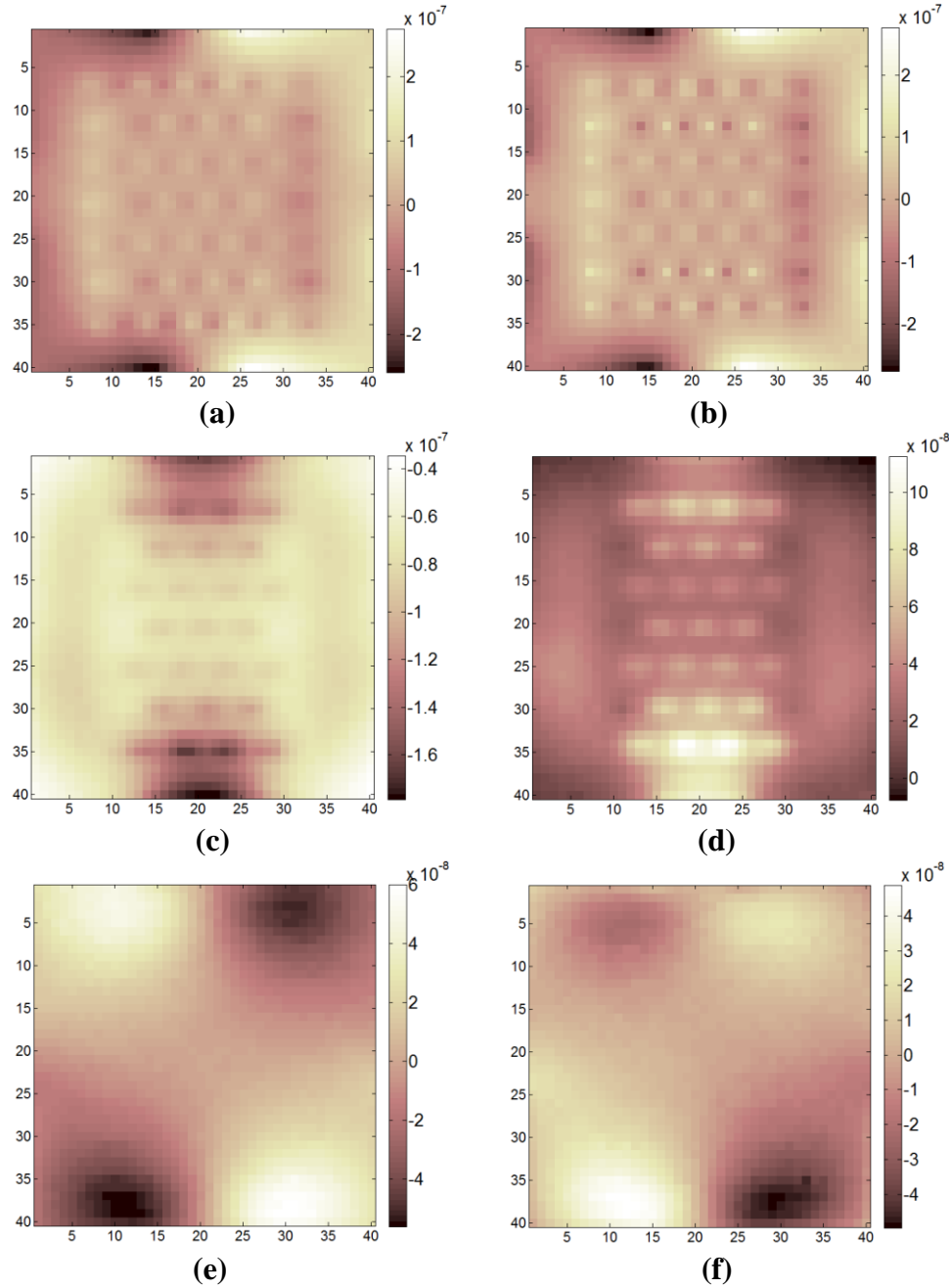


Figure 4.5: The magnetic flux density distribution in all three orientations for the vertical current injection path using the experimental phantom. (a) z component (experimental) (b) z component (numerical) (c) x -plus (d) x -minus (e) y -plus (f) y -minus.

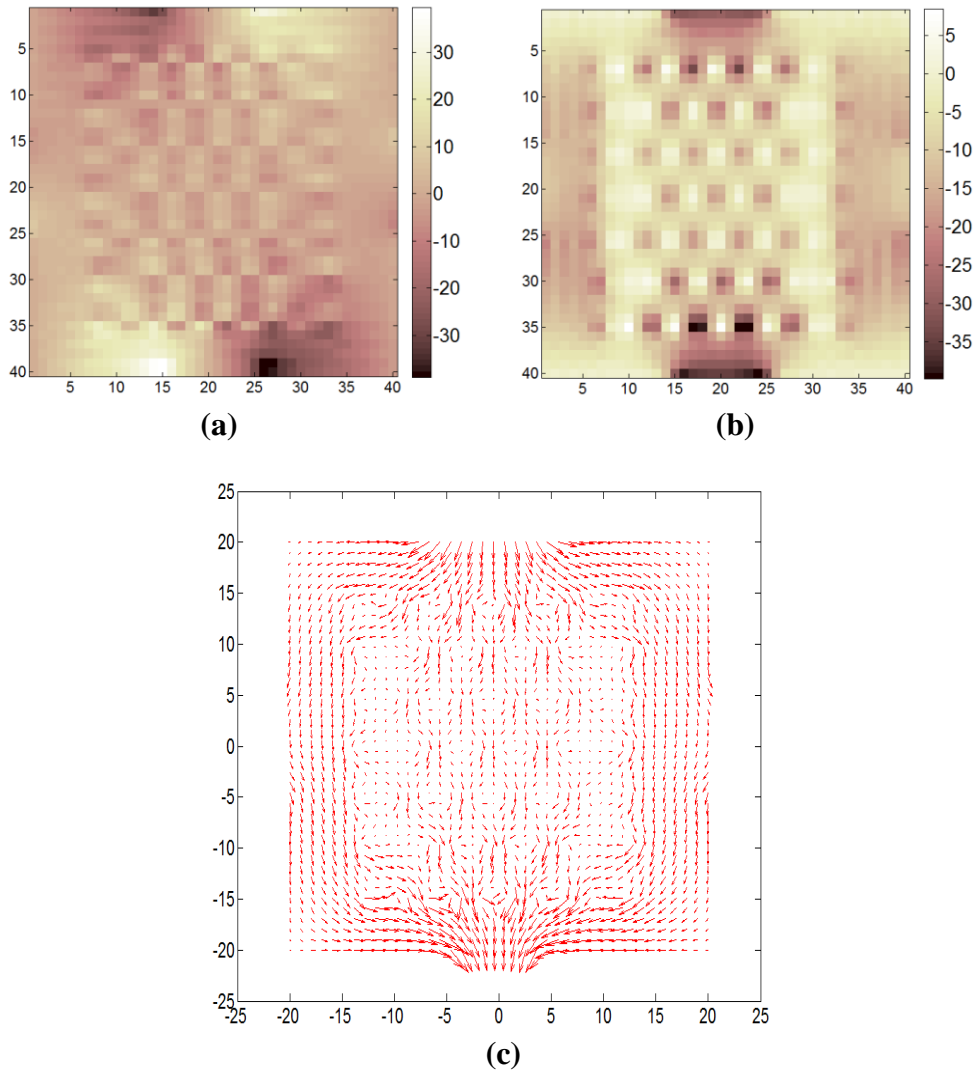


Figure 4.6: Current density distribution for the vertical current injection path of the experimental phantom. (a) J_x (b) J_y (c) Total current density distribution.

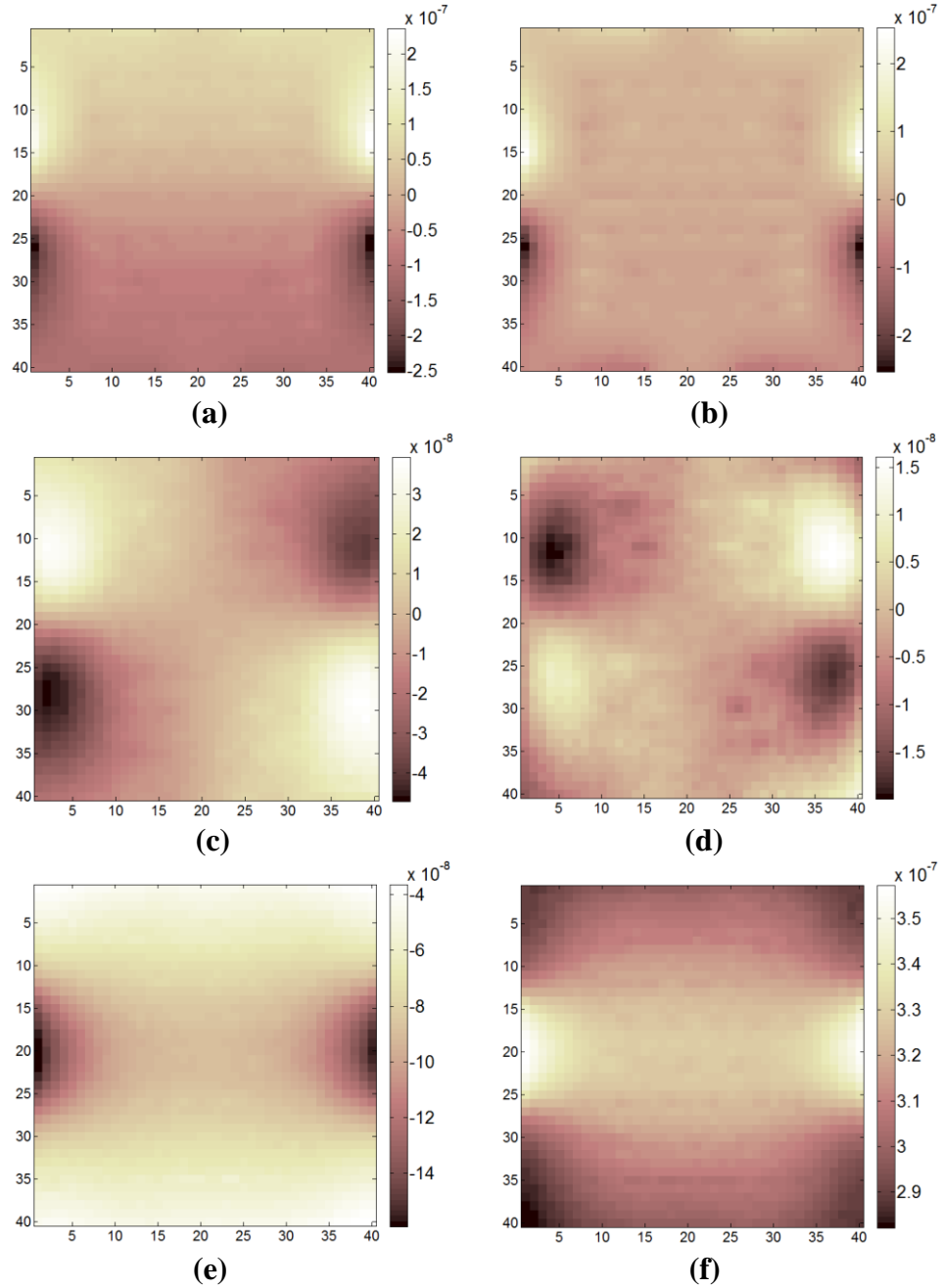


Figure 4.7: The magnetic flux density distribution in all three orientations for the horizontal current injection path using the experimental phantom. (a) z component (experimental) (b) z component (numerical) (c) x -plus (d) x -minus (e) y -plus (f) y -minus.

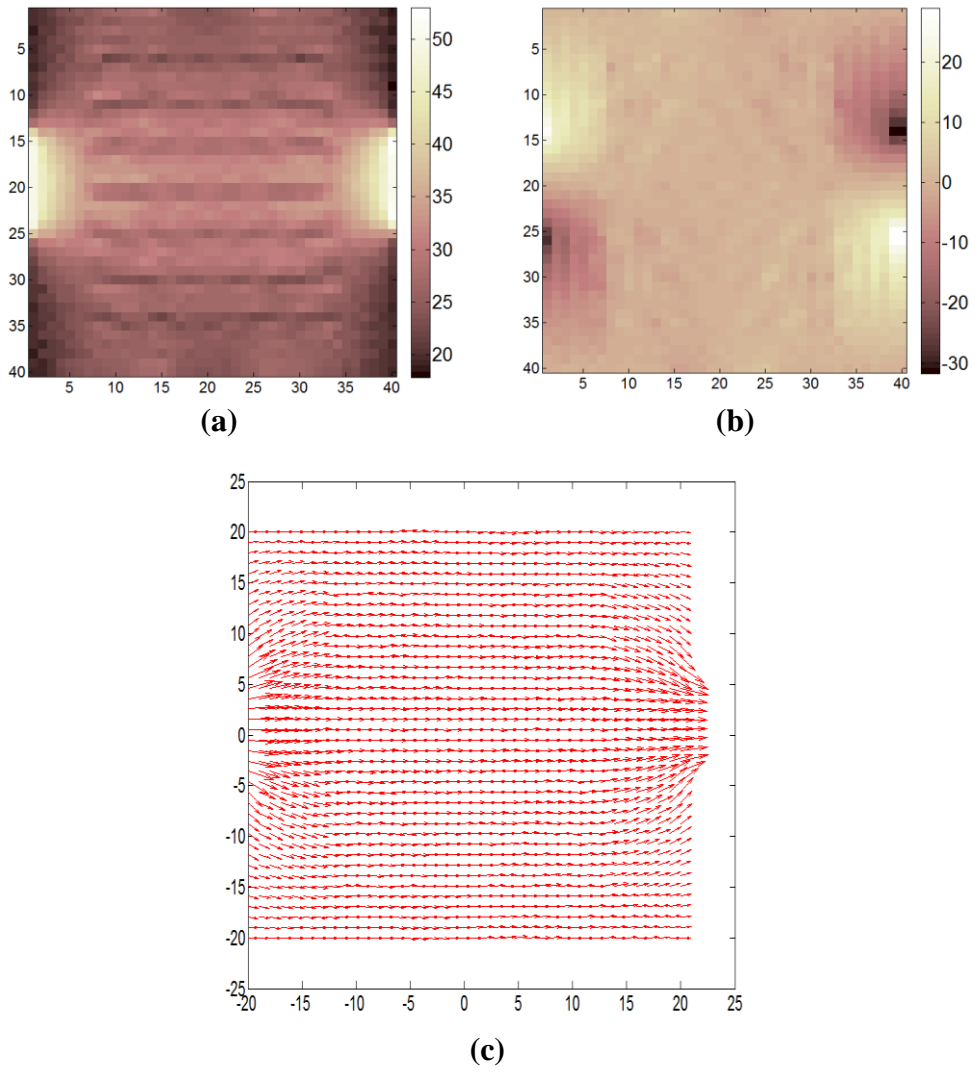


Figure 4.8: Current density distribution for the horizontal current injection path of the experimental phantom. (a) J_x (b) J_y (c) Total current density distribution

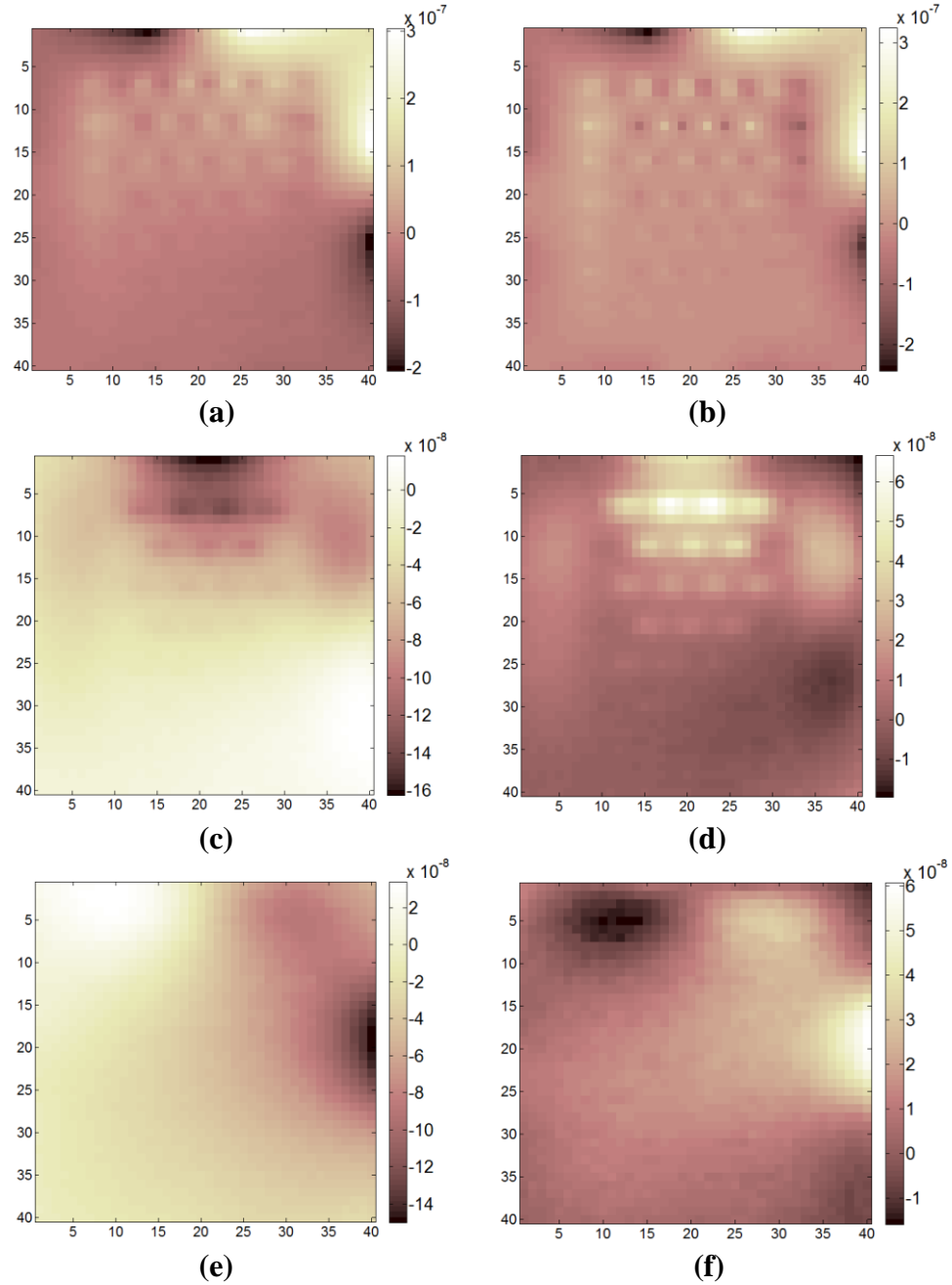


Figure 4.9: The magnetic flux density distribution in all three direction for the first adjacent current injection path (up and right electrodes) using the experimental phantom. (a) z component(experimental) (b) z component (numerical) (c) x-plus (d) x-minus (e) y-plus (f) y minus

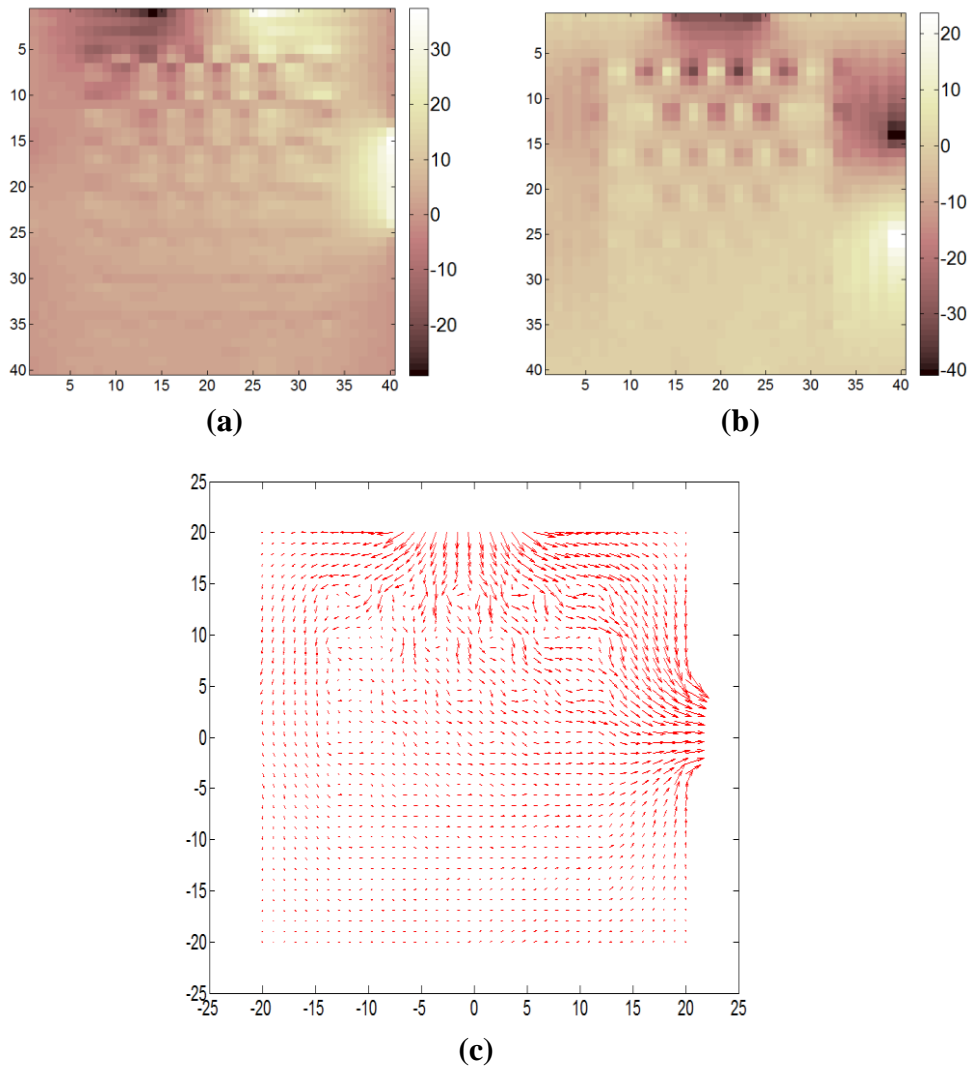


Figure 4.10: Current density distribution for first adjacent current injection path (up and right electrodes) of the experimental phantom. (a) J_x (b) J_y (c) Total current density distribution

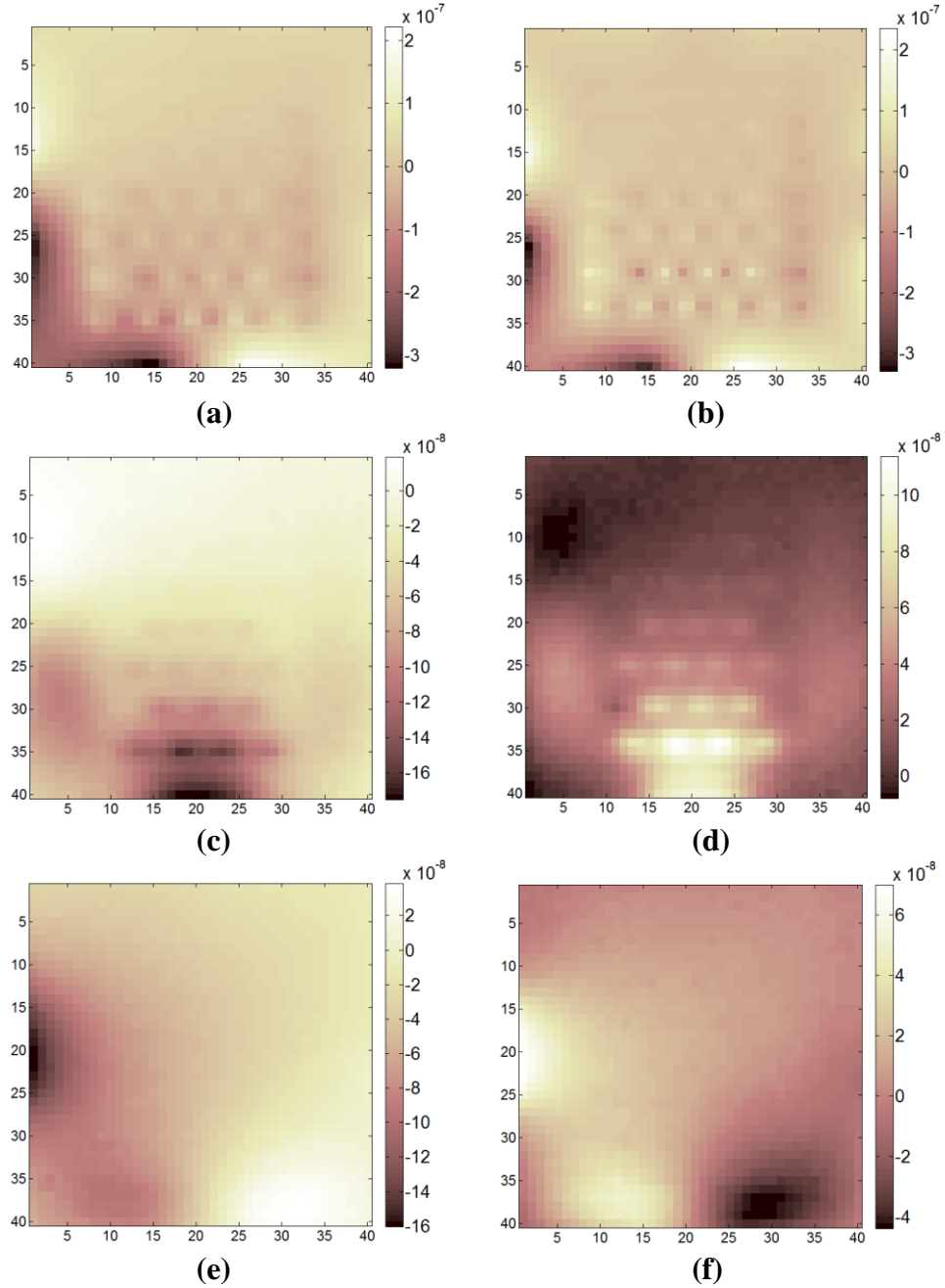


Figure 4.11: The magnetic flux density distribution in all three direction for the second adjacent current injection path (left and down electrodes) using the experimental phantom. (a) z component(experimental) (b) z component (numerical) (c) x-plus (d) x-minus (e) y-plus (f) y minus

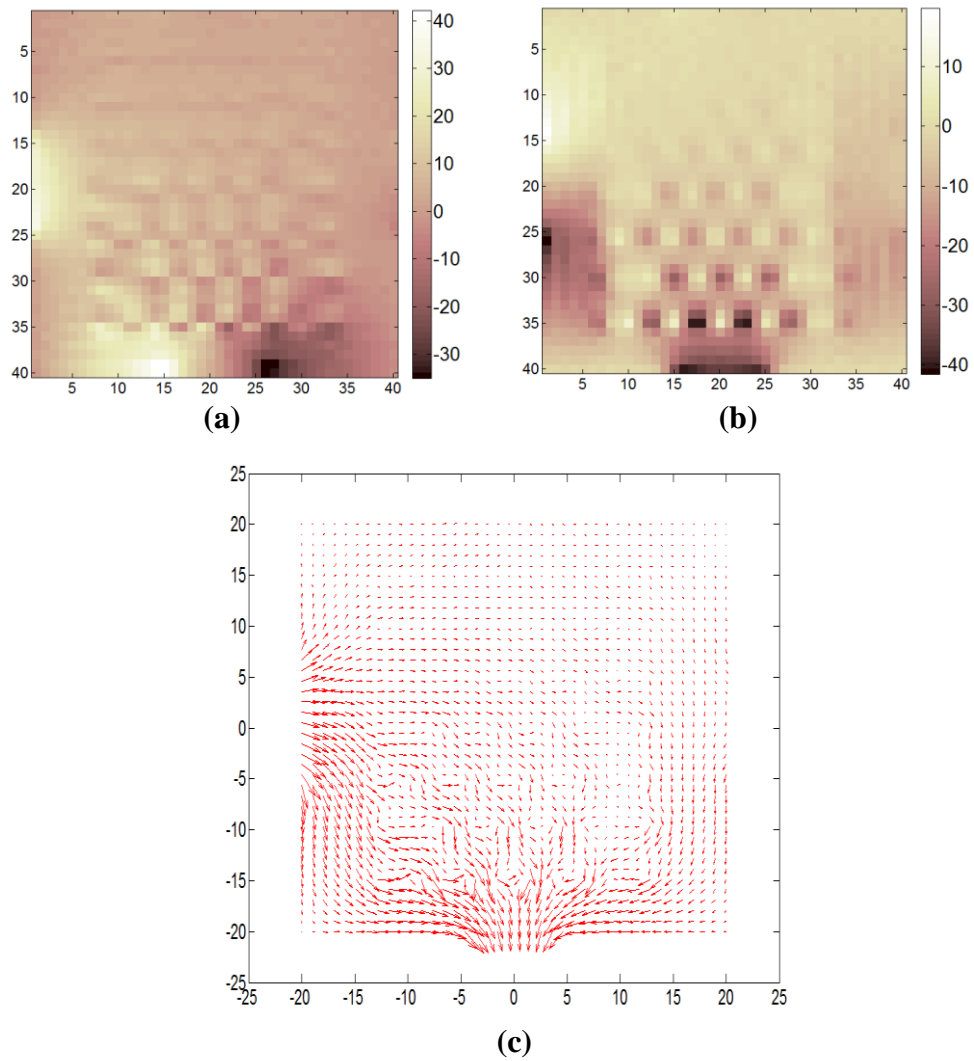


Figure 4.12: Current density distribution for the second adjacent current injection path (left and down electrodes) of the experimental phantom. (a) J_x (b) J_y (c) Total current density distribution

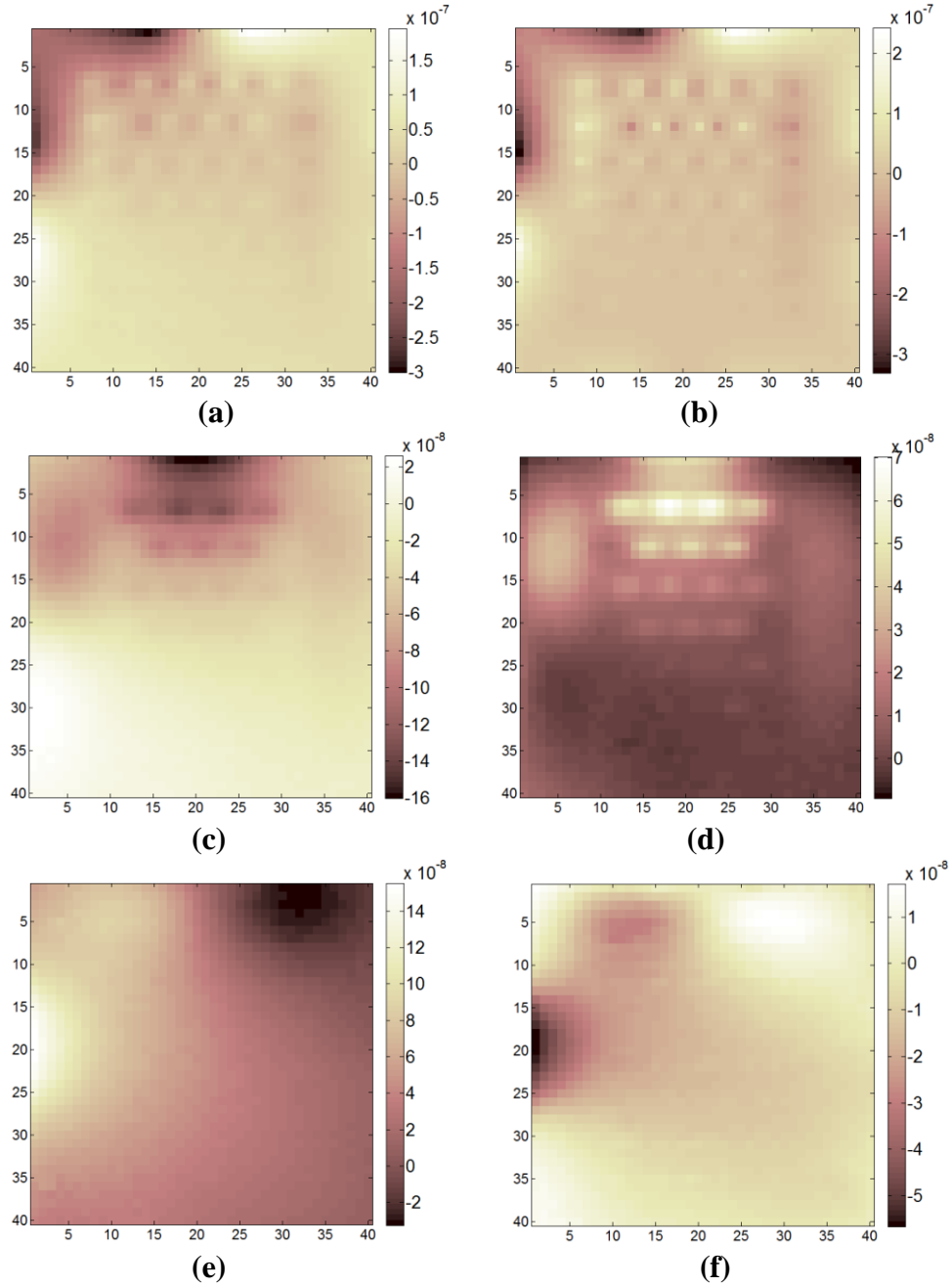


Figure 4.13: The magnetic flux density distribution in all three direction for the third adjacent current injection path (up and left electrodes) using the experimental phantom. (a) z component(experimental) (b) z component (numerical) (c) x-plus (d) x-minus (e) y-plus (f) y minus

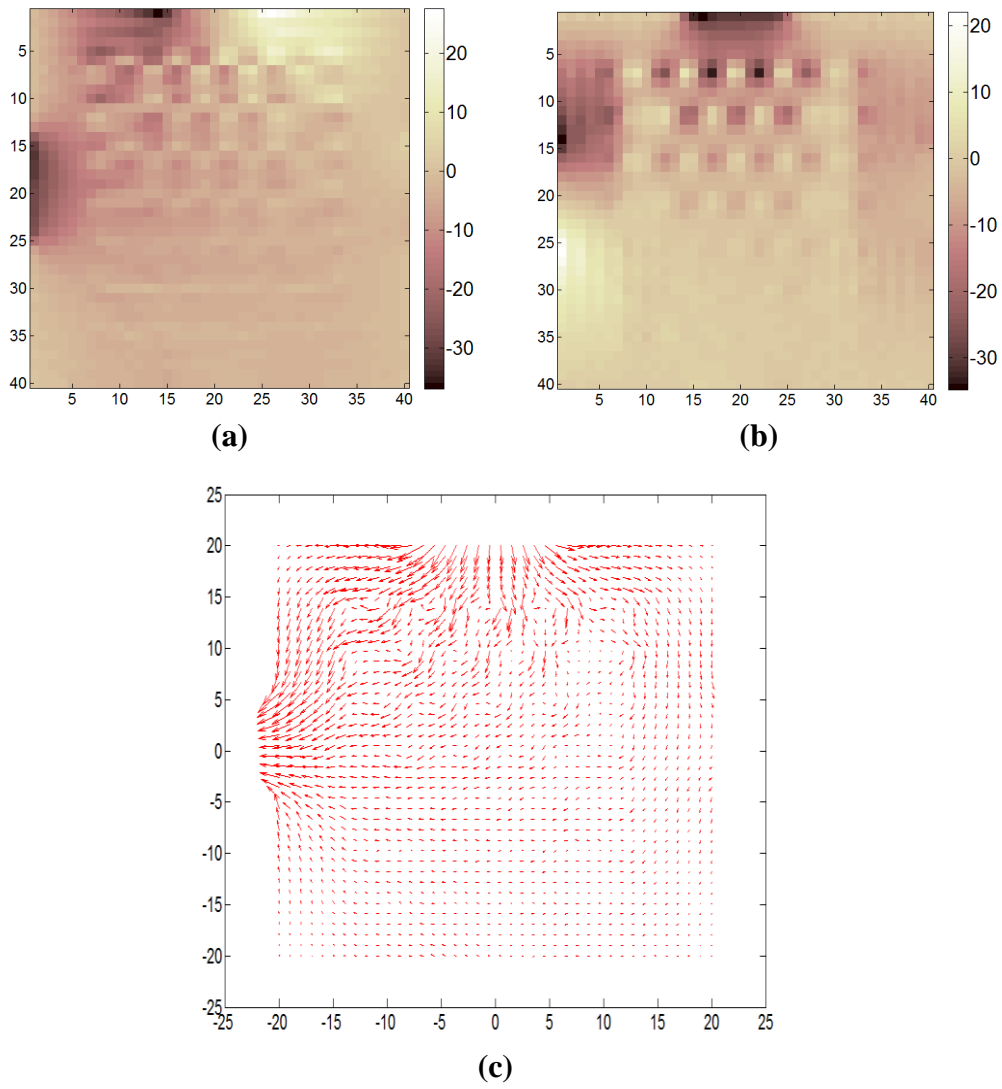


Figure 4.14: Current density distribution for the third adjacent current injection path (up and left electrodes) of the experimental phantom. (a) J_x (b) J_y (c) Total current density distribution

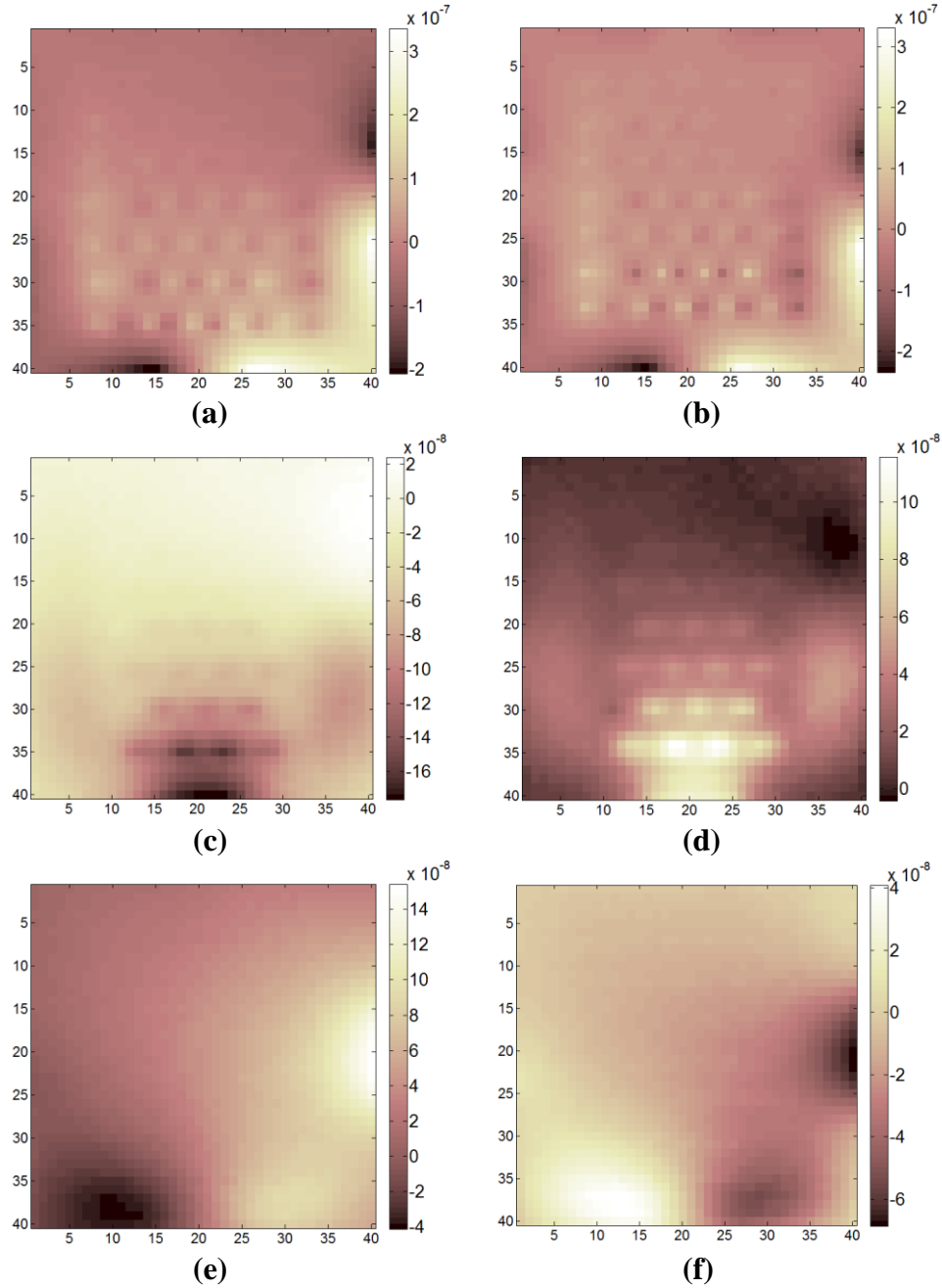


Figure 4.15: The magnetic flux density distribution in all three direction for the fourth adjacent current injection path (right and down electrodes) using the experimental phantom. (a) z component(experimental) (b) z component (numerical) (c) x -plus (d) x -minus (e) y -plus (f) y -minus

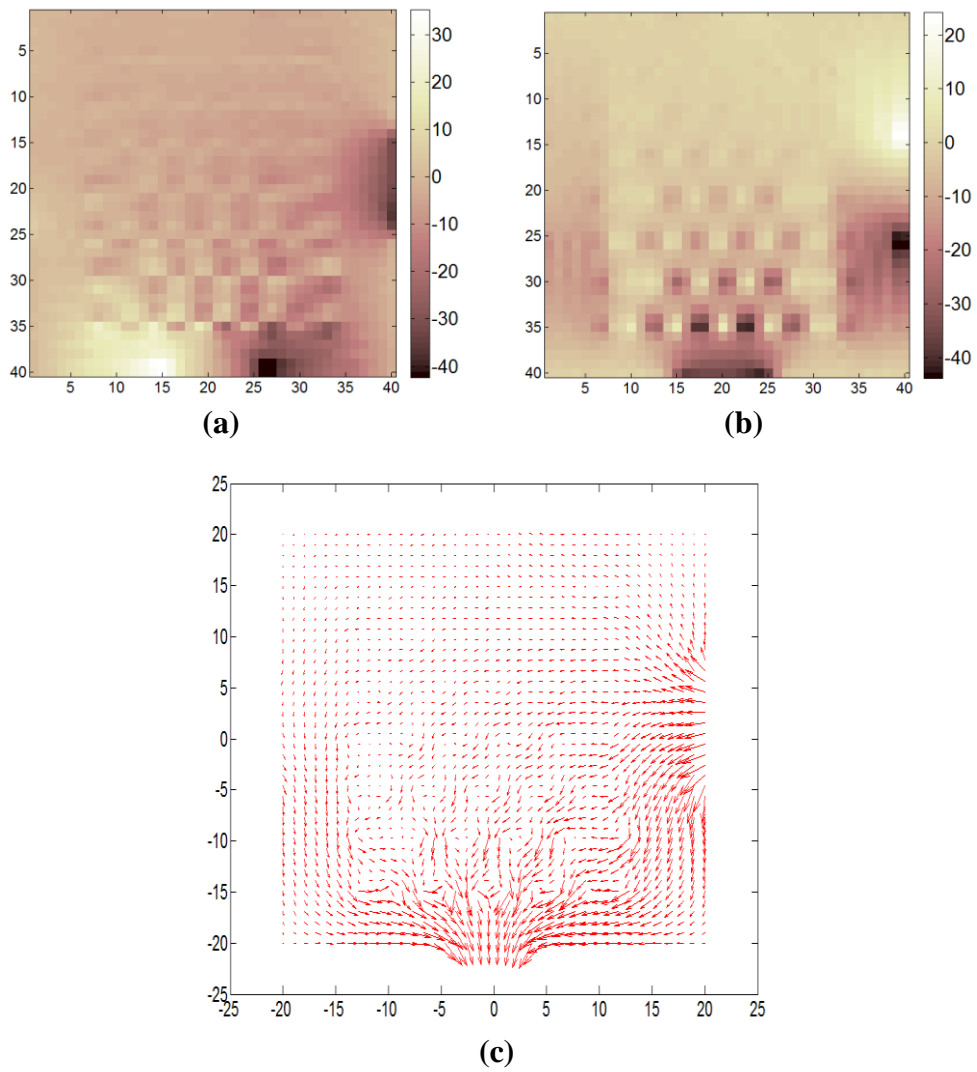


Figure 4.16: Current density distribution for the fourth adjacent current injection path (left and down electrodes) of the experimental phantom. (a) J_x (b) J_y (c) Total current density distribution

4.7.2 Experimental Results of the Reconstructed Anisotropic Conductivities

In this subsection, the experimental results of the reconstructed anisotropic conductivities in xx and yy directions (σ_{xx} , σ_{yy}) using the four J -based reconstruction algorithms along with the error calculations for each case is given. As it is mentioned in Section 4.3, to calculate the error measure a true conductivity distribution is needed. The obtained true conductivity distributions using equations in (4.5) is demonstrated in Figure 4.17.

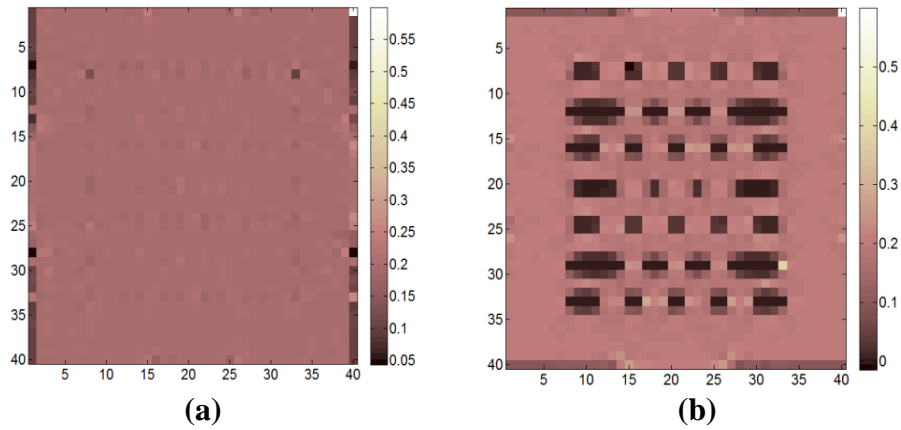


Figure 4.17: True conductivity distributions obtained using (4.5). (a) σ_{xx} (b) σ_{yy}

These true conductivity images are illustrated for each case to be compared with the reconstructed conductivity image.

4.7.2.1 The Reconstructed Conductivities Using AEPP algorithm

In this section, the two reconstructed conductivity images (σ_{xx} , σ_{yy}) using AEPP algorithm is illustrated along with the calculated true conductivity distributions in xx and yy directions in Figure 4.18.

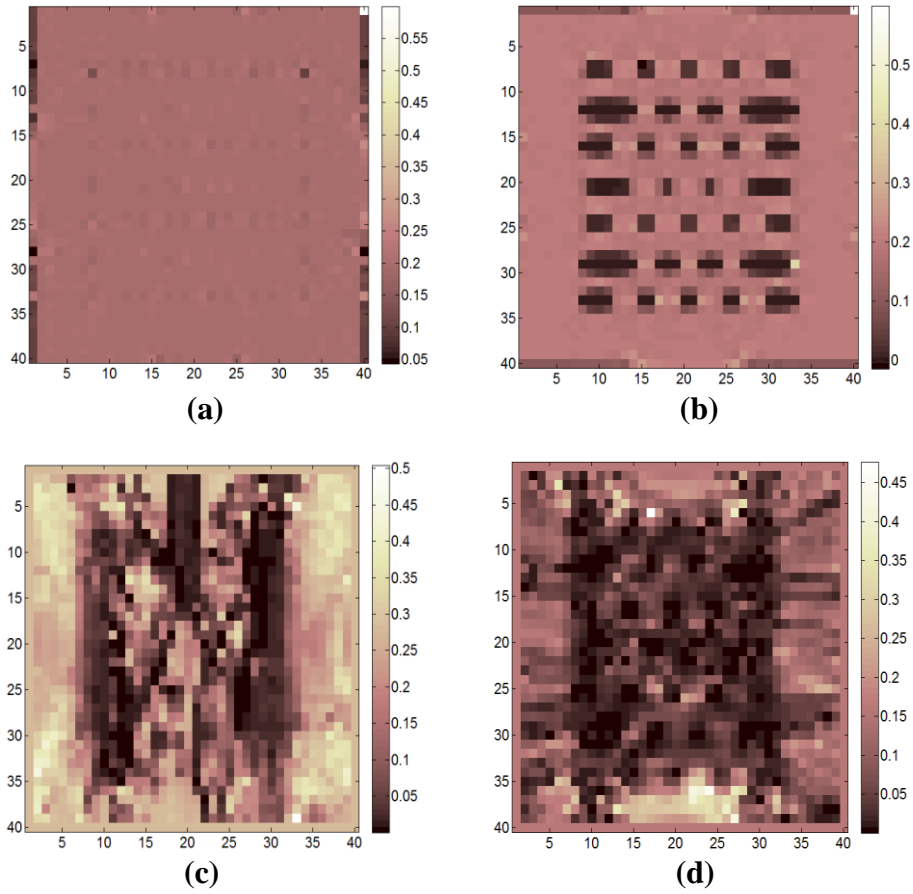


Figure 4.18: The results of anisotropic conductivity reconstructed using AEPP algorithm for the experimental phantom (a) True conductivity σ_{xx} (b) True conductivity σ_{yy} (c) Reconstructed σ_{xx} (d) Reconstructed σ_{yy}

As it is seen from the Figure 4.18, the reconstructed conductivities using AEPP algorithm are very erroneous to the extent that cannot be evaluated using error measures.

4.7.2.2 The Reconstructed Conductivities Using AJS algorithm

In this section, the two reconstructed conductivity images (σ_{xx}, σ_{yy}) using AJS algorithm is illustrated along with the calculated true conductivity distributions in xx and yy directions in Figure 4.19.

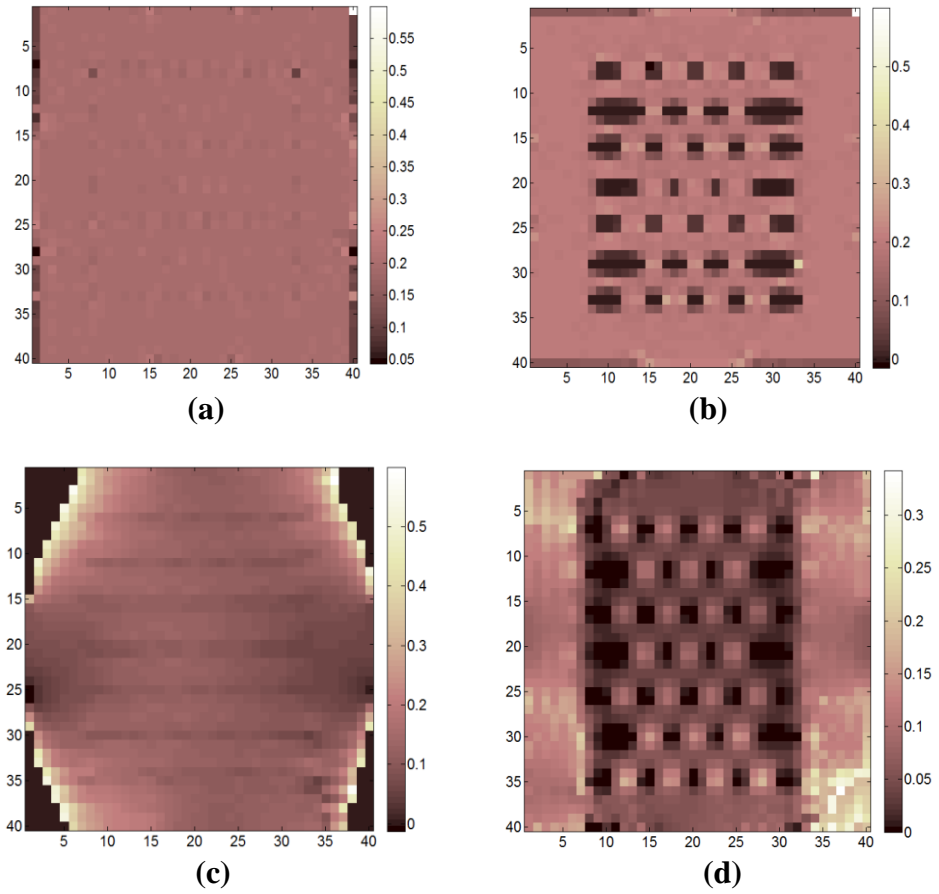


Figure 4.19: The results of anisotropic conductivity reconstructed using AJS algorithm for the experimental phantom (a) True conductivity σ_{xx} (b) True conductivity σ_{yy} (c) Reconstructed σ_{xx} (d) Reconstructed σ_{yy}

Table 4.4: Percentage error of the reconstructed conductivities in Figure 4.19

Anisotropic Conductivity	σ_{xx}	σ_{yy}
Error %	40.04	53.66

4.7.2.3 The Reconstructed Conductivities Using AHJS algorithm

In this section, the two reconstructed conductivity images (σ_{xx}, σ_{yy}) using AHJS algorithm is illustrated along with the calculated true conductivity distributions in xx and yy directions in Figure 4.20.

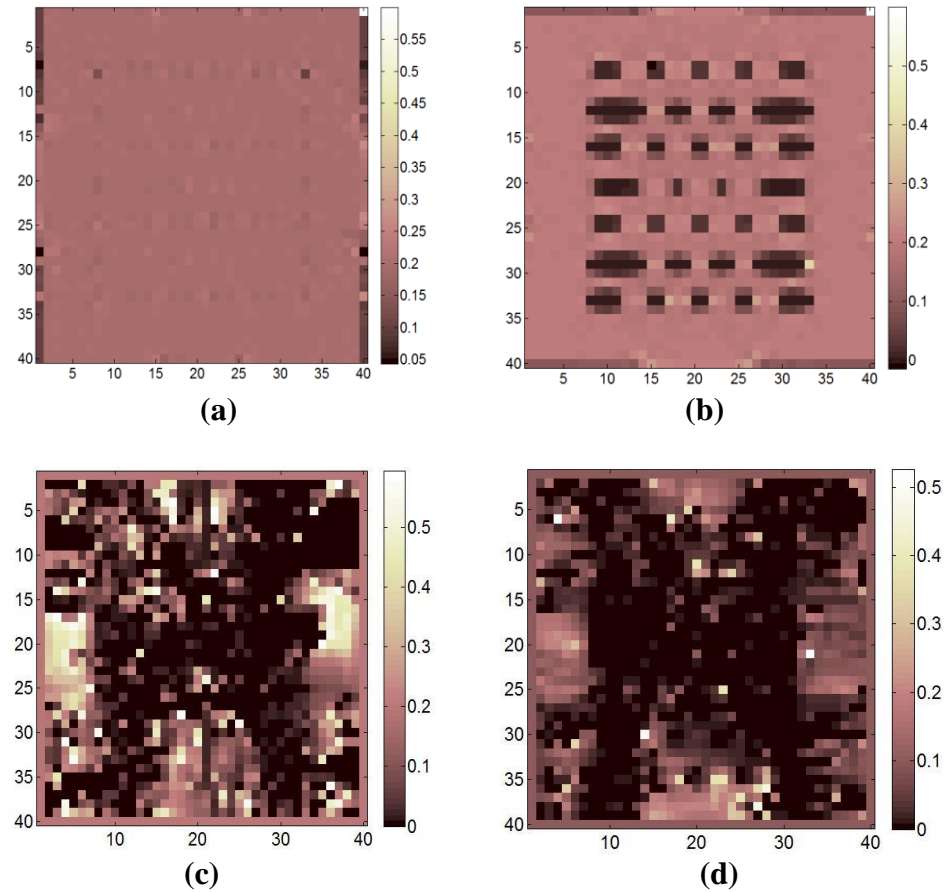


Figure 4.20: The results of anisotropic conductivity reconstructed using AHJS algorithm for the experimental phantom (a) True conductivity σ_{xx} (b) True conductivity σ_{yy} (c) Reconstructed σ_{xx} (d) Reconstructed σ_{yy}

Similar to the results of the AEPP algorithm, the obtained conductivity images for this algorithm can not be evaluated using the error measures because of the highly erroneous results.

4.7.2.4 The Reconstructed Conductivities Using AHEPP algorithm

In this section, the two reconstructed conductivity images (σ_{xx}, σ_{yy}) using AHEPP algorithm is illustrated along with the calculated true conductivity distributions in xx and yy directions in Figure 4.21.

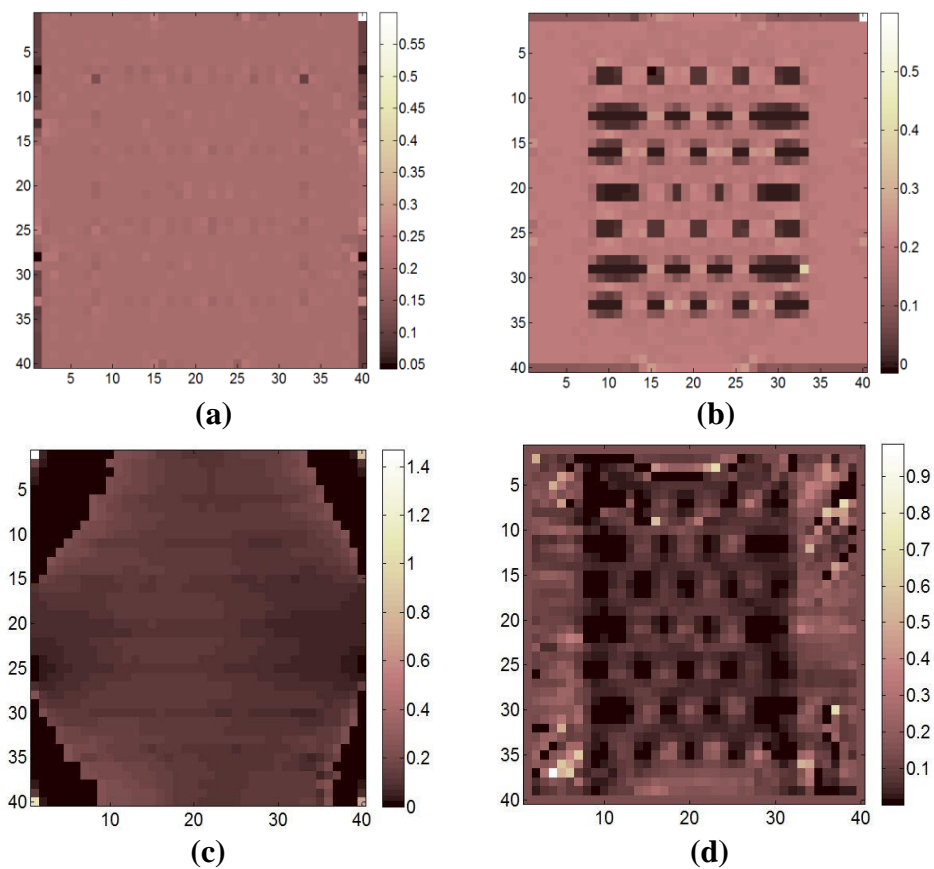


Figure 4.21: The results of anisotropic conductivity reconstructed using AHEPP algorithm for the experimental phantom (a) True conductivity σ_{xx} (b) True conductivity σ_{yy} (c) Reconstructed σ_{xx} (d) Reconstructed σ_{yy}

Table 4.5: Percentage error of the reconstructed conductivities in Figure 4.21

Anisotropic Conductivity	σ_{xx}	σ_{yy}
Error %	61.56	58.98

4.7.3 Comparisons of the Four J -Based MRCTI Algorithms

As it is explained in Chapter 2, in J -based MRCTI reconstruction algorithms the current density distribution inside the imaging region is calculated by taking derivative of the magnetic flux density data. The experimentally obtained magnetic flux density distribution is a noisy data because in the case of real experiments the SNR level is not infinite. Taking derivative from this noisy data causes a huge increase in the noise level in the obtained current density distribution. On the other hand, as it is explained in Section 2.4.1.2, in the case of AEPP algorithm the boundary potentials are projected into the imaging region using the equipotential lines. These lines are constructed in the imaging region using the current density data and observing the angle calculated in (2.19), at each iteration. Using the noisy current density data, results in projecting the boundary potentials to the wrong pixels in the imaging region. Subsequently, a wrong potential gradient is calculated and the obtained anisotropic conductivity becomes highly erroneous. When this phenomena is associated with the isotropic assumption in the first iteration of the AEPP algorithm as it is mentioned in Section 2.4.4, results in an extremely erroneous image for the conductivity distribution which is shown in Figure 4.18.

In the case of AJS algorithm, as the potential field in the imaging region is calculated using FEM therefore, the calculated potential gradient in the imaging region is independent of the noisy current density data. However, in calculation of the reconstructed

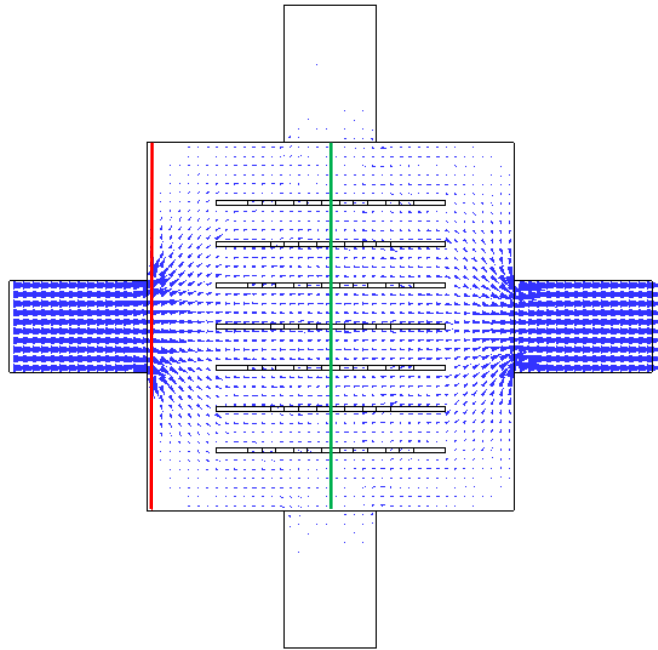
conductivity using equations in (2.28), the noisy current density data defects the resultant conductivity images. That is why, the reconstructed anisotropic conductivities in Figure 4.19 show better visual results along with reduced calculated errors. The black regions at the corners of the reconstructed images shown in Figure 4.19, are actually related to the pixels with negative conductivity values in σ_{yy} image and the very large positive values in the σ_{xx} image. As the negative conductivity value is not meaningful these pixel are assigned to possess zero conductivity. Similarly, in the case of very large positive values at the corners of σ_{xx} image, the pixels which have values ten times greater than the background conductivity are taken as zero. In the presence of these pixels and under the effect of those large values of the image scaling, the conductivity image cannot be displayed properly. Furthermore, to calculate the error values in this case the mentioned regions in σ_{xx} and σ_{yy} are not taken into account.

The reconstructed conductivities using the AHJS algorithm show similar results with the AEPP. As it is explained in 2.4.3, in this algorithm the final best result of the reconstructed conductivity using AEPP algorithm is fed to AJS as initial conductivity distribution. But, starting the AJS algorithm with an extremely noisy data causes a highly erroneous result for this algorithm as well. The anisotropic conductivity images given in Figure 4.20 are the proof of this claim.

The proposed hybrid algorithm namely, the anisotropic hybrid equipotential projection (AHEPP) algorithm is explained in Section 4.2.2. In this algorithm, unlike the AHJS algorithm, instead of using an extremely erroneous result of the AEPP algorithm as starting point for AJS, the final best result of anisotropic conductivity distribution resulted from AJS (Figure 4.19) is fed to AEPP algorithm as initial conductivity distribution. This procedure can solve the problem of the AEPP algorithm in the case of isotropic assumptions in the first iteration. On the other hand, by starting the AEPP algorithm with an acceptable conductivity distribution with reduced error a better result is obtained to the

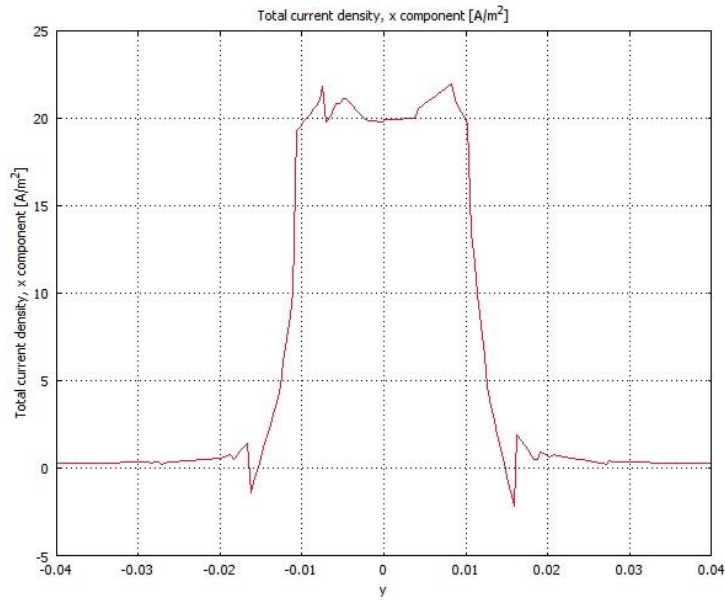
extent that to be evaluated using the error measures. Furthermore, as it is explained in Section 2.4.4, the entire time which is needed to obtain the desired conductivity distribution (Figure 4.21) using this algorithm is about one tenth of the time which is needed for the AJS algorithm to reach to the desired conductivity result for the same number of iterations (Figure 4.19).

As the final comparison of the four J -based MRCTI reconstruction algorithms the increased error at the corners of the reconstructed conductivity images is discussed. As it is expressed in Section 3.4, the current density data in the corner regions of the experimental phantom is the minimum (Figure 4.22). Therefore, current density data in these points is more sensitive to the experimental noise and these regions in the reconstructed conductivity images of the all four algorithms are more erroneous. But, it can be inferred from the Figures 4.18-4.21, that this increased error at the corners of the reconstructed conductivity images using AJS is the minimum where in the case of AEPP algorithm is maximum. Because, the AEPP algorithm is more sensitive to the current density noise as explained previously where, the AJS has the least sensitivity to current density noise in conductivity calculation, among the four algorithms. The effect of this error sensitivity is better visible in the resultant conductivity images from the AHEPP algorithm in compare with the AJS in the yy direction (σ_{yy}), because a main part of the AHEPP is based on the AEPP algorithm.

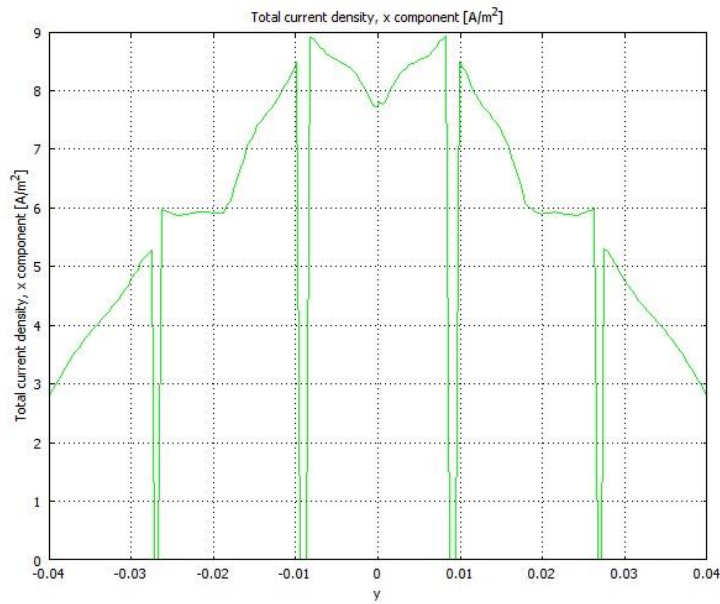


(a)

Figure 4.22: Illustration of current density minimality in corner pixels of the simulation phantom. (a) Total current density in horizontal current injection profile (b) x component of the total current density along the specified red line in (a). As it is illustrated in the (b) the current density along the selected line is minimum for the pixels in corner points. The negative picks of current density in the diagram (b) is due to rapid transitions of the current lines when leaving the recessed part of the electrode. (c) x component of the total current density in the middle line of the simulation phantom (green line).



(b)



(c)

Figure 4.22: (continued)

At the end of this chapter, performance of the four J -based MRCTI reconstruction algorithms in anisotropic conductivity reconstruction is compared from different aspects and illustrated using the performance chart Figure 4.23, for the experimental data. The information about the simulation reconstruction quality and simulation errors in the chart is taken from [42].

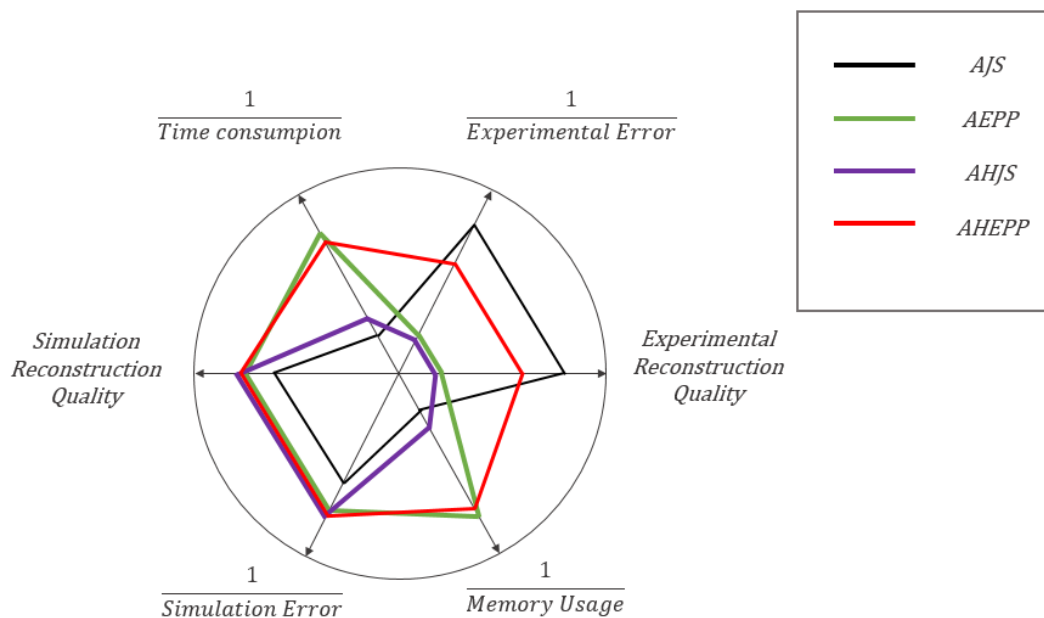


Figure 4.23: The performance chart of the four J -based algorithms

As it can be inferred from the performance chart in Figure 4.23, by considering all aspects of simulation and experimental applications, the proposed AHEPP algorithm shows a good overall performance. This algorithm inherits the good performance of the AEPP algorithm in simulation model applications along with low time consumption and low memory usage, because the main part of this algorithm is the AEPP algorithm.

Similarly, the good performance of the AJS algorithm in experimental applications can be seen in AHEPP algorithm as well.

The best performance in the simulation applications belongs to AHEPP algorithm where, in the experimental applications AJS algorithm shows the best results and AHEPP is in the second place.

CHAPTER 5

CONCLUSIONS

In this thesis, the previously proposed three J -based MRCTI reconstruction algorithms namely, the anisotropic equipotential projection (AEPP), the anisotropic J -substitution (AJS) and the anisotropic hybrid J -substitution (AHJS) algorithms along with the newly proposed J -based algorithm, anisotropic hybrid equipotential projection (AHEPP) are used to reconstruct the anisotropic conductivity distribution of the experimental phantom using the UMRAM 3 Tesla Magnetic Resonance Imaging (MRI) system. The obtained experimental results consist of magnetic flux density distribution, current density data and the reconstructed anisotropic conductivities. The reconstructed conductivities are evaluated using error measures to obtain the accuracy of the used reconstruction algorithms. Furthermore, the scaled version of the relative reconstructed conductivity images are obtained by using a scaling procedure. A numerical model is prepared using COMSOL to obtain the true conductivity distribution to use in error calculations. The SNR level of the performed experiments is calculated as 26, to be used in comparing the obtained experimental data in feature works with the experiments of this study.

An experimental phantom with special properties is designed and manufactured during this thesis and the required spin echo pulse sequence is prepared using the Siemens pulse sequence programming software (IDEA).

The obtained anisotropic conductivity from the experimental data is compared by considering the quality of the reconstructed images and the calculated error measures. The comparisons of the four algorithms showed that the anisotropic J-substitution algorithm shows best performance among the four algorithms and the reconstructed anisotropic conductivity using this algorithm has the best quality and a lower noise measure in both anisotropic directions (σ_{xx} , σ_{yy}). Both of the anisotropic equipotential projection and the anisotropic hybrid J-substitution algorithms do not produce meaningful and considerable results. Furthermore, these results are not to the extent that to be evaluated by error measures. Similar observations have been reported by Değirmenci and Eyüboğlu in [23] for the first three *J*-based algorithms but no error measures were reported. The experimental results of this thesis showed that the sensitivity of AEPP and AHJS algorithms to the noise of the current density data is to the extent that using an MRI device with high main magnetic field intensity and SNR cannot overcome this sensitivity. However, the experimental SNR level of the experiments in this thesis is not greater than the one in the [23].

To test the performance of the proposed anisotropic hybrid equipotential projection algorithm (AHEPP) using the simulation data a numerical model, which is given in [20, 21, 22 and 42], is prepared similar to the model. The obtained simulation results of AHEPP are compared with the results of the other three *J*-based algorithms in [42].

The experimental results reconstructed using AHEPP algorithm show better contrast quality than the AEPP and the AHJS algorithms and the noise measure calculated for the reconstructed conductivity in *yy* direction (σ_{yy}) of the experimental phantom is near to the noise measure of the AJS algorithm for this anisotropic direction as it is given in Table 4.4 and 4.7. The large difference between the two reconstruction algorithms (AJS and AHEPP) is in the reconstruction of the conductivity in *xx* direction.

REFERENCES

- [1] Miklavčič, D., Pavšelj, N. and Hart, F. X. 2006. Electric Properties of Tissues. Wiley Encyclopedia of Biomedical Engineering.
- [2] S. H. Oh, B. I. Lee, T. S. Park, S. Y. Lee, E. J. Woo, M. H. Cho, J. K. Seo, and O. Kwon, "Magnetic resonance electrical impedance tomography at 3 Tesla field strength.," *Magn. Reson. Med.*, vol. 51, no. 6, pp. 1292–6, Jun. 2004.
- [3] H. J. Kim, T. I. Oh, Y. T. Kim, B. Il Lee, E. J. Woo, J. K. Seo, S. Y. Lee, O. Kwon, C. Park, B. T. Kang, and H. M. Park, "In vivo electrical conductivity imaging of a canine brain using a 3 T MREIT system.," *Physiol. Meas.*, vol. 29, no. 10, pp. 1145–55, Oct. 2008.
- [4] *Numerical Analysis*, volume XII, ELSEVIER Inc. San Diego, CA, 2004, pp. 453-550.
- [5] R. P. Henderson and J. G. Webster, "An Impedance Camera for Spatially Specific Measurements of the Thorax," *IEEE Transactions on Biomedical Engineering*, vol. BME-25, no. 3, pp. 250-254, 1978.
- [6] C. Hähnlein, K. Schilcher, C. Sebu, and H. Spiesberger, "Conductivity imaging with interior potential measurements," *Inverse Probl. Sci. Eng.*, vol. 19, no. 5, pp. 729–750, Jul. 2011.
- [7] D. C. Barber and B. H. Brown, "Applied potential tomography," *Journal of Physics E: Scientific Instruments*, vol. 17, 1984.
- [8] P. C. Sabatier and C. Sebu, "On the resolving power of electrical impedance tomography," *Inverse Probl.*, vol. 23, no. 5, pp. 1895–1913, Oct. 2007.
- [9] G. C. Scott, M. G. Joy, R. L. Armstrong, and R. M. Henkelman, "Measurement of nonuniform current density by magnetic resonance.," *IEEE Trans. Med. Imaging*, vol. 10, no. 3, pp. 362–74, Jan. 1991.

- [10] Zhang, N. (1992). Electrical Impedance Tomography Based on Current Density Imaging. MSc Thesis, Department of Electrical Engineering, University of Toronto. Toronto, Canada.
- [11] E. J. Woo, S. Y. Lee, and C. W. Mun, "Impedance tomography using internal current density distribution measured by nuclear magnetic resonance," *Proc. SPIE 2299, Mathematical Methods in Medical Imaging III*, vol. 2299, pp. 377–385, Jul. 1994.
- [12] Y. Ziya Ider, Ö. Birgül, "Use of the magnetic field generated by the internal distribution of injected currents for Electrical Impedance Tomography (MR-EIT)," *TÜBITAK Elektrik*, vol.6, NO.3, 1998.
- [13] Ö. Birgül and Y. Z. Ider, "Use of Magnetic Field Generated by the Internal Distribution of Injected Currents for Electrical Impedance Tomography," *Proc. of IXth International Conference on Electrical Bio-Impedance in conjunction with European Concerted Action on Impedance Tomography*, pp. 418-419, September 1995.
- [14] Ö. Birgül and Y. Z. Ider, "Electrical Impedance Tomography Using Magnetic Field Generated by Internal Current Distribution," *Proc. of IEEE Engineering in Medicine and Biology, 18th Annual International Conference*, 1996.
- [15] Eyüboğlu B. M., Reddy R, and Leigh J. S., "Imaging electrical current density using nuclear magnetic resonance", *Elektrik Turkish J. of Elec. Eng. and Comp. Sci.*, 6, 201-214, 1998.
- [16] M. S. Özdemir, B. M. Eyüboğlu, and O. Özbek, "Equipotential projection based magnetic resonance - electrical impedance tomography and experimental realisation," *Physics in Medicine and Biology*, 49 (2004) 4765–4783.
- [17] O. Kwon, E. J. Woo, J. Yoon, and J. K. Seo, "Magnetic Resonance Electrical Impedance Tomography (MREIT): Simulation Study of J-Substitution Algorithm," *IEEE Trans. Biomedical Engineering*, vol. 49, no. 2, pp. 160–167, 2002.
- [18] H. S. Khang, B. Il Lee, S. H. Oh, E. J. Woo, S. Y. Lee, M. H. Cho, O. Kwon, J. R. Yoon, and J. K. Seo, "J-substitution algorithm in magnetic resonance electrical impedance tomography (MREIT): phantom experiments for static resistivity images.," *IEEE Trans. Med. Imaging*, vol. 21, no. 6, pp. 695–702, Jun. 2002.

- [19] R. Boyacıoğlu, B. M. Eyüboğlu, “J-substitution and filtered Equipotential projection based hybrid MREIT reconstruction algorithm”, Proc. of Med. Physics and Biomed. Eng. World Congress, 2009.
- [20] E. Değirmenci and B. M. Eyüboğlu, “Anisotropic conductivity imaging with MREIT using equipotential projection algorithm.,” *Phys. Med. Biol.*, vol. 52, no. 24, pp. 7229–42, Dec. 2007.
- [21] E. Değirmenci, B.M. Eyüboğlu, “Anisotropic Conductivity Imaging with MREIT Using J-substitution and Hybrid J-substitution Algorithms,” World Congress on Medical Physics and Biomedical Engineering, Munich – Germany, IFMBE Proceed", 25/II -DVD, (2009), p.4pages, 308-311.
- [22] E. Değirmenci and B. M. Eyüboğlu, “Image reconstruction in magnetic resonance conductivity tensor imaging (MRCTI).,” *IEEE Trans. Med. Imaging*, vol. 31, no. 3, pp. 525–32, Mar. 2012.
- [23] E. Değirmenci and B. M. Eyüboğlu, “Practical realization of magnetic resonance conductivity tensor imaging (MRCTI).,” *IEEE Trans. Med. Imaging*, vol. 32, no. 3, pp. 601–8, Mar. 2013.
- [24] K. Jeon, A. S. Minhas, Y. T. Kim, W. C. Jeong, H. J. Kim, B. T. Kang, H. M. Park, C.-O. Lee, J. K. Seo, and E. J. Woo, “MREIT conductivity imaging of the postmortem canine abdomen using CoReHA.,” *Physiol. Meas.*, vol. 30, no. 9, pp. 957–66, Sep. 2009.
- [25] H. J. Kim, Y. T. Kim, A. S. Minhas, W. C. Jeong, E. J. Woo, J. K. Seo, and O. J. Kwon, “In vivo high-resolution conductivity imaging of the human leg using MREIT: the first human experiment.,” *IEEE Trans. Med. Imaging*, vol. 28, no. 11, pp. 1681–7, Nov. 2009.
- [26] S. H. Oh, B. Il Lee, E. J. Woo, S. Y. Lee, M. H. Cho, O. Kwon, and J. K. Seo, “Conductivity and current density image reconstruction using harmonic Bz algorithm in magnetic resonance electrical impedance tomography.,” *Phys. Med. Biol.*, vol. 48, no. 19, pp. 3101–16, Oct. 2003.
- [27] J. K. Seo, J. R. Yoon, E. J. Woo, and O. Kwon, “Reconstruction of conductivity and current density images using only one component of magnetic field measurements,” *IEEE Trans. Biomed. Eng.*, vol. 50, no. 9, pp. 1121–1124, Sep. 2003.

- [28] H. J. Kim, W. C. Jeong, Y. T. Kim, a S. Minhas, T. H. Lee, C. Y. Lim, H. M. Park, J. K. Seo, and E. J. Woo, "In vivo conductivity imaging of canine male pelvis using a 3T MREIT system," *J. Phys. Conf. Ser.*, vol. 224, p. 012020, Apr. 2010.
- [29] Y. T. Kim, Z. Meng, A. S. Minhas, H. J. Kim, E. J. Woo, C. Y. Lim, and H. M. Park, "In vivo MREIT conductivity imaging of canine brain to evaluate ischemia and abscess," *2011 8th Int. Symp. Noninvasive Funct. Source Imaging Brain Hear. 2011 8th Int. Conf. Bioelectromagn.*, pp. 44–47, May 2011.
- [30] H. J. Kim, Y. T. Kim, W. C. Jeong, a. S. Minhas, C. Y. Lim, H. M. Park, and E. J. Woo, "Conductivity imaging of canine body using 3T magnetic resonance electrical impedance tomography (MREIT) system," *Sci. Iran.*, vol. 18, no. 6, pp. 1505–1510, Dec. 2011.
- [31] Y. T. Kim, A. S. Minhas, Z. Meng, H. J. Kim, and E. J. Woo, "Conductivity imaging of human lower extremity using MREIT with multi-echo pulse sequence and 3 mA imaging current," *2011 8th Int. Symp. Noninvasive Funct. Source Imaging Brain Hear. 2011 8th Int. Conf. Bioelectromagn.*, pp. 48–52, May 2011.
- [32] E. J. Woo, "High-resolution MREIT using low imaging currents.," Conf. Proc. IEEE Eng. Med. Biol. Soc., vol. 2011, pp. 7025–8, Jan. 2011.
- [33] T. I. Oh, H. J. Kim, W. C. Jeong, M. Chauhan, O. I. Kwon, and E. J. Woo, "Detection of temperature distribution via recovering electrical conductivity in MREIT.," *Phys. Med. Biol.*, vol. 58, no. 8, pp. 2697–711, Apr. 2013.
- [34] Z. J. Meng, S. Z. K. Sajib, M. Chauhan, R. J. Sadleir, H. J. Kim, O. I. Kwon, and E. J. Woo, "Numerical simulations of MREIT conductivity imaging for brain tumor detection.," *Comput. Math. Methods Med.*, vol. 2013, p. 704829, Jan. 2013.
- [35] Z. P. Liang, P. C. Lauterbur, "Signal localization" in *Principles of Magnetic Resonance Imaging: A Signal Processing Prespective*, Washington, SPIE, 2000, pp. 141–186.
- [36] H. R. Gamba and D. T. Delpy, "Artefacts in MR images of electrical current distribution," *Phys. Med. Biol.* 1997; 42:2481–2491.
- [37] G. C. Scott, M. L. G. Joy, R. L. Armstrong, R. M. Henkelman, "Sensitivity of magnetic resonance current density imaging", *J Magn. Reson.*, vol. 97, pp. 235-254, 1992.

- [38] R. Sadleir, S. Grant, S. U. Zhang, B. I. Lee, H. C. Pyo, S. H. Oh, C. Park, E. J. Woo, S. Y. Lee, O. Kwon, J. K. Seo, "Noise analysis in magnetic resonance electrical impedance tomography at 3 and 11 T field strengths", *Physiol. Meas.*, vol. 26, pp. 875-884, 2005.
- [39] L. Ying, "Phase Unwrapping," *Wiley Encyclopedia of Biomedical Engineering*.2006. DOI: 10.1002/9780471740360.ebs1356.
- [40] Z. P. Liang, "A model-based method for phase unwrapping," *IEEE Trans. Med. Imaging*, vol. 15, no. 6, Dec. 1996.
- [41] Ö. Birgül, "Development of reconstruction algorithms for magnetic resonance electrical impedance tomography and experimental realization", PhD. Thesis, METU, Ankara, Turkey 2002.
- [42] E. Değirmenci, "High resolution imaging of anisotropic conductivity with magnetic resonance electrical impedance tomography (MREIT)", PhD. Thesis, METU, Ankara, Turkey 2010.
- [43] MAGNETOM Verio,
<http://www.healthcare.siemens.com/magnetic-resonance-imaging/3t-mri-scanner/magnetom-verio>, 3.01,2014
- [44] C. Göksu, "A Programmable Current Source for MRCDI & MREIT Applications", MSc. Thesis, METU, Ankara, Turkey 2014.
- [45] Avago Technologies, "10 Megabaud Versatile Link Fiber Optic Transmitter and Receiver for 1 mm POF and 200 µm HCS[®]," HFBR-2528Z Receiver datasheet, Nov. 2011
- [46] Göksu C., Eyüboğlu B. M., Eroğlu H.H., "A Programmable Current Source for MRCDI & MREIT Applications," XIII Mediterranean Conference on Medical and Biological Engineering and Computing 2013 IFMBE Proceedings Vol. 41, 2014, pp 198-201
- [47] Eroğlu H.H. and Eyüboğlu B. M. (2012) Design and implementation of a monopolar constant current stimulator. BIYOMUT Proc., 17th National Biomedical Engineering Meeting, İstanbul, Turkey, 2012, pp 283-286
- [48] topac.com + Instrumentsonline.com,
<http://www.topac.com/conductivityprobes.html>, 1.10.2013.